

Synthesis of Ge-based one-dimensional nanomaterials for photodetector applications

Yan, Chaoyi

2011

Yan, C. (2011). Synthesis of Ge-based one-dimensional nanomaterials for photodetector applications. Doctoral thesis, Nanyang Technological University, Singapore.

<https://hdl.handle.net/10356/47555>

<https://doi.org/10.32657/10356/47555>

Synthesis of Ge-Based One-Dimensional Nanomaterials for Photodetector Applications

Yan Chaoyi

Supervisor: Lee Pooi See

School of Materials Science & Engineering

A thesis submitted to the Nanyang Technological University in fulfillment of
the requirement for the degree of Doctor of Philosophy

2011

Acknowledgement

There are numerous people who have inspired and supported me through this exciting and joyful journey of PhD study. I am deeply indebted to them for the guidance, friendship, companionship and love.

First of all, I would like to thank my supervisor, Prof. Lee Pooi See, for all her consistent support and guidance during the project execution. There is no doubt that I would not have been able to accomplish this study without her instructive guidance, insightful suggestions and encouragements. I also would like to thank Prof. Huang Yizhong, Prof. Lance Li Lian-Jong, Prof. Wong Chee Cheong and Prof. Yan Qingyu Alex for serving on my confirmation and thesis committee.

I also would like to express my appreciation to many of the previous and current group members, Ms. Afriyanti Sumboja, Ms. Chan Meiyin, Mr. Damar Yoga Kusuma, Mr. Fatwa Firdaus Abdi, Ms. Foo Wan Ling, Mr. Khoo Eugene, Mr. Lai Jiancheng Donny, Ms. Lin Mengfang, Mr. Nandan Singh, Mr. Nguyen Anh Chien, Mr. Peter Darmawan, Mr. Sim Keng Lim Raymond, Mr. Wang Jinmin, Mr. Wang Xu, Mr. Yan Jian, Mr. Yudi Setiawan, Mr. Zhang Tao, *etc.* It was really a great time working together with them. Without their help and friendship, my research would not have progressed so well and my life would not have been so enjoyable as it has been. A special thank goes to Mr. Nandan Singh, who shares the exploration journey with me.

This study was also carried out with fruitful collaborations with other groups, Prof. Song Jin in UW-Madison and Dr. Li Liang in NIMS-MANA, Japan. I have learned quite a lot from

their enthusiasm, advices and experiences. Many of my friends in Singapore are also gratefully acknowledged. Their wisdoms and friendships are greatly appreciated and shall not be forgotten.

I would like to acknowledge all staffs of Advanced Materials Research Center (AMRC), Microelectronics Lab, Advanced Ceramics Lab, XRD-Electron Microscopy Lab and Polymer Lab for their assistance and technical support in the use of various equipments, in particular John Koh, Thomas Ker and Sharon Tan from AMRC lab.

Finally, I would like to convey my deepest appreciation to my parents and my sister for their forever endless love. Last but not least, my sincerest appreciations and blesses go to my beloved wife Lu Xiaowei and my lovely angel daughter Yan Xiaowen. I will be forever grateful for the warmest home because of you.

Table of Contents

Acknowledgement	I
Table of Contents	III
List of Figures	VI
List of Tables	XII
Abstract	XIII
 CHAPTER 1 Introduction	 1
1.1 Background	1
1.2 Objectives and Motivation	3
1.2.1 Controllable Synthesis of Complex Nanomaterials	4
1.2.2 High-Performance NW Photodetectors	6
1.3 Research Approaches	8
1.4 Thesis Overview	10
 CHAPTER 2 Literature Review	 13
2.1 Syntheses and Applications of 1D Nanostructures	13
2.1.1 Growth Mechanisms	13
2.1.2 Groups of Materials Investigated	19
2.1.3 Properties and Applications	20
2.2 Ge-Based 1D Nanostructures	27
2.2.1 Elemental Ge Nanostructures	27
2.2.2 Binary Ge-Based Nanostructures	35
2.2.3 Ternary Ge-Based Nanostructures	37
2.3 1D Nanostructures for Photodetector Applications	39
2.3.1 Small Bandgap Semiconductor NWs	39
2.3.2 Wide Bandgap Semiconductor NWs	40
2.3.3 Ternary Oxide Photodetectors with Even Larger Bandgap	42
 CHAPTER 3 Experimental Methods	 47
3.1 NW Growth Processes	47
3.1.1 Furnace Setup	47
3.1.2 Growth Substrate Preparation	48
3.1.3 Source Material Preparation	49
3.1.4 NW Growth Conditions	49
3.2 Characterizations	51
3.2.1 XRD	51
3.2.2 SEM	52
3.2.3 TEM	53
3.2.4 EDS	53
3.3 Device Fabrications and Property Measurements	54
3.3.1 Device Fabrications	54
3.3.2 Property Measurements	55
 CHAPTER 4 Elemental GeNWs: Catalytic Growth and Applications in Visible Light Photodetectors	 57
4.1 Objective	57
4.2 Au Catalyzed Growth of GeNWs	59

4.2.1 Au-Ge Binary Phase Diagram	59
4.2.2 Experimental Methods	59
4.2.3 Morphological and Structural Characterizations	60
4.2.4 Effect of Growth Temperature and Pressure on the NW Morphology	67
4.3 Bi-Catalyzed Growth of GeNWs	69
4.3.1 Bi-Ge Binary Phase Diagram.....	69
4.3.2 Experimental Methods	70
4.3.3 Morphological and Structural Characterizations	71
4.3.4 Growth Mechanisms	75
4.3.5 Effect of Bi/Ge Molar Ratio on the NW Morphology	76
4.4 Single GeNW and Networks for Visible-Light Photodetectors.....	77
4.4.1 Introduction.....	77
4.4.2 Device Fabrication Methods	78
4.4.3 Comparative Studies of Single NW and Network Devices	79
4.4.4 Conduction and Detection Mechanisms	82
4.5 Conclusions.....	87
CHAPTER 5 Synthesis of Zn ₂ GeO ₄ (ZGO) NWs for Selective Deep-UV Photodetection ..	90
5.1 Objective	90
5.2 Chemical Vapor Deposition of ZGO NWs.....	91
5.2.1 Experimental Methods	91
5.2.2 Structural Characterizations.....	92
5.2.3 Growth Mechanisms	98
5.3 Pressure-Induced Kink Formation in ZGO NWs.....	101
5.3.1 Experimental Methods	101
5.3.2 Single-Crystalline Kinked ZGO Superstructures.....	102
5.3.3 Expansion to Other Groups of Materials	104
5.3.4 Kinking Mechanisms	106
5.4 Branched ZGO-ZnO Heterostructures	107
5.4.1 Secondary Deposition Methods	107
5.4.2 Epitaxial Growth of Aligned ZnO Nanorod Arrays	108
5.4.3 Detailed Mechanistic and Crystallographic Analyses	113
5.5 ZGO NW Networks for Selective Deep-UV Photodetection	118
5.5.1 Device Fabrication Methods	118
5.5.2 Network Devices with Fast Response Time and High Wavelength Selectivity ...	118
5.6 Conclusions.....	124
CHAPTER 6 Morphology Controlled Synthesis of In ₂ Ge ₂ O ₇ (IGO) Nanostructures for Solar-Blind Photodetection.....	128
6.1 Objective	128
6.2 Self-Catalytic Growth of IGO Semi-Nanotubes	130
6.2.1 Experimental Methods	130
6.2.2 Structural Characterizations.....	130
6.2.3 Anisotropic Adsorption Induced Semi-Nanotube Formation	134
6.3 Au-Catalyzed Growth of IGO NWs	137
6.3.1 Experimental Methods	137
6.3.2 VLS Growth of IGO NWs	137
6.4 Spontaneous Growth of Ultralong IGO Nanoribbons	139
6.4.1 Experimental Methods	139

6.4.2 VS Growth of Nanoribbons with Rectangular Cross-Sections	139
6.5 Hierarchical IGO Nanostructures	144
6.5.1 Experimental Methods	144
6.5.2 Combinational Homoepitaxial Growth.....	145
6.6 High Performance UV Photodetectors Using IGO Nanoribbons	147
6.6.1 Device Fabrication Methods	147
6.6.2 Performance Characterizations	148
6.7 Conclusions.....	152
CHAPTER 7 Conclusions and Recommendations	154
7.1 Conclusions.....	154
7.2 Recommendations for Future Work.....	157
Publication List	161

List of Figures

CHAPTER 1

Figure 1. 1 A schematic summary of the quasi-1D nanostructures. (a) NWs; (b) core-shell NWs; (c) nanotubes; (d) axial heterostructures; (E) nanobelts; (F) nanotapes; (G) dendrites; (H) hierarchical nanostructures; (I) nanosphere assembly; (J) nanosprings.¹²

CHAPTER 2

Figure 2. 1 (a-c) Typical TEM images of ZnO nanobelts. (d) Cross-sectional TEM images of a ZnO nanobelts. (e) ZnO nanobelt with stacking fault. ⁴	14
Figure 2. 2 Schematic diagrams of the OAG and VLS growth processes. ⁵	15
Figure 2. 3 Schematic illustration of the VLS growth processes of GeNWs.	16
Figure 2. 4 Binary phase diagram for Au-Si. ¹¹	16
Figure 2. 5 Schematic diagram of the Ge NW growth via VLS and VSS mechanisms. When the temperature decreases, the catalyst may become solid but the growth still proceeds. ¹⁴	17
Figure 2. 6 SEM images of the wafer-scale ZnO NW grown in solution. ¹⁸	18
Figure 2. 7 Different configurations of the NWs heterostructures: (a) homogeneous NW structure; (b) axial heterostructure; (c) radial heterostructure; (d) branched heterostructure. ⁹	20
Figure 2. 8 (a) Schematic of a NW FET. (b) Id-Vd and (c) Id-Vg characteristics of the NW FET. (d) I-V behavior of n-GaN NW (green), a p-Si NW (blue), and the corresponding n-GaN/p-Si NW junction (red). ³⁵	21
Figure 2. 9 (a) Schematic diagram depicting the detection of single virus using Si NW sensor. (b) Real time observation and the conductance change of the detection process. ³⁶	22
Figure 2. 10 (a) Emission spectra from ZnO NW arrays below (curve a) and above (curve b and inset) the lasing threshold. (b) Emission intensity as a function of optical pumping energy intensity. (c) Schematic illustration of a NW resonance cavity. ⁴⁰	24
Figure 2. 11 Future integrated nanophotonic circuits for chemical analysis. ⁴¹	24
Figure 2. 12 Schematic of morphological changes that occur in Si during electrochemical cycling. ⁴²	25
Figure 2. 13 (a) Schematic diagram and (b) SEM images of the coaxial Si NW solar cells. ³¹	27
Figure 2. 14 (a) Cross-sectional and (b) top views of the Ge NWs epitaxially grown on Ge(111) substrates. ⁷²	29
Figure 2. 15 Binary phase diagram of Au-Ge. The eutectic temperature of Au-Ge is 361 °C at 28 at.% of Ge. ¹³	30
Figure 2. 16 Orientated growth of GeNWs on Ge micro-crystals. ⁸⁵	31
Figure 2. 17 (a,b) Low magnification TEM images of Ge-ZnO biaxial heterostructures; (c,d) HRTEM images of ZnO and Ge, respectively. ⁸⁸	32
Figure 2. 18 Growth sequences of the Ge p-n junctions. Red color stands for n-type segment. Green light stands for undoped segment. Blue color stands for p-type segment. ⁶⁶	32
Figure 2. 19 Synthesis of core-shell NWs by sequential deposition methods. ²⁶	34
Figure 2. 20 SEM images of the 3D GeO ₂ NW networks. ⁹⁶	35
Figure 2. 21 SEM and TEM images of the Co ₅ Ge ₇ NWs grown on flexible substrates. ⁹⁹	36
Figure 2. 22 Binary phase diagram of Co-Ge. ¹⁰⁰	37
Figure 2. 23(a) Schematic diagram and (b) AFM image of single GeNW photodetector. (c) Transfer characteristic of GeNW FET. (d) Photo-switching behavior of GeNW device under pulsed incident light (5 ms). ¹⁰⁷	40

Figure 2. 24 (a) Schematic of a ZnO NW photodetector. (b) Photo-switching behavior showing slow response and reset time. ¹⁰⁸	41
Figure 2. 25 Response and recovery characteristics of individual ZnSnO ₃ NW as exposed to UV illumination at -3 V and 300 K. ¹⁰⁹	42

CHAPTER 3

Figure 3. 1 Furnace setup used for NW growth. ¹	47
Figure 3. 2 Temperature profile of the furnace with a central temperature of 1000 °C. Location of the small quartz tube at the downstream end is indicated. Locations of the growth substrates vary in different growth round to the test the growth temperature effect.	48
Figure 3. 3 Pressure as function of Ar gas flow rate at room temperature.	50
Figure 3. 4 Digital photograph of the Rigaku XRD system.	52
Figure 3. 5 Digital photograph of the SEM system (JEOL 6340F).	52
Figure 3. 6 Digital photograph of the TEM system (JEOL 2100F).	53
Figure 3. 7 Schematic diagrams of the photolithography processes. ²	54
Figure 3. 8 Digital photograph of the FIB system (FEI Novaetch Nanolab DualBeam 600i).	55
Figure 3. 9 SEM image of a typical NW device with FIB-deposited Pt contacts.	55
Figure 3. 10 Photograph of the Keithley system: (a) overview and (b) probe tips.	56

CHAPTER 4

Figure 4. 1 Au-Ge binary phase diagram. ²⁰	59
Figure 4. 2 Experimental setup used for GeNW growth using Au catalyst.	60
Figure 4. 3 SEM images of GeNWs synthesized using Au as catalysts: (a) low magnification; (b) high magnification; (c) NWs grow out of the edge of the substrate; (d) cross-sectional view of the short Ge nanorods.	60
Figure 4. 4 Diameter distribution of the samples coated with different Au thickness. Solid lines are corresponding Gaussian fit.	61
Figure 4. 5 XRD patterns show the crystal phase of the as-synthesized GeNWs: (a) both GeO ₂ and Ge phases detected. (b) Pure Ge phase synthesized with a better vacuum condition.	62
Figure 4. 6 (a) Low magnification TEM image of the GeNWs with uniform diameter through the length; (b) high magnification TEM image of a single GeNW, showing the Au catalyst particle at the front (dark spot).	63
Figure 4. 7 (a) HRTEM and (b) FFT pattern of a GeNW. The HRTEM image is taken along [101] zone axis. Growth direction of the NWs is along [111] direction.	63
Figure 4. 8 HRTEM images and corresponding FFT patterns of GeNWs with different diameters. All the NWs characterized show the same growth direction along [111].	64
Figure 4. 9 EDS spectra of the (a) NW stems and (b) catalyst particles.	65
Figure 4. 10 EDS line scanning profile across a catalyst particle at the front of NW. Ge (green line) and Au (red line) distribution are shown in the profile.	65
Figure 4. 11(a,b) Optical images of as-synthesized GeNWs on Si substrate with different densities; (c,d) optical images of GeNWs dispersed on Si substrates with different magnifications.	67
Figure 4. 12 Temperature-dependent morphologies between the temperature region of 300-500 °C.	67
Figure 4. 13 Effect of vapor pressure inside the quartz tube on the synthesis of GeNWs: (a,b) nanoparticles or nanorods of very low yield were produced at a vapor pressure of 1×10^{-3} mbar with no introduction of Ar flow; (c,d) large scale NWs were synthesized when the vapor pressure was increased to 4.2 mbar with a Ar flow of 300 sccm.	69

Figure 4. 14 Binary phase diagram of Bi-Ge.....	70
Figure 4. 15 (a) SEM image of Bi-catalyzed GeNWs grown on Si substrate. The large particles are Bi particles deposited on the substrate. (b-d) SEM images of different magnifications of GeNWs grown on Cu grid. GeNWs can be observed at the edges of the holey carbon film (d).	71
Figure 4. 16 (a-c) Low magnification and (d-f) high magnification TEM images of the GeNWs grown on Cu grids. Metal catalyst particles (dark spots) can be clearly observed at the growth fronts as shown in (d-f).	72
Figure 4. 17 HRTEM images of the GeNWs. All the NWs characterized show the growth direction along [111].	73
Figure 4. 18 EDS spectra taken from different regions of the sample: (a) areas including large metal particles; (b) areas that only include NWs.....	73
Figure 4. 19 EDS line scanning profile across a GeNW and its Bi catalyst particle.	74
Figure 4. 20 (a,b) Schematic illustration of the GeNW growth process using Bi catalyst. (c) SEM image of the Cu grid (substrate) after a short deposition time of 5 min. Bi nanoparticles (highlighted by circles) can be observed on the substrate.....	75
Figure 4. 21 SEM images of the products synthesized using source materials of different Bi/Ge molar ratios: (a,b) 1:5; (c,d) 1:20.	76
Figure 4. 22 Typical wavelength spectra from the tungsten-halogen lamp at different emission temperatures. ³⁶ The light source used in present study was the tungsten-halogen lamp in the optical microscope of the probe station. The light intensity of the lamp can be tuned within the range of 0.02–0.8 mW cm ⁻⁴	78
Figure 4. 23 Comparison of the photoresponse behaviors of single-NW device and network device. Schematic models, <i>I</i> - <i>V</i> curves and photoresponse characteristics of (a-c) single-NW device and (d-f) NW-network device.....	79
Figure 4. 24 (a) Enlarged view of a current decay process showing the fast reset time of 0.2 s. (b) Multiple step photoresponse characteristics of network devices.	80
Figure 4. 25 Photoresponse characteristics of two typical NW-network devices, showing the fast photoresponse time observed.	81
Figure 4. 26 Schematic band diagrams for single-NW device with Ohmic contact and network device with non-Ohmic contact, at zero bias. Rectangles represent the partial contributions that are not light-sensitive (see text for more details).	82
Figure 4. 27 Schematic models for the Au-GeNW contact (a) before and (b) after FIB modification.....	84
Figure 4. 28 Schematic diagrams of single-NW, parallel-NW and entangled-NW devices....	86

CHAPTER 5

Figure 5. 1 (a) Low magnification top-view and (b) cross-sectional view SEM images of the dense ZGO NWs. (c) Enlarged SEM image showing the Au catalyst particles at the NW growth fronts. (d) XRD pattern showing a pure rhombohedral ZGO phase.	93
Figure 5. 2 (a) Low magnification TEM image showing the general morphology of ZGO NWs. (b) Enlarge view of two overlapping NWs, showing the Au catalyst particle. (c) EDS spectrum recorded from individual NW. (d) HRTEM image and (e) FFT pattern of the ZGO NW. The HRTEM image was taken along [1-10] zone axis, showing a NW growth direction along [110]. (f) Space filled structure model for a ZGO NW growing along [110] direction.	94
Figure 5. 3 (a) Low magnification TEM image of a branched NW structure. (b,c) HRTEM images of the backbone NW and backbone-branch junction. The corresponding	

positions are indicated by squares in (a). Inset in (c) is the FFT pattern along [1-1-2] zone axis.	95
Figure 5. 4 Morphologies of ZGO NWs grown under different conditions. (a,b) Dense and uniform NWs grown between 400-500 °C. (c) Short nanorods with sponge-like impurities were deposited between 500-600 °C. (d) Very few NWs were grown between 300-400 °C. (e,f) Au catalyst was shown to be essential for the growth of high quality NWs.....	97
Figure 5. 5 Schematic diagram of the VLS growth process for ternary ZGO NWs. The coevaporation and adsorption of Zn and Ge vapor to the Au catalyst resulted in the growth of ternary ZGO phase.	98
Figure 5. 6 Growth model for the branched ZGO NWs.	100
Figure 5. 7 (a-d) Low magnification TEM images of the kinked ZGO NWs. Unlike the straight NWs grown under stable growth conditions, the vapor perturbation introduces kinks in the ZGO NWs. (e-f) HRTEM images of the joint sections showing the single-crystalline structures of the kinked NWs. No structural defects were observed in the kinked NWs. Insets are the corresponding low magnification TEM images indicating the positions of the joint sections.	103
Figure 5. 8 Structural characterization of single-crystalline ZGO nanorings. (a-b) Low magnification TEM images showing the circular ring-shaped structures. (c-e) HRTEM images of different locations of the nanoring, verifying that the entire nanoring is single-crystalline.....	103
Figure 5. 9 Detailed structures of the type I nanorings formed by NW self-welding. (a) TEM image and (b) ED pattern of a typical single-crystalline type I nanoring. (c) Enlarged view of the tip-backbone joint section. Au catalyst can be viewed at the growth front. (d,e) HRTEM images of the joint sections, showing the defect-free crystallographic structure. Inset in (e) is the schematic diagram of the type I nanoring formation processes.	105
Figure 5. 10 SEM images of the branched NW heterostructures after a secondary ZnO branch growth at 520 °C. (a) Low magnification image. (b-e) High magnification images showing the well-aligned ZnO branches. The arrows and numbers in (d) and (e) indicate the 6-fold symmetry of the branches, as viewed from the (d) top and (e) side. (f) Enlarged view of the branches, showing the coalescence at the bottom. (g) View of 6-fold symmetry from the top, as indicated by dashed lines.	108
Figure 5. 11 XRD patterns of the nanostructures (a) before and (b) after secondary ZnO deposition. While a pure ZGO phase was detected before growth, an additional ZnO was detected after secondary deposition.	109
Figure 5. 12 (a) Low magnification TEM image of the branched heterostructures. (b) Enlarged view of the branches. Arrows indicate the coalescence between thin NWs. (c) Enlarged view of an individual ZnO branch, with its HRTEM image shown in (d). Inset in (c) is the corresponding FFT pattern. The ZnO branch NWs grow along [001] direction. (e) EDS spectrum recorded from the whole heterostructures in (a). (f) EDS line scanning profiles confirming the ZGO backbone NW with ZnO branches.	110
Figure 5. 13 SEM images showing the heterostructure morphologies grown at (a,b) 560 °C and (c,d) 480 °C. (e) Statistical results showing the branch lengths and branch widths as a function of growth temperature.	112
Figure 5. 14 (a) TEM image of a ZGO backbone with ZnO nuclei. (b-d) HRTEM image and corresponding FFT patterns of the interface. (e-g) TEM image and FFT patterns showing the consistent crystallographic relationship between ZGO and ZnO. (h) Structure defects such as misfit dislocations were observed at some of the ZGO-ZnO interface to release strain.	113

Figure 5. 15 Schematic models of (a) hexagonal ZGO lattice and (b) the epitaxial relationship between (001) surface of ZnO and (1-10) surface of ZGO. The red rectangles show the lattices of ZGO (1-10) plane.....	115
Figure 5. 16 Schematic illustration of structure evolution of the branches (red color) under different growth temperatures. The temperature dependent nucleation rates and lateral growth rates lead to the formation of distinct nanobelt and NW branches.	116
Figure 5. 17(a) Schematic diagram of the UV photodetector using ZGO NW networks. (b) I-V characteristics of the device in dark (black squares) and upon 0.2 mW/cm ² (red circles) 254 nm UV illumination. Inset is a typical SEM image of the NW network between electrodes. Scale bar is 5 μm. (c) Photoresponse characteristics showing the reversible switching behavior when the 0.2 mW/cm ² 254 nm UV light is turned on and off repeatedly. (b) Enlarged view of a single on/off cycle showing the fast response and reset time within 1 s.	119
Figure 5. 18 (a) Photoresponse behavior of the device under UV illumination of 254 nm (red line) and 365 nm (black line). (b) Schematic of the carrier generation and NW-NW junction barrier for electron transfer in the network device.	121

CHAPTER 6

Figure 6. 1 XRD pattern of the indium germanate nanostructures. Both the IGO and In phases were detected. Red rectangles indicate the three peaks belong to In.	130
Figure 6. 2 SEM images of IGO semi-nanotubes. (a) low magnification of cross-section view; (b-d) high-magnification of the nanotubes revealing the semi-tubular structure and catalyst particles at the front. Inset in (d) shows an open end of a single nanotube. Scale bar is 100 nm.....	131
Figure 6. 3 (a,b) TEM images of semi-nanotubes with more than half tube-walls; (d,e) TEM images of semi-nanotubes with less than half tube-walls; (c,f) corresponding schematic illustrations of the semi-nanotubes.	132
Figure 6. 4 (a,b) HRTEM and SAED of semi-nanotube grow along <-121> direction; (c,d) HRTEM and FFT of semi-nanotube grow along <1-1-1> direction.	133
Figure 6. 5 EDS spectra of the (a) catalyst tip and (b) NW body of the semi-nanotubes.....	134
Figure 6. 6 (a) Binary phase diagram of Ge-In, showing that a higher In concentration is required if the liquid alloy were to solidify at a lower temperature; (b) germanium concentration gradient at the liquid-substrate interface (a circle with a diameter of 200 nm). The cap of the liquid droplet is omitted for clarity; (c) schematic illustration of the semi-nanotube nucleation and growth processes.....	135
Figure 6. 7 (a,b) SEM images of the as-synthesized NWs on substrates; (c) XRD pattern of the indium germanate NWs.	137
Figure 6. 8 (a) Low magnification TEM image of the IGO NW with metal catalyst particle at the front; (b) HRTEM image of NW segment below catalyst; (c) lattice-resolved HRTEM image of the NW; (d) two dimensional Fourier transform along [110] zone axis; (e) corresponding SAED pattern of the NW.	138
Figure 6. 9 (a) Low magnification SEM image of the IGO nanoribbons; (b,c) magnified SEM images showing the curved nanoribbon morphology; (d) SEM image of the nanoribbon cross-section; (e) low magnification optical microscopy image showing the ultra-long nanoribbons.....	140
Figure 6. 10 (a) TEM image of a single IGO nanoribbon; (b) SAED pattern of the nanoribbon along [100] zone axis; (c,d) TEM images showing the cross-sections of the nanoribbons; (e) HRTEM image and (f) EDS spectrum of the nanoribbons.	141

Figure 6. 11 (a) Low magnification SEM image of the hierarchical IGO nanostructures; (b-d) magnified SEM images showing IGO NWs growing on micro-crystals; SEM image of the (e) parallel and (f) crossed NW configurations.	145
Figure 6. 12 (a) TEM image of the hierarchical IGO nanostructures; (b,c) magnified TEM images of the tip and bottom of the NW array; (d) representative TEM image of the bottom of a single NW growing on micro-crystal; (e-g) HRTEM images of the NW with locations indicated in (d). Inset in (e) is the corresponding two dimensional Fourier transform recorded along [110] zone axis.	146
Figure 6. 13 (a) Linear and (b) logarithm plot of the spectral response in single IGO nanobelt device. (c) Linear and (d) logarithm <i>I-V</i> curves of the device in dark and under 230 nm light illumination. Insets in (a) and (c) are schematic and SEM image of the device. <i>(This data was acquired by our collaborator Dr. Li Liang in NIMS-MANA, Japan)</i>	148
Figure 6. 14 (a) Photo-switching behavior of the IGO nanobelt devices under 230 nm light illumination ($19 \mu\text{W cm}^{-2}$) at a bias of 10 V. (b) Enlarged view of single cycle showing the fast response and reset time < 1 s. (c) High-frequency (100 Hz) switching characteristics. The reference signal is also shown for comparison. (d) Photoresponse in air and under different vacuum conditions. <i>(This data was acquired by our collaborator Dr. Li Liang in NIMS-MANA, Japan)</i>	150

List of Tables

Table 2. 1 Material characteristics of several typical semiconductors. ⁴⁴	28
Table 6. 1 Summary of the growth conditions for the 4 types of typical IGO nanostructures.	129

Abstract

This thesis focused on the synthesis of Ge-based one-dimensional (1D) nanostructures for photodetector applications. We presented the comprehensive studies of controllable syntheses of Ge-based nanostructures, including Ge nanowires (NWs), zinc germanate ($\text{Zn}_2\text{Ge}_2\text{O}_4$, ZGO) NWs and indium germanate ($\text{In}_2\text{Ge}_2\text{O}_7$, IGO) nanostructures. Photodetector using those novel nanostructures were fabricated and studied, aiming to achieve high wavelength selectivity, high photoresponse time and low fabrication cost.

GeNWs were synthesized in a horizontal high temperature furnace using both conventional Au and novel Bi catalysts. The growth conditions were carefully optimized to achieve the best NW yield. Morphology, crystal structure and chemical compositions of the NWs were characterized using various instruments. Photodetectors based on single GeNW and NW networks were fabricated and studied. Network devices with facile fabrication processes exhibited greatly enhanced photoresponse time than single NW devices and are considered as alternative solutions for further large scale production.

Ternary germanates with wide bandgaps are of particular interests for photodetector applications with high wavelength selectivity. We presented the controllable syntheses of two novel ternary germanates: ZGO and IGO. Based on our understandings of the underlying mechanisms, excellent control of the nanomaterial growth and structural evolution processes were achieved. High-quality germanate nanostructures and their corresponding heterostructures were synthesized and used for photodetector applications. High wavelength selectivity and photoresponse time were observed in those devices, indicating a promising application potential for those novel nanomaterials.

CHAPTER 1 Introduction

1.1 Background

“There is plenty of room at the bottom”, said Richard Feynman in 1959. Indeed, the dream of constructing nanomaterials at the atomic scale has inspired consistent efforts of global scientists into the field of nanotechnology. Exciting progress has been made in the past few decades. Engineering and manipulation of the nanostructures are producing materials with unprecedented unique properties, which are of great interest both for fundamental understanding and technological applications.

Materials with at least one of the dimensions in nanoscale are treated as nanomaterials. Consequently, the nanomaterials can be categorized into several types, typically including two-dimensional (2D) nanostructures (such as thin films), one-dimensional (1D) nanostructures [such as nanowires (NWs) and nanotubes] and zero-dimensional (0D) nanostructures (such as nanoparticles). Among them, 1D nanostructures, with anisotropic elongation in one dimension, are of particular interest.

Until now, various types of 1D inorganic nanostructures were reported in literature, for example, NWs, nanotubes, nanobelts, nanotapes, nanosprings and their heterostructures (Figure 2.1). A schematic summary of the quasi-1D nanostructures is shown in Figure 2.1.¹

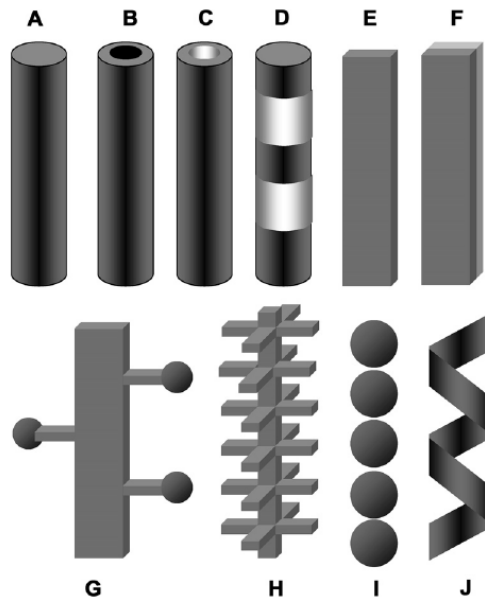


Figure 1. 1 A schematic summary of the quasi-1D nanostructures. (a) NWs; (b) core-shell NWs; (c) nanotubes; (d) axial heterostructures; (E) nanobelts; (F) nanotapes; (G) dendrites; (H) hierarchical nanostructures; (I) nanosphere assembly; (J) nanosprings.¹

1D nanostructures, as a unique class of materials, are advantageous for many important applications compared with their 2D or 0D counterparts. For example, semiconductor NWs and nanotubes with high aspect ratios are extensively investigated for nanoelectronic applications. Field-effect transistors fabricated using semiconductor NWs were widely reported in literature. However, those 0D nanostructures (such as nanoparticles) are not ideal building blocks for nanoelectronic circuits, due to the difficulty to connect the electrodes using nanoparticles. 1D nanostructures are also better choices than their 2D counterparts (such as thin films) in nanoelectronic devices. For example, NW sensors are expected to show improved performances (such as higher sensitivity and faster response time) than thin film nanosensors due to the much higher surface area. Higher surface area means more exposure to the ambient environment and hence more prominent change of electronic properties under the otherwise identical conditions, which is of crucial importance for chemical and light sensors.

NWs are also considered as superior structures for energy conversion and harvesting, such as applications in Li-ion batteries and solar cells. The 1D structure of the NWs provide direct electron paths to the current collector, ensuring fast electron transfer and hence improved performances. For example, researchers have demonstrated that Li-ion batteries using Si NW electrodes can reach the theoretical performance, which is almost 10 times of the conventional carbon electrodes.² However, batteries using Si nanoparticle or thin film electrodes can rarely reach such high performance due to the difficulty in pulverization and hence low utilization of the materials. Analogously, the NWs also showed superior performances than the nanoparticles in dye-sensitized solar cells.³

The 1D geometry of NW allows the construction of complex nanostructures and hence functionalities. For example, thin film can be stacked layer by layer to enrich its functionality. Similar layer by layer coating on nanoparticles forms the core-shell nanoparticles. While this can be easily achieved in NWs (i.e., the formation of core-shell NWs), there are much more structural variations that could be achieved due to its unique geometry. Until now, various heterostructured NWs have been reported, such as core-shell NWs, axial heterostructured NWs, branched nanotrees and side-by-side nanotapes. The abundant structural variations in NWs greatly enrich their properties, enabling the fabrication of novel nanodevices.

1.2 Objectives and Motivation

Numerous efforts have been devoted to the syntheses and applications of 1D nanostructures in the past decades. Significant progresses have been made in understanding their growth mechanism, developing novel synthetic method, investigating their unique optical, electronic or magnetic properties and integrate those nanostructures into functional nanodevices.

However, many challenges are yet remaining to be solved to further advance their practical applications.

1.2.1 Controllable Synthesis of Complex Nanomaterials

One important issue requiring further efforts is the controllable synthesis of 1D nanostructures of novel materials, such as ternary complex oxides. While most of previous research in literature was focusing on elemental or binary materials, more complex ternary materials have received little attention, probably due to the complexity of morphology and composition control. Recently, ternary nanostructures have attracted increasing interest due to their interesting optical and electronic properties which are usually unavailable in elemental or binary compounds. Compared with binary oxide materials (*e.g.*, ZnO, SnO₂), ternary oxides with unique optical and electronic properties are of special interest for specific applications. Until now in the literature, 1D nanostructures of ternary ZnO-based materials has been widely studied, due to the wide interest in ZnO.⁴ The 1D nanostructures were mainly fabricated by 2 methods: solid state reaction and vapor phase deposition.

Solid state reaction is a facile and versatile method to fabricate ternary nanostructures. For example, a layer of a second material (such as Al₂O₃) can be coated on the 1D NW template (such as ZnO). Annealing at high temperature will promote the atomic inter-diffusion and lead to the formation of ternary nanostructures, such as ZnAl₂O₅.⁴ Based on the different preferential diffusion behavior or different material combinations, various ZnO-based ternary nanostructures (such as NWs, nanotubes, nanochains, nanobrushes) have been reported.⁴ However, solid state reaction has several drawbacks. First, although single-crystalline spinel nanotubes were previously reported, most of the nanostructures obtained via solid state reaction are poly-crystalline. Single-crystalline structures are usually preferred for property

studies and device applications. Second, it is difficult to obtain high purity ternary nanostructures by solid state reactions. For example, the shell thickness of Al_2O_3 can be precisely controlled when using atomic layer deposition (ALD), however, the diameter of ZnO NW templates varied in a large range, which results in either excess or insufficient Al_2O_3 to form stoichiometric ZnAl_2O_5 . The conditions would be even worse when the shell was deposited by other methods such as physical/chemical vapor deposition, where it is hard to achieve uniform shell deposition.

Vapor phase deposition is another commonly used method for ternary oxide fabrications. The method is similar to those previously used for binary oxide (such as ZnO, SnO_2 , In_2O_3) synthesis, except that the evaporation and deposition process is more complex. Until now, several ternary nanostructures synthesized by vapor phase deposition were also reported, such as ZnGa_2O_4 and Zn_2SnO_5 .⁴ As well known in the NW literature, nanostructures grown by direct vapor phase deposition are usually single-crystalline, as have also been observed in the ternary oxide NWs. The high crystallinity of the NWs is one of the appealing aspects of vapor phase deposition. However, there are still several issues to be addressed in this method. First, formation of impurity phase is also one of the critical issues to be solved. Due to the different physical and chemical properties of the source materials, it is more complex a process to control the evaporation and deposition kinetics. For example, ZnGa_2O_4 NW synthesized by co-evaporation of ZnO and Ga_2O_3 powders were previously reported,⁵ however, significantly ZnO phases were observed besides the desired ZnGa_2O_4 phase. This is actually also commonly encountered in other reports, where one of the binary oxide phases was also observed apart from the desired ternary phase. It is of great importance to achieve high purity NW growth in further studies, in order to remove their potential influence in property studies and device applications.

The strong interest in controllable synthesis of novel nanostructures has driven us to perform the systematic studies in Ge-based 1D nanostructures: syntheses and applications. Ge is considered as a promising alternative material for future high-speed nanoelectronic devices due to its high carrier mobility and compatibility with Si. Ge-based complex compounds, such as ternary germanates, are also of strong interests for innovative nanoelectronic and optoelectronic applications, such as photodetectors.

1.2.2 High-Performance NW Photodetectors

Photodetector is an important application of NW optoelectronic devices. For potential commercialized NW photodetectors, it is crucial that the devices have high sensitivity, high selectivity, fast response time, low cost and long cyclic time. Although NW photodetectors are expected to exhibit superior performances than their bulk or thin film counterparts, the performances of NW devices reported until now are not quite satisfactory. There are still several critical issues remain to be addressed before NW photodetectors can be put into large scale industrial usage.

First, most of the photodetectors are utilizing single NW as the detection channels. However, scalable fabrication of single NW devices is currently hindered by the difficulty of controllable NW alignment and addressing. Although several techniques have been developed to, for example, align NWs along a unidirection, satisfactory methods to address individual NW are still lacking. Moreover, the cost of single NW device fabrication would be quite high, probably due to the delicate aligning techniques required and lithography steps.

One solution is of course to develop facile and low cost NW alignment methods, which is still facing significant challenges although remarkable progresses have been made.⁶ Another alternative solution is that instead of single NW, NW networks can be used as active detection channels. No alignment is required for network devices, and this might be an excellent way to overcome the alignment obstacle if the network devices perform well.

Second, fast photoresponse time is a critical requirement for industrial applications, for the efficient tracing of light changes. However, the photoresponse for single NW devices are usually on the order of several minutes and even up to hours. The slow response and reset time is usually associated with the slow oxygen adsorption and desorption processes,⁷ since Ohmic contacts were usually observed in those devices and the resistance is dominated by the NW itself.

One promising solution to achieve fast response time is to create asymmetric contacts in the NW devices, leading to Schottky instead of Ohmic conductance. In Schottky devices, the resistance is dominated by the NW/electrode junctions, which successfully avoided the problem of slow oxygen adsorption/desorption processes. Some examples of creating Schottky contacts in ZnO UV sensors using FIB have been reported.⁷ However, it should be highlighted that FIB is a quite expensive and low output method, which cannot be used for large scale productions. Nevertheless, the reports may shed light on some other promising methods, by transferring the dominate device resistance to some other places, such as contact junctions.

Third, good wavelength selectivity is also highly desirable for industrial applications. Although Ge with a small bandgap can be used for the detection of ultraviolet light, it is not a

superior choice when good wavelength selectivity is required. Binary oxide materials usually show good wavelength selectivity to UV light due to their wide bandgaps and visible-blind photodetectors can be readily fabricated using oxide NW detection channels.

To date, research in ternary oxide NWs with even larger bandgaps than those of binary oxides is very limited. However, ternary oxides are promising candidates with excellent wavelength selectivity. For example, zinc germanate (Zn_2GeO_4 , ZGO) with a bandgap of 4.68 eV are only expected to response to light with wavelength below 265 nm. Those novel ternary oxide NWs will show excellent wavelength selectivity which are especially useful for deep-UV detection. One of the future research directions is to achieve controllable growth of novel ternary oxide NWs, which can be integrated for photodetectors with good wavelength selectivity.

1.3 Research Approaches

In this study, we use vapor phase deposition to synthesize 1D Ge-based nanostructures, aiming to achieve high quality nanostructure growth with high purity, high crystallinity and high degree of structural control. Comprehensive studies on the controllable growth of GeNWs, zinc germanate NWs and indium germanate NWs are demonstrated. NW photodetectors based on those novel 1D nanostructures are presented. Our research focused on the exploration of NW photodetectors with low fabrication cost, fast photoresponse time and high wavelength selectivity.

First we presented our studies on the growth of GeNWs in our horizontal quartz furnace. Various growth parameters were carefully optimized, in order to obtain the best NW yield and more importantly to provide guides for the synthesis of other nanostructures. Detailed

morphology, crystal phase and chemical compositions of the NWs were characterized using X-ray diffraction (XRD), scanning electron microscopy (SEM), transmission electron microscopy (TEM) and energy dispersive spectroscopy (EDS). Those GeNWs were used in visible light photodetectors. With the purpose of lower device fabrication cost while maintaining high performance, we have successfully demonstrated the usage of NW networks as superior detection channels over single NW. The NW devices were fabricated using photolithography and focused-ion-beam (FIB) techniques. The photodetectors were characterized using in a Keithley semiconductor parameter analyser system. Tungsten-halogen lamp with tunable light intensity embedded in the probe station is used as the incident visible light source.

Zinc germanate (Zn_2GeO_4 , ZGO) is an interesting wide bandgap semiconductor, which may function as efficient UV photodetectors. With experiences from the synthesis of GeNWs, we have also demonstrated the successful growth of high purity ZGO NWs and their corresponding superstructures (kinked ZGO NWs and nanorings) and heterostructures (branched ZGO-ZnO heterostructures). Analogously, the morphology, crystal structures and chemical compositions of ZGO NWs and their derived complex structures were all carefully characterized. ZGO NW photodetectors were fabricated and were found to exhibit excellent performances than previous reports, such as fast response and reset time and excellent wavelength selectivity.

Indium germanate ($\text{In}_2\text{Ge}_2\text{O}_7$, IGO) nanostructures with tunable morphologies were synthesized and characterized. Novel IGO nanostructures, including semi-nanotubes, NWs, nanobelts and 3D hierarchical nanostructures were successfully synthesized via proper control of the growth conditions. Detailed growth mechanisms were also discussed to provide

deep understandings of the growth processes. Solar-blind UV photodetectors based on IGO nanobelts with wide bandgap were demonstrated as high-performance devices.

1.4 Thesis Overview

This thesis presents the synthesis of Ge-based 1D nanostructures for photodetector applications. We focused on the understanding of their growth mechanisms to achieve decent morphology control. Their integration into nanoscale optoelectronic devices will also be demonstrated.

In Chapter 1, we presented the research background and motivations for this thesis. The research progresses and future directions related to our studies are briefly introduced. We also give an overview of our research approaches, as well as introductions of the main content of each chapter.

In Chapter 2, we present the research progresses of 1D nanostructures in literature. 1D nanostructures, as a unique class of nanomaterials, were extensively studied for various applications ranging from nanoelectronics, optoelectronics to energy conversion. Especially, we introduce the research interest in Ge-based nanostructures, due to their attractive properties and applications in nanodevices. The research progress and future directions in using 1D nanostructures for photodetectors are also introduced.

In Chapter 3, we introduce the experimental methods used in this thesis, including the NW synthesis/characterization and device fabrication/characterization methods. The NWs were grown in a high-temperature quartz tube system. The nanostructures were thoroughly characterized using XRD, SEM, TEM and EDS. Photodetectors were fabricated mainly using

photolithography and FIB. Device performances were measured using a semiconductor analyzer with additional light sources.

In Chapter 4, we present the synthesis and characterization of elemental Ge NWs. Apart from the conventional Au catalysts, we found that Bi can also serve as efficient metal catalysts to direct GeNW growth by chemical vapor deposition. Visible light photodetectors based on GeNWs were fabricated. Photodetectors with NW network as detection channels showed much faster photoresponse time than those single NW devices. The detailed conduction and detection mechanisms are discussed.

In Chapter 5, we present the synthesis and characterizations of ternary ZGO NWs and their corresponding heterostructures. Chemical vapor deposition of high density ZGO NWs and the structural characterizations are presented. We also demonstrate that kinked ZGO NWs and nanorings can be readily synthesized via pressure modulation. All the kinked superstructures and nanorings are single-crystalline without defects. ZGO NW based branched ZGO-ZnO heterostructures are also successfully synthesized via a secondary deposition method. ZGO NW network photodetectors are fabricated and exhibit fast response time and good wavelength selectivity for deep-UV photodetection.

In Chapter 6, we present the morphology controlled synthesis of indium germanate ($\text{In}_2\text{Ge}_2\text{O}_7$) nanostructures. With a good understanding of the nanostructure growth mechanisms, excellent morphology control of the nanostructures was achieved. For example, $\text{In}_2\text{Ge}_2\text{O}_7$ nanostructures with various morphologies were fabricated, including semi-nanotubes, NWs, nanobelts and hierarchical structures. Indium germanates are typical wide-bandgap

semiconductors, and can be used for solar-blind photodetectors. Detailed optoelectronic characterizations of the IGO nanobelt photodetectors are presented.

In Chapter 7, we summarize our work in the thesis and give some suggestions for future work.

References:

- (1) Kuchibhatla, S.; Karakoti, A. S.; Bera, D.; Seal, S. *Progress in Materials Science* **2007**, *52*, 699-913.
- (2) Chan, C. K.; Peng, H. L.; Liu, G.; McIlwrath, K.; Zhang, X. F.; Huggins, R. A.; Cui, Y. *Nature Nanotechnology* **2008**, *3*, 31-35.
- (3) Law, M.; Greene, L. E.; Johnson, J. C.; Saykally, R.; Yang, P. D. *Nature Materials* **2005**, *4*, 455-459.
- (4) Fan, H. J.; Yang, Y.; Zacharias, M. *Journal of Materials Chemistry* **2009**, *19*, 885-900.
- (5) Feng, P.; Zhang, J. Y.; Wan, Q.; Wang, T. H. *Journal of Applied Physics* **2007**, *102*.
- (6) Wang, M. C. P.; Gates, B. D. *Materials Today* **2009**, *12*, 34-43.
- (7) Zhou, J.; Gu, Y. D.; Hu, Y. F.; Mai, W. J.; Yeh, P. H.; Bao, G.; Sood, A. K.; Polla, D. L.; Wang, Z. L. *Applied Physics Letters* **2009**, *94*.
- (8) Lewis, J. S.; Holloway, P. H. *Journal of the Electrochemical Society* **2000**, *147*, 3148-3150.
- (9) Liu, Z. S.; Jing, X. P.; Wang, L. X. *Journal of the Electrochemical Society* **2007**, *154*, H500-H506.
- (10) Bender, J. P.; Wager, J. F.; Kissick, J.; Clark, B. L.; Keszler, D. A. *Journal of Luminescence* **2002**, *99*, 311-324.
- (11) Sato, J.; Kobayashi, H.; Ikarashi, K.; Saito, N.; Nishiyama, H.; Inoue, Y. *Journal of Physical Chemistry B* **2004**, *108*, 4369-4375.
- (12) Huang, J. H.; Wang, X. C.; Hou, Y. D.; Chen, X. F.; Wu, L.; Fu, X. Z. *Environmental Science & Technology* **2008**, *42*, 7387-7391.
- (13) Tsai, M. Y.; Yu, C. Y.; Wang, C. C.; Perng, T. P. *Crystal Growth & Design* **2008**, *8*, 2264-2269.

CHAPTER 2 Literature Review

2.1 Syntheses and Applications of 1D Nanostructures

In this section, we provide a review of NW growth mechanisms and several typical groups of materials that have been investigated. With special focus on Ge-based 1D nanostructures, we provide the updated literature review of elemental, binary and ternary Ge-based nanostructures and applications. Finally, literature progresses on 1D nanostructure photodetectors are also summarized. The research progresses of using small bandgap semiconductors (such as Ge), wide bandgap semiconductors (typically binary oxides) and ternary materials with even larger bandgaps were introduced.

2.1.1 Growth Mechanisms

Various synthetic methods have been employed to synthesis semiconductor nanowires (NWs), mainly including vapor-solid (VS), oxide-assisted growth (OAG), vapor-liquid-solid (VLS), vapor-solid-solid (VSS) and solution phase synthesis.

Vapor-solid (VS) mechanism

During VS process, vapor-phase growth species directly condense into solid NWs, due to the anisotropic crystal structure or template effect. This process avoids the usage of metal catalysts as those in VLS process, which may introduce contamination into the NWs. However, it is difficult to achieve controlled growth via this mechanism. For example, the NW diameters in most cases are randomly distributed, which make it undesirable for further device processing and applications. In most cases, oxide materials can be grown through the VS mechanism. Su *et al.* reported the synthesis of IGO nanobelts via thermal evaporation through a VS growth mechanism.¹ Han *et al.* reported the growth of novel ZnO nanocones

arrays by low temperature evaporation of Zn powder, and the ZnO nanostructures grew through VS mechanism.² Wang *et al.* reported the successful synthesis of In_2O_3 and SnO_2 nanobelts, NWs and nanodiskettes through VS mechanism.^{3,4} Typical TEM images of the ZnO nanobelts are shown in Figure 2.1.⁴

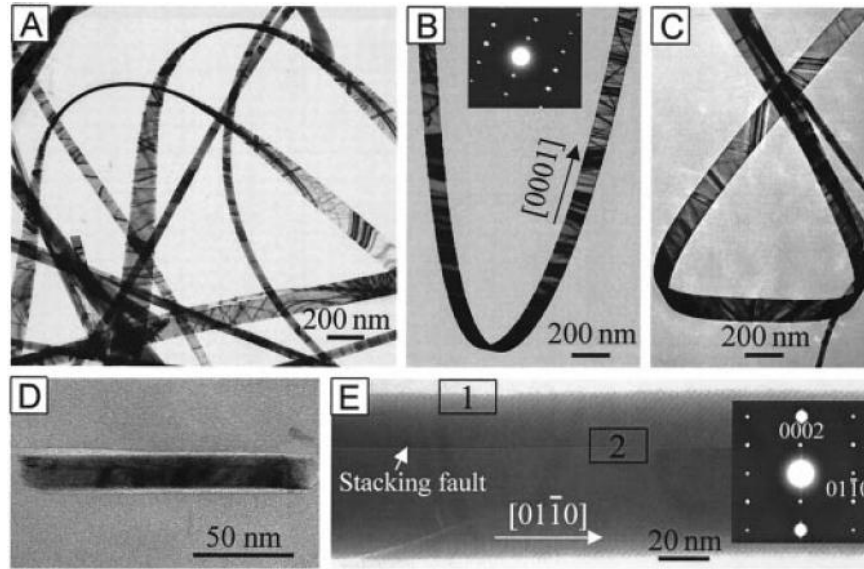


Figure 2. 1 (a-c) Typical TEM images of ZnO nanobelts. (d) Cross-sectional TEM images of a ZnO nanobelts. (e) ZnO nanobelt with stacking fault.⁴

Oxide-assisted growth (OAG)

NWs fabricated through OAG mechanism was first reported by Lee. S. T. group.⁵ The advantage of OAG lies in the absence of external catalysts to direct the NW growth. Unlike VS mechanism which is mostly applied to oxide materials, oxide-assisted growth only succeed in several groups of materials with proper oxide forms. The NWs synthesized through OAG process are usually poly-crystalline or have twin-boundaries. A thick oxide outlayer would always be found surrounding the NWs, which is intrinsic to this mechanism, and this may hamper the potential applications which require no oxide layer on the surfaces. Wang *et al.* reported the synthesis of Si NWs by combinational laser ablation and thermal evaporation methods.⁶ Shi *et al.* reported the synthesis of GaAs NWs by oxide-assisted laser ablation of a mixture of GaAs and Ga_2O_3 .⁷ An overview of the various nanostructures

synthesized via OAG process can be found.⁵ Schematic diagrams of the OAG and VLS processes are shown in Figure 2.2 (VLS mechanism will be introduced in the following part).⁵

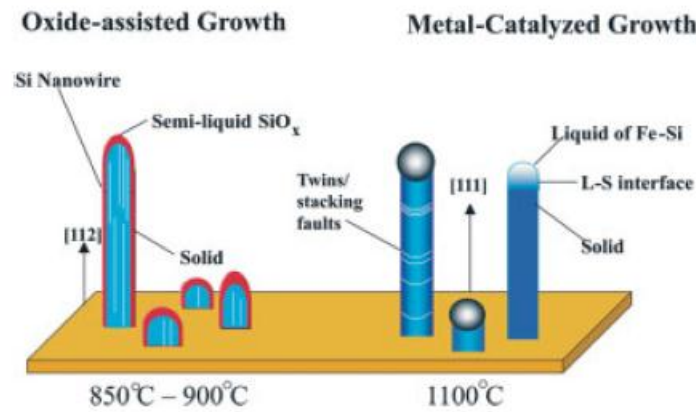


Figure 2. 2 Schematic diagrams of the OAG and VLS growth processes.⁵

Vapor-liquid-solid (VLS) mechanism

Most of the 1D nanostructures, including CNTs and semiconductor NWs, are synthesized through VLS mechanism.⁸ Taking Ge NW as an example, the detailed growth processes of the GeNWs are as follows: 2. Liquidus catalyst particles would form on the substrates as the temperature increases; 2. Gas species (such as GeH_4 or Ge vapor) are introduced into the chamber to initiate the NW growth. For chemical vapor deposition (CVD) using GeH_4 , GeH_4 would decompose with Au as catalysts. Ge species could consequently be adsorbed. For synthesis directly using Ge vapor, the vapor would be preferentially adsorbed to the liquid Au particle surface. 3. Continuous adsorption of Ge vapor would lead to supersaturation of the catalyst particle, followed by precipitation of solid Ge NW at the liquid (catalyst)-solid (substrate) interface. 4. Long NWs can be synthesized if the vapor species are continuous supplied for a certain period. A simplified illustration of Ge NW growth via VLS mechanism is shown in Figure 2.3. One great advantage of VLS mechanism is that it can produce NWs with controlled structures and compositions. It provides excellent control over almost all the

key parameters of the NWs, including chemical composition, structure, size, morphology and doping.⁹

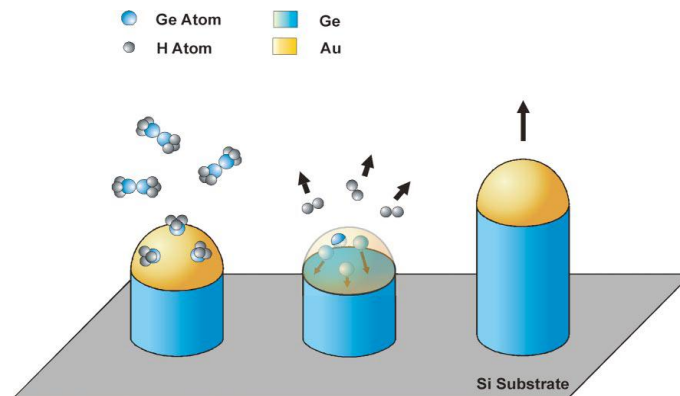


Figure 2. 3 Schematic illustration of the VLS growth processes of GeNWs.

The growth of semiconductor NWs via VLS mechanism can be predicted using binary phase diagrams.¹⁰ The binary phase diagram of Si-Au is shown in Figure 2.4, guiding the thermodynamics of VLS growth. At a certain growth temperature (usually above the eutectic temperature), the Au alloy catalyst particle is in its liquidus form via adsorption of Si. The concentration of Si would increase with continuous adsorption. Solid Si NWs would nucleate and grow when the concentration of Si is higher than the critical value defined by the liquidus line of Si.

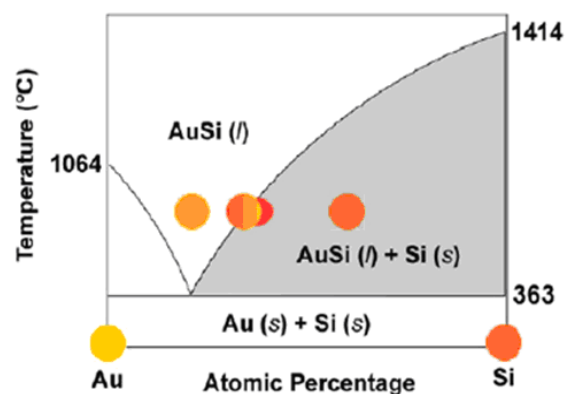


Figure 2. 4 Binary phase diagram for Au-Si.¹¹

The binary phase diagrams for elemental alloy, such as Si and Ge, is simple and assured. But the phase diagrams for catalyst metal with binary or even ternary compound is not readily

available in most cases. This can be solved by using simplified phase diagrams for catalyst and certain component that was incorporated into the catalyst during growth. For example, for the case of Au catalyzed growth of GaAs NWs, the growth conditions can be predicted using the Au-Ga binary phase diagram, since As was observed to be absent from the Au catalyst particle during growth.^{10,12}

Vapor-solid-solid (VSS) mechanism

The process of VSS is similar to that of VLS, where external metal catalysts are used to direct the growth of NWs. The only difference is that the metal particles are in solid state instead of liquid state during growth. The growth rate of VSS is much slower than that of VLS, due to the low affinity of vapor phase to the solid catalyst particle and low diffusion rate through the solid particle.¹²⁻¹⁴ Schematic diagram of the VLS and VSS growth processes are shown in Figure 2.5.¹⁴

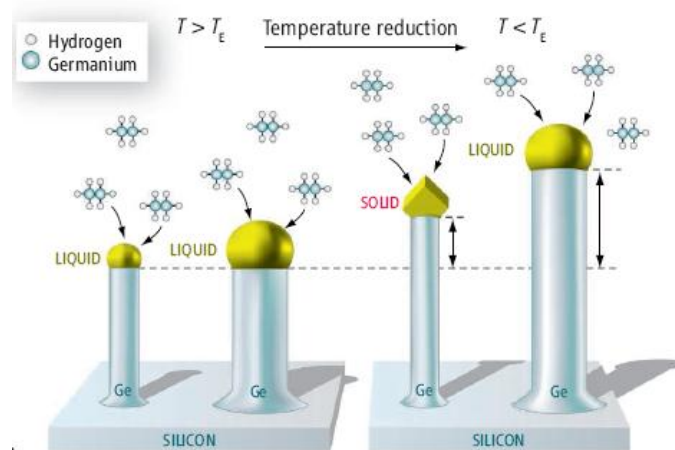


Figure 2. 5 Schematic diagram of the Ge NW growth via VLS and VSS mechanisms. When the temperature decreases, the catalyst may become solid but the growth still proceeds.¹⁴

Solution phase synthesis

All the growth mechanism discussed above involves vapor phase for growth species supply, SLS mechanism is a distinct mechanism where the growth species are supplied in solution.

For NWs synthesized in solution phase, different materials have been synthesized either with or without metal catalysts. Holmes *et al.* reported the controlled synthesis of silicon NWs in solution phase.¹⁵ The diameter of the NWs can be controlled by using Au catalyst particles with different diameters. The growth orientation of the NWs can be tuned by changing the reaction pressure. Hanrath *et al.* reported a similar synthesis process of Si and Ge NWs in high temperature supercritical fluids by thermally degrading organosilane/organogermane precursors with organic-monolayer-protected Au nanoparticles as catalysts.¹⁶ While in most cases, Au is employed as catalysts for NWs growth, Lu *et al.* reported the synthesis of Ge NWs using Bi as catalysts.¹⁷ NWs synthesized in solution phase without catalysts can also be found, Greene *et al.* reported the synthesis of large scale ZnO NW arrays.¹⁸ The advantages of solution phase synthesis include high yield and high purity, but the organic contamination and inferior surface conditions could hamper the potential applications. Typical SEM images of the wafer-scale ZnO NWs grown in solution are shown in Figure 2.6.¹⁸

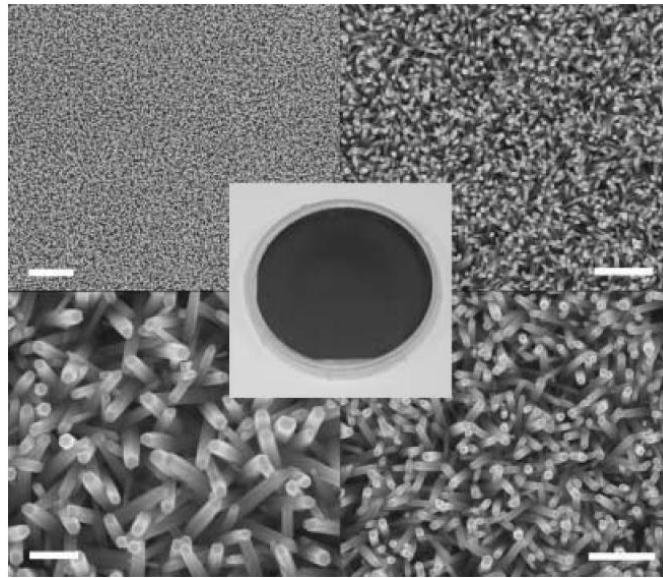


Figure 2. 6 SEM images of the wafer-scale ZnO NW grown in solution.¹⁸

2.1.2 Groups of Materials Investigated

Until now, NWs of a wide range of material have been reported in literature. In general, the inorganic NWs can be categorized into the following groups: 1. elemental NWs, such as Si and Ge; 2. binary phase NWs, such as ZnO, GaAs and NiSi; 3. ternary phase NWs, such as GaInAs and Zn_2TiO_4 . Several review articles give excellent survey of the NW syntheses for various materials.¹⁹⁻²³

Different groups of NWs are of interest for different applications depending on their properties. For example, Si and Ge NW are generally used in nanoelectronic devices (such as FETs and sensors). Oxide NWs (such as ZnO and In_2O_3) can be used for nanoelectronic and nanophotonic applications (such as FETs and photonic circuits). Ternary oxides NWs can be used for luminescent and magnetic applications, depending on the compositions.

One of the most important research aspects in NWs is the fabrication of heterostructures. The capability to change the composition, structure, morphology or doping in the NWs represents a significant step towards complex nanosystems fabrication. Until now in literature, several types of NW heterostructures have been widely investigated, such as the axial heterostructures (segmented NWs), radial heterostructures (core-shell NWs) and branch heterostructures (nanotrees). A schematic diagram of the heterostructures is shown in Figure 2.7. The ability to design and fabricate novel NW structures are especially desired for the realization of various functionalities.²⁴⁻³⁴ The successful synthesis of radial and axial heterostructures show peculiar and interesting electronic and optoelectronic properties that is unavailable with the simple homogeneous NW. The unique properties of the heterostructures will be introduced later.

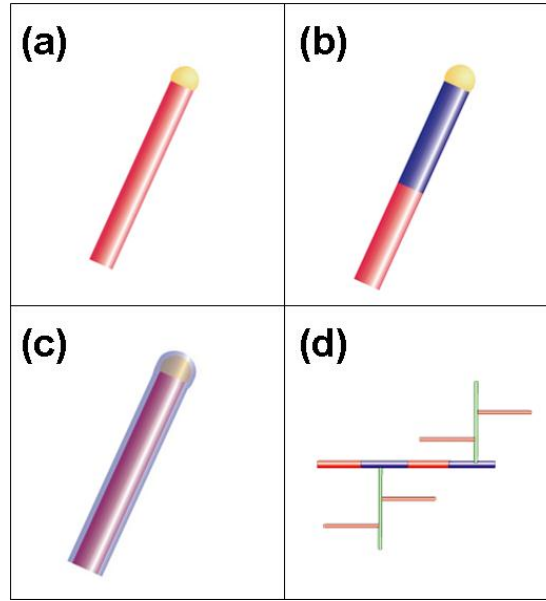


Figure 2. 7 Different configurations of the NWs heterostructures: (a) homogeneous NW structure; (b) axial heterostructure; (c) radial heterostructure; (d) branched heterostructure.⁹

2.1.3 Properties and Applications

There are plenty of reports investigating the properties and applications of 1D nanostructures. In general, there are 3 types of most important applications that NWs have been used for, including nanoelectronic (such as FET, sensor, spintronic devices), nanophotonic (such as photoluminescence, light-emitting diode, waveguiding) and energy conversion (such as Li-ion battery, solar cell, piezotronics, thermoelectric devices). We will explain each application in detail in the following part.

NWs for nanoelectronic applications

Semiconductor NWs were extensively investigated for nanoelectronic applications. The NWs synthesized via the bottom-up method were expected to further shrink the nanocircuit size and allow even larger scale integration, although one of the major problems, large scale NW assembly, still need to be solved. FET based on a single semiconductor NW is a prototype nanoelectronic device. The device configuration and performances based on a single GaN

NW is shown in Figure 2.8.³⁵ A back-gate FET configuration is adopted (Figure 2.8a). I_d - V_d and I_d - V_g characteristics showed good Ohmic and gate-tunable conductance of the NW channel (Figure 2.8b-c). Nanoscale p - n junctions based on a p -Si NW and n -GaN NWs were also demonstrated. While good Ohmic conductance was observed for each single NW, rectified behavior as expected for p - n junction was observed (Figure 2.8d).³⁵

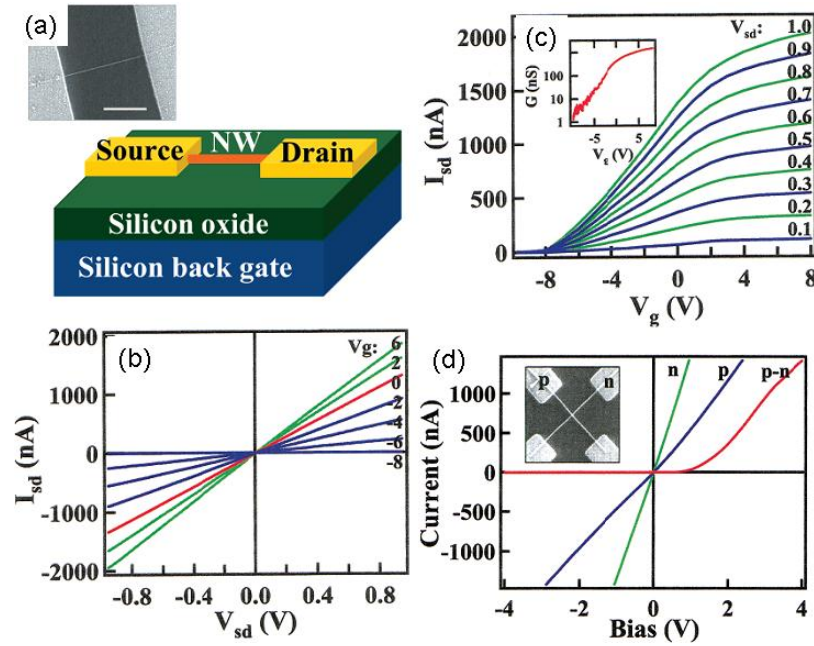


Figure 2. 8 (a) Schematic of a NW FET. (b) I_d - V_d and (c) I_d - V_g characteristics of the NW FET. (d) I-V behavior of n-GaN NW (green), a p-Si NW (blue), and the corresponding n-GaN/p-Si NW junction (red).³⁵

Based on the prototype NW FET, other corresponding electronic devices such as NW sensors can be readily fabricated. Until now, semiconducting NWs have been used as chemical, light and biological sensors. As a typical example, the detection of virus using Si NW sensor is schematically shown in Figure 2.9.³⁶ As shown in Figure 2.9a, the conductance of the Si NW would change when a virus is in contact with the NW surface, due to the gating effect. When the virus detached from the NW, the conductance would restore to its initial value. This enables the real time detection of biological species with ultrahigh sensitivity. The dynamic detection process is further verified by the real time optical microscope observation, as shown in Figure 2.9b.³⁶

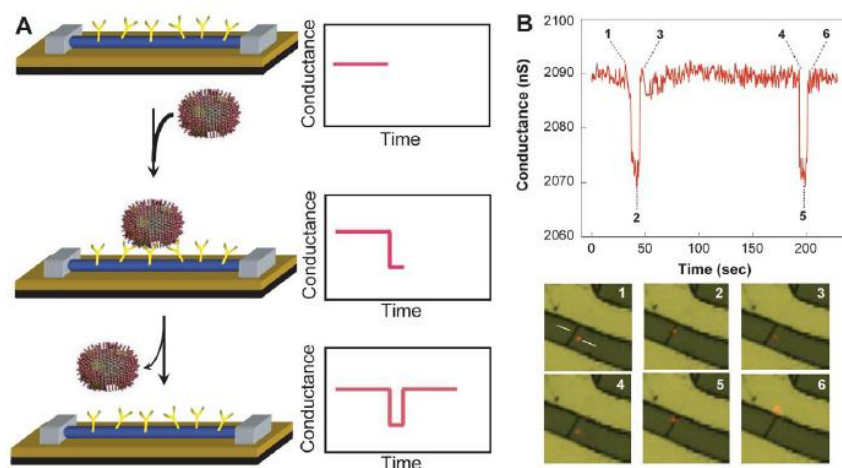


Figure 2. 9 (a) Schematic diagram depicting the detection of single virus using Si NW sensor. (b) Real time observation and the conductance change of the detection process.³⁶

The underlying sensing mechanism for other types of NWs sensors, such as chemical gas and light sensors, are essentially similar with those biological sensors. For example, the NW conductance would also change when exposed to a certain type of reactive gases which can change the surface adsorption conditions and hence conductance of the NWs. For light detector, the photons would generate new carriers in the NW volume and hence change the NW conductance. Until now, various semiconducting NWs (such as Si and ZnO) have been used for chemical, biological or light sensors. Significantly progresses have been made in the field of, for example, understanding the sensing mechanism and improving the sensitivity. Future direction may lie in employing cheap and reliable methods to fabricate NW sensors, as well as the continuous improvement of sensor performances. Until now, there is still no ideal solution for large scale and cost-effective method to produce nanosensors with consistent performances.

Another emerging topic in NW electronic is spintronics, manipulating and utilizing the electron spin states in NWs to achieve novel functionalities. Compared with FET and sensors, research on this aspect is very limited. Some reports on the spin state detection can be found in literature. For example, electron spin state change in helimagnetic MnSi NWs under

external magnetic field has been studied.^{37,38} Analogously, detection of the spin state in Si NWs using magnetic MnSi states has also been demonstrated.³⁹

NWs for nanophotonic applications

Many groups of NWs with interesting optical properties may find interesting applications in nanophotonic devices. Photoluminescence (PL) is a direct and preliminary reflection of the NW optical properties. For example, most of the oxide NWs were found to be luminescent, with light emission ranging from ultraviolet to infrared. Also, another very interesting point is that NWs were found to be able to emit lasers besides the broad-band light. Typical light emission spectra from vertically aligned ZnO NWs are shown in Figure 2.10.⁴⁰ When a pumping light with low power was used, continuous emission was observed (Figure 2.10A-a). Lasing emission was observed when the pumping power was increased above the lasing threshold, and the emission intensity increases with pumping power (Figure 2.10a-b). The laser with ultra-narrow line widths indicates the stimulated emission in the NWs, which is as a result of the preferential amplification effect.⁴⁰

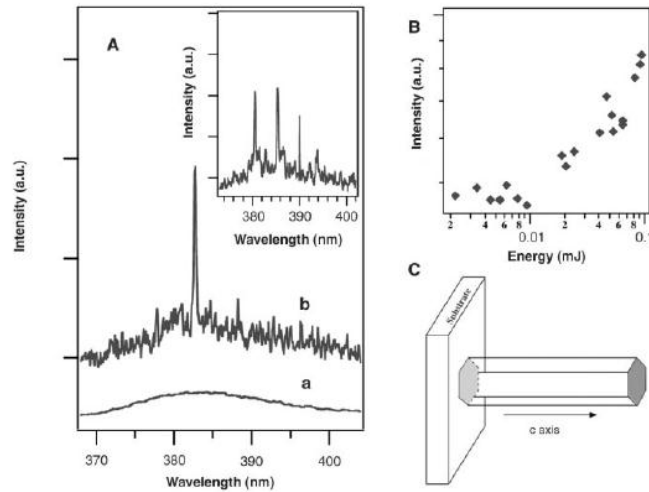


Figure 2. 10 (a) Emission spectra from ZnO NW arrays below (curve a) and above (curve b and inset) the lasing threshold. (b) Emission intensity as a function of optical pumping energy intensity. (c) Schematic illustration of a NW resonance cavity.⁴⁰

NWs were also used as building blocks in light-emitting-diodes (LEDs) and nanophotonic circuits. NWs are considered as important components in future integrated photonic circuits.⁴¹ For example, recently a future nanophotonic circuits for chemical analyses is proposed.⁴¹ A schematic diagram of the circuit is shown in Figure 2.11.⁴¹ The components are explained as following: 2. NW solar cell as on-chip power supply; 2. NW LED as light sources; 3,4. NW as waveguides and filters; 5,6. analysis chamber; 7. NW photodetector.

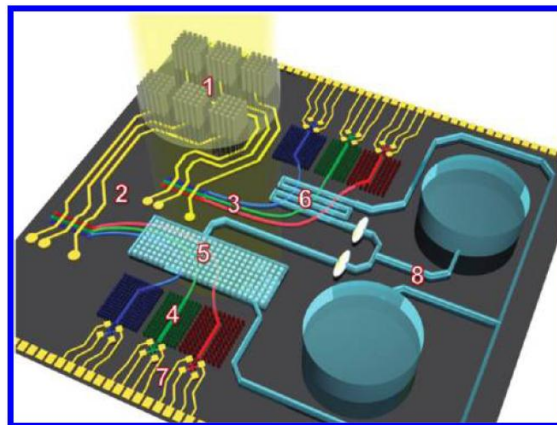


Figure 2. 11 Future integrated nanophotonic circuits for chemical analysis.⁴¹

In this proposed integrated circuit, NWs are playing vital roles in power supply, light generation, light transport and light detection. The 3 types of main applications that NWs

have been used for are fully utilized in this circuit. Among them, energy conversion and harvesting will be discussed in the following part.

NWs for energy conversion and harvesting

NWs are also considered as promising materials for energy conversion and harvesting. The one-dimensionality of the NWs makes them superior candidates for many important energy conversion applications, when compared with their 2D or 0D counterparts. Until now, NWs of different groups of materials have been used for several types of important applications, such as Li-ion batteries, supercapacitors, solar cells, piezotronic nanogenerators and thermoelectric circuits.

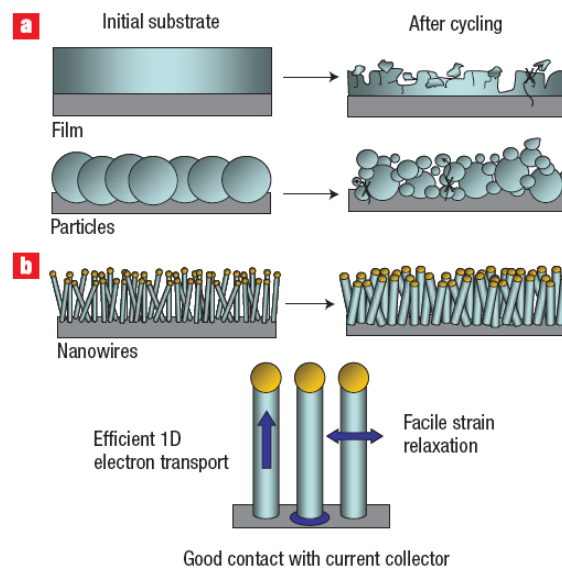


Figure 2. 12 Schematic of morphological changes that occur in Si during electrochemical cycling.⁴²

First we introduce the application of Si NWs in Li-ion batteries. Schematic of the morphological changes for 3 different types of Si structures (film, particles and NWs) are shown in Figure 2.12.⁴² The volume of Si anodes changes by about 400% during electrochemical cycling, which is one of the major problems to achieve the high theoretical performance of Si anodes. The Si films and particles tend to pulverize during cycling, leading to serious performance degradation. However, NWs can minimize the problem to some

extent. For example, the pulverization problem for NWs is less severe than that for thin and particles. The spacing between NWs allows increase in volume and the NWs do not break. Also, each NW is in direct contact with the underlying current collector. The NW itself can serve as an efficient electron transport path to the current collect, resulting in a higher utilization of the anode materials. Theoretical performance of Si has been achieved using Si NW anodes,⁴² which is almost 10 times the performance of conventional carbon electrodes. However, we have to admit that there still remain quite a lot of problems before Si NWs can be employed for industrial applications. The conductivity of the Si NW degrades significantly after cycling; also the NW breakage problem still exists although it's better than thin films and particles.⁴² Currently researchers are trying to combine the advantages of carbon (long life time) and Si (high performance) by forming a hierarchical structures,⁴³ which may present a future research direction to improve the anode performances.

Nanoscale power sources with ultrasmall sizes are required if we want to produce a self-powered nanodevice. Such nanoscale batteries have been fabricated using coaxial NWs, but this can not be achieved using 0D nanoparticles due to its geometry. The schematic diagram of the coaxial NW solar cell is shown in Figure 2.13a.³¹ Coaxial *p-i-n* Si NWs were synthesized by VLS growth and sequential shell deposition. Then metal pads were selectively deposited on the out shell and inner core, and single NW solar cells were fabricated. An efficiency of 4.2% was achieved on those NW solar cells.³¹ The output voltage and current can be modified by combining several cells in parallel and in series. Those solar cells were shown be able to power the nanosensors and logic gates. Those NW solar cells represent a typical unique application that cannot be readily achieved in other types of nanostructures, such as nanoparticles.

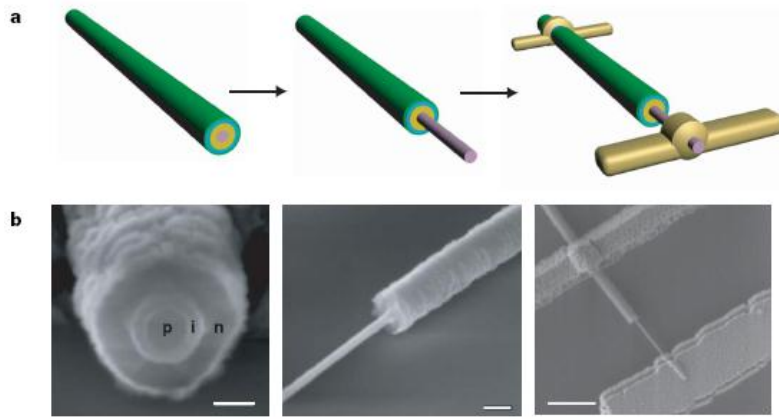


Figure 2. 13 (a) Schematic diagram and (b) SEM images of the coaxial Si NW solar cells.³¹

2.2 Ge-Based 1D Nanostructures

In the above sections, we have discussed the growth mechanism for different groups of materials, as well as their properties and applications. Among the abundant types of materials that have been investigated, we focus on the Ge-based 1D nanomaterials. In the following sections, we will introduce the motivation and current research progress in literature for 3 types of Ge-based nanomaterials (elemental Ge NWs, binary Ge-based NW and ternary Ge-based NWs).

2.2.1 Elemental Ge Nanostructures

Among all the semiconductor materials, group IV materials (Si and Ge) are of special interests since they are compatible with the mainstream Si-based semiconductor technology. Si NWs have been extensively investigated as effective building blocks for nanoscale devices according to the “bottom-up” paradigm. The dominant role of Si in modern microelectronic industries is mainly attributed to the excellent properties of SiO₂. However, compared with Si, Ge is attracting growing interest as alternative channel material due to its high carrier mobility, which makes it promising material for high performance nanoelectronics. A table comparing the physical properties of several typical semiconductors is shown in Table 2.2.⁴⁴

Ge is considered as a superior candidate in future MOFET devices. The Bohr radius of Ge (24.3 nm) is larger than that of Si (4.9 nm), which is expected to allow easier observation of quantum confinement effects, which is important both for fundamental research and practical applications.

Table 2. 1 Material characteristics of several typical semiconductors.⁴⁴

	Ge	Si	GaAs	InSb	InP
Bandgap, E_g (eV)	0.66	1.12	1.42	0.17	1.35
Electron affinity, χ (eV)	4.05	4.0	4.07	4.59	4.38
Hole mobility, μ_h ($\text{cm}^2\text{V}^{-1}\text{s}^{-1}$)	1900	450	400	1250	150
Electron mobility, μ_e ($\text{cm}^2\text{V}^{-1}\text{s}^{-1}$)	3900	1500	8500	80 000	4600
Effective density of states in valence band, N_V (cm^{-3})	6.0×10^{18}	1.04×10^{19}	7.0×10^{18}	7.3×10^{18}	1.1×10^{19}
Effective density of states in conduction band, N_C (cm^{-3})	1.04×10^{19}	2.8×10^{19}	4.7×10^{17}	4.2×10^{16}	5.7×10^{17}
Lattice constant, a (nm)	0.565	0.543	0.565	0.648	0.587
Dielectric constant, k	16.0	11.9	13.1	17.7	12.4
Melting point, T_m ($^{\circ}\text{C}$)	937	1412	1240	527	1060
Clarke number (%)	6.5×10^{-4}	25.8	Ga: 1×10^{-3} As: 5×10^{-4}	In: 1×10^{-5} Sb: 5×10^{-5}	In: 1×10^{-4} P: 8×10^{-2}

Until now in literature, the growth methods of Ge NWs are well established. They are reports using solution phase synthesis for GeNW growth.^{16,17,45-53} NWs synthesized in vapor phase, in most cases, are grown via VLS process. Chemical vapors, such as GeH_4 and GeI_2 are frequently employed as precursors due to the mild low temperature synthesis conditions.^{13,54-76} Ge vapors generated from high temperature (~ 1000 $^{\circ}\text{C}$) evaporation are also used for GeNW synthesis since this avoids the usage of toxic precursors and highly explosive carrier gas such as H_2 for safety consideration.⁷⁷⁻⁸⁵ Other methods such as laser ablation were also employed for GeNW synthesis.⁸⁶

As a typical example, the Ge NWs grown via Au-catalyzed VLS process is shown in Figure 2.14.⁷² Vertically aligned Ge NW arrays can now be easily obtained by epitaxial growth on lattice-matched substrates (such as Si and Ge substrates). Special attention should be paid to

remove the oxide layer between the Au catalyst and the underlying substrate in order to achieve good epitaxial relationship.

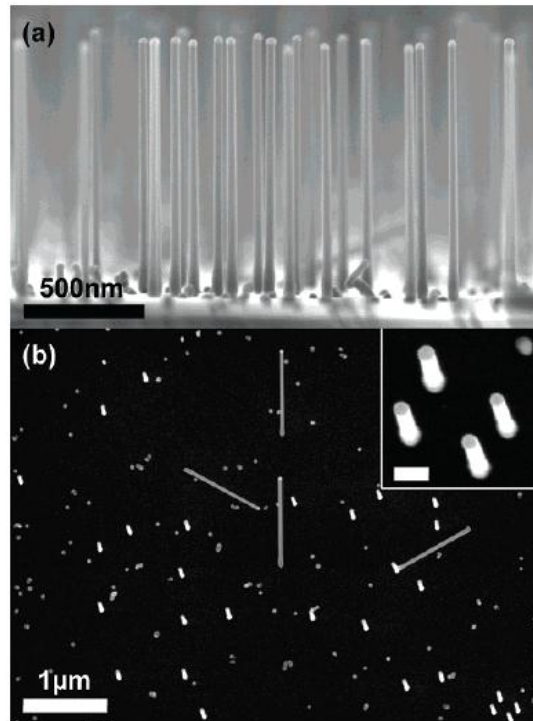


Figure 2. 14 (a) Cross-sectional and (b) top views of the Ge NWs epitaxially grown on Ge(111) substrates.⁷²

Au is the dominant metal used as catalysts for GeNW synthesis, due to the chemical stability and low eutectic temperature (see Figure 2.15).¹³ However, since Au possesses significant contamination problem to the carrier mobility of GeNWs.⁸⁷ It is critical to develop alternative metal catalyst that is suitable for GeNW growth. There are few reports using non-gold as metal catalysts for GeNW synthesis, including Mn,⁷¹ Bi,¹⁷ In and Sb,^{83,84} Fe,⁵⁹ and Ni.⁴⁸ Moreover, Tuan *et al.* reported a comprehensive investigation of the possibility to use several types of metals for GeNW growth, including Co, Ni, CuS, Mn, Ir, MnPt₃, Fe₂O₃, FePt, which all showed excellent capability to direct the GeNW growth in solution phase.⁵²

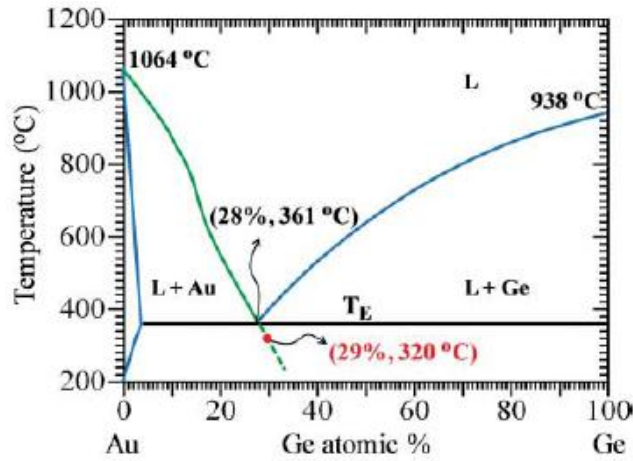


Figure 2. 15 Binary phase diagram of Au-Ge. The eutectic temperature of Au-Ge is 361 °C at 28 at.% of Ge.¹³

Ge NW based heterostructures have also been widely investigated to enable the potential functionalities of the NWs. For example, hierarchical Ge NW heterostructures, biaxial nanotapes, axial *p-n* NW junctions and radial core-shell NW heterostructures have all been demonstrated.

Branched heterostructures: Ge NW bundles⁸⁵

Chen *et al.* reported the growth of oriented Ge NWs with diameters below the Bohr radius on the faces of single-crystal Ge microcrystals.⁸⁵ Representative SEM images of the oriented GeNWs grown on Ge micro-crystals are shown in Figure 2.16. Ge powder was used as source powder. Si (110) substrates covered with 2-3 nm Au were used to collect the products. Ar and H₂ gas were introduced separately at flow rates of 50 and 5 sccm, respectively. The central temperature of the furnace was 925 °C with growth temperature around 700 °C. Bare Si or Si wafers coated with Ni produced no NWs. It is suggested that micro-crystals of Ge form first via the Stranski-Krastanov mechanism in the vicinity of the Au nanoparticles.⁸⁵ However, the reason why micro-crystals are form rather than domes requires further study. The reason of preferentially formation of Ge structures with different configurations and

shapes (micro-crystal and NW) was not given.⁸⁵ The capability to design various nanoscale heterostructures is central to investigate their potential unexpected properties and applications.

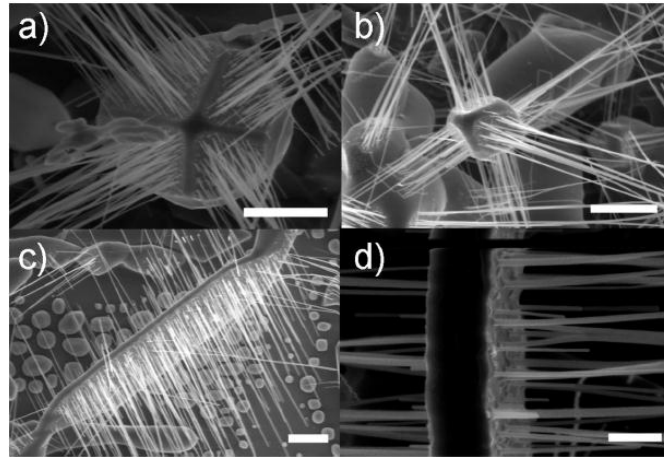


Figure 2. 16 Orientated growth of GeNWs on Ge micro-crystals.⁸⁵

Biaxial heterostructures: Ge-ZnO nanotapes⁸⁸

Yin *et al.* reported the fabrication of ZnO/Ge, ZnO/Ge/ZnO and Ge/ZnO/Ge nanotapes via a two stage chemical vapor deposition method.⁸⁸ Good epitaxial relationships were observed between the ZnO/Ge interfaces despite the large lattice mismatch. Typically, low magnification TEM images and HRTEM images of the biaxial heterostructures are shown in Figure 2.17. Both the ZnO and Ge parts are single crystalline.

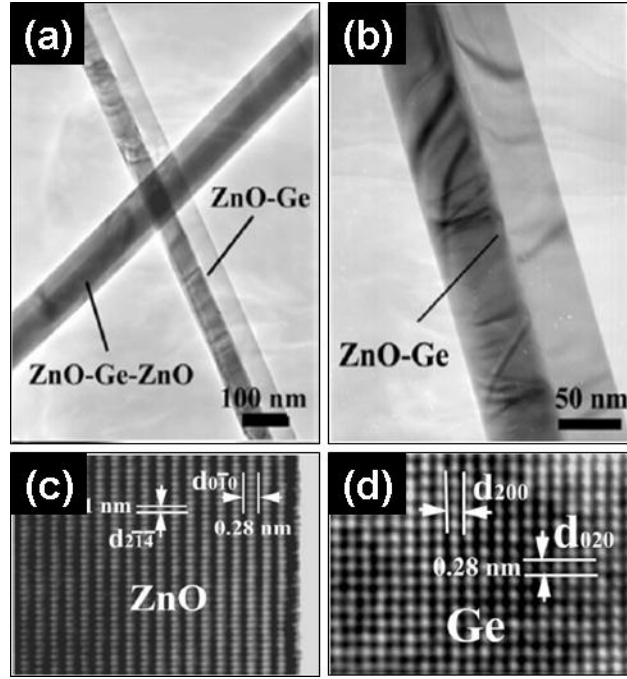


Figure 2. 17 (a,b) Low magnification TEM images of Ge-ZnO biaxial heterostructures; (c,d) HRTEM images of ZnO and Ge, respectively.⁸⁸

Axial heterostructures: linear GeNW p - n junction⁶⁶

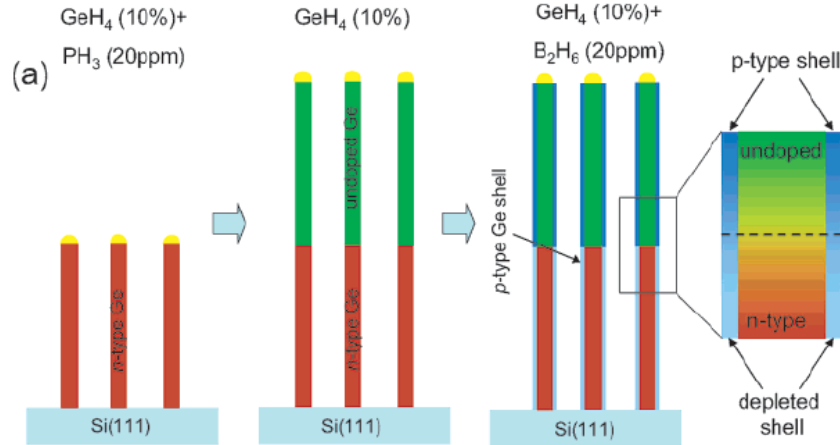


Figure 2. 18 Growth sequences of the Ge p - n junctions. Red color stands for n -type segment. Green light stands for undoped segment. Blue color stands for p -type segment.⁶⁶

Axial heterostructures of GeNWs have also been demonstrated. Tutuc *et al.* reported the growth linear GeNW p - n junctions by chemical vapor deposition and a peculiar dopant incorporation mechanism. Detailed growth sequences of the GeNW heterostructures is shown in Figure 2.18. First n -type GeNW arrays were epitaxially grown on Si (111) substrates using

GeH₄ as precursors and PH₃ as dopant. Then pure GeH₄ was introduced into the furnace for continuous growth of an intrinsic NW segment. Finally, a thin *p*-type shell using B₂H₆ as dopant gas was grown surrounding the whole NW. The *p*-type layer surrounding the undoped segment keeps its *p*-type nature, while the layer surrounding the *n*-type segment is depleted.

Radial heterostructures: epitaxial Ge/Si core/shell structures^{26,27,33,89-93}

Compared with the three GeNW heterostructures discussed above, radial GeNW heterostructures (core-shell structure) attracted much more interests due to their extraordinary electrical properties and excellent examples for fundamental study of the carrier (especially holes) properties. A brief introduction to the research progress for Ge/Si core/shell heterostructures will be presented in the following part.

Epitaxial core-shell and core multi-shell NW heterostructure synthesis was first realized in 2002 by Lieber's group.²⁶ A schematic illustration of the NW core, uniform shell and multiple shell growth is shown in Figure 2.19. First, the NW core is grown through gold-catalyzed growth. The synthesis conditions are controlled to maintain reactant decomposition only on the gold particle surface. Second, a thin uniform shell is deposited on the NW surface through altering the synthesis conditions to induce homogeneous reactant decomposition. Third, as a consequence, multiple shells can be readily grown by repeated modulation of the reactants.

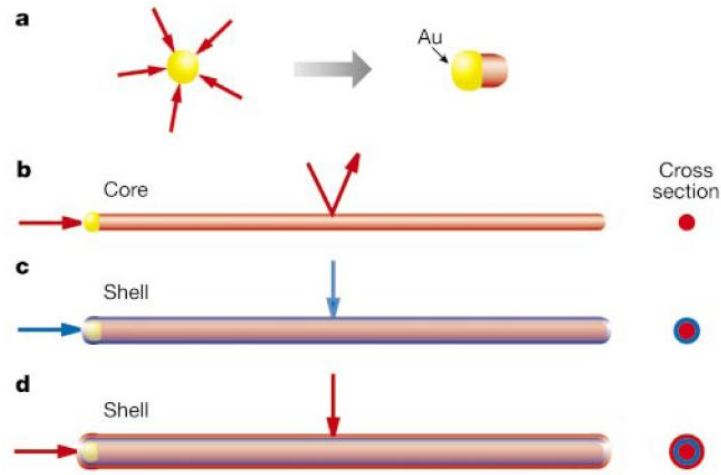


Figure 2. 19 Synthesis of core –shell NWs by sequential deposition methods.²⁶

Long carrier mean free paths at room temperature in Ge/Si core/shell NWs were observed previously,⁹³ similar to that of carbon nanotubes (CNTs).⁹⁴ However, the difficulty in controlling the electronic properties of CNTs have severely hindered their industrial applications. On the contrary, semiconductor NWs were also shown to exhibit uniform and consistent electronic properties. High performance FET using Ge/Si core/shell heterostructures with high- k dielectrics have been successfully demonstrated.²⁷

The 1D hole-gas in the Ge/Si NW heterostructures⁹³ give high-performance FETs values of the scaled transconductance ($3.3 \text{ mS } \mu\text{m}^{-1}$) and on current ($2.1 \text{ mA } \mu\text{m}^{-1}$) that are three to four times greater than state-of-the-art MOSFETs. Liang *et al.* reported the performance analysis of the Ge/Si core/shell NW FETs, using semi-classical, ballistic transport model and an tight binding treatment of the electronic structure.⁹¹ Comparison of the measured performance of the device with the simulated result assuming ballistic transport shows that the experimental device operates between 60-85% of the ballistic limit. In conclusion, Ge/Si core/shell NW heterostructures have been successfully fabricated and show great potential for the realization of high performance nanoelectronics.

2.2.2 Binary Ge-Based Nanostructures

There are generally two types of binary Ge-based NWs: germanium oxides and transition-metal germanides. The reports are much less than those on Ge NWs. We will introduce the research progress on GeO_2 and germanide NWs in the following section.

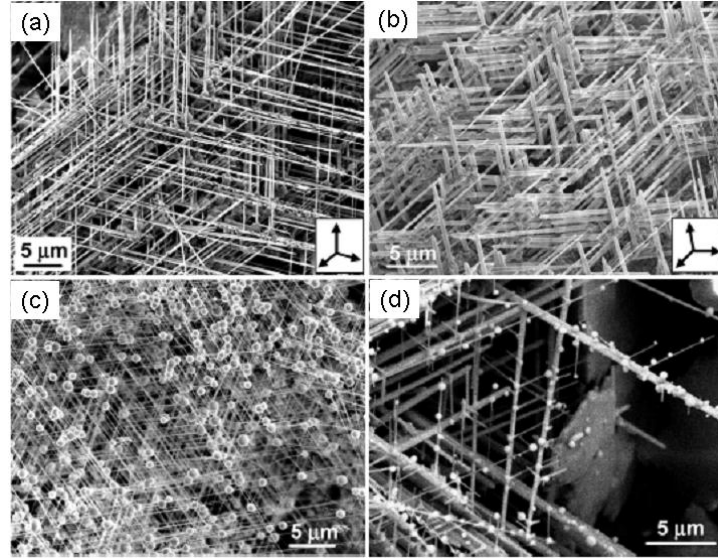


Figure 2.20 SEM images of the 3D GeO_2 NW networks.⁹⁶

During the actual synthesis of Ge NWs, it was noticed that the as-grown Ge NWs were usually coated with surface oxides. More efforts were devoted to the growth of pure GeO_2 NWs. Until now, several types of 1D GeO_2 nanostructures, including NWs⁹⁶ and nanotubes.⁹⁷ As a typical example, 3D GeO_2 NW networks grown via high temperature evaporation with the assistance of Al powder is shown in Figure 2.20.⁹⁶ The formation of order 3D nanostructures is due to the epitaxial growth. GeO_2 NWs are luminescent materials with a broad band emission peaked at ~ 400 nm.⁹⁶ They may find interesting applications in such as luminescent materials and waveguides.

Another type of binary Ge-based nanostructures is transition metal germanides. In bulk or thin film research, transition metal germanides are well investigated. Those germanides are considered as good electrical contacts in Si circuits due to their low resistivity and

compatibility with Si. Some other germanides are investigated for interesting magnetic properties. However, germanides in 1D form are rarely investigated. The research on silicide and germanide NWs was only initiated recently. While relatively abundant silicide NWs have been investigated, as can be found in a recent review paper,⁹⁸ research on germanides are very limited. Only very recently did Yoon *et al.* reported the synthesis of Co_5Ge_7 NWs and nanobelts.⁹⁹ The NWs were grown by evaporating CoCl_2 and Ge powders at high temperature. The NWs were shown to be excellent field emitters due to its high conductivity. To the best of our knowledge, this is the only report on germanide NWs that can be found in literature.

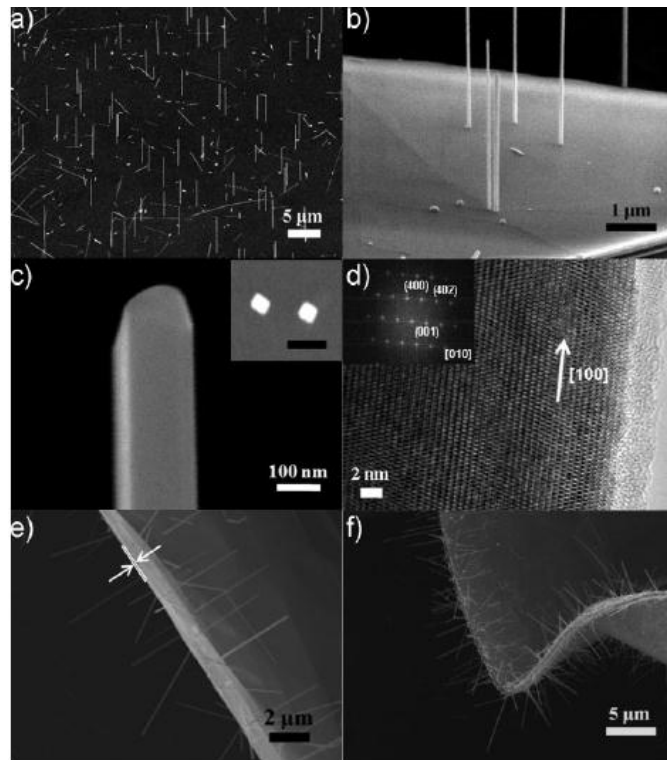


Figure 2. 21 SEM and TEM images of the Co_5Ge_7 NWs grown on flexible substrates.⁹⁹

One of the problems in silicide and germanide NW synthesis is the repeatability and phase control. Until now, direct reacting metal chlorides with Si or Ge source is a common method for silicide or germanide NW synthesis. However, one may find that the experimental methods provided in the reports can be rarely repeated. The NW growth is highly sensitive to many other factors besides from the usual growth parameters, such as growth temperature, pressure and carrier gas. Some other methods, such as single-source precursor for silicide

NW growth,⁹⁸ were also developed. However, the precursors are very expensive and the chemically derived single-source precursors are not stable in ambient conditions.

Phase control is another critical issue that needs to be investigated in silicide and germanide NW growth. For transition metal silicides and germanides, one characteristic is that there are many stoichiometric phase for each silicide or germanide material. Taken the Co-Ge system for example, there are 4 stable phases at room temperature: Co_5Ge_3 , CoGe , Co_5Ge_7 and $\text{Co}_{0.875}\text{Ge}_2$.¹⁰⁰ There are also several other meta-stable phases that may exist at high temperature. However, it is unknown why Co_5Ge_7 NWs were obtained, not CoGe NWs. Little is known regarding how to control and tune the phases of silicide and germanide NWs. This is an important and interesting point for future research.

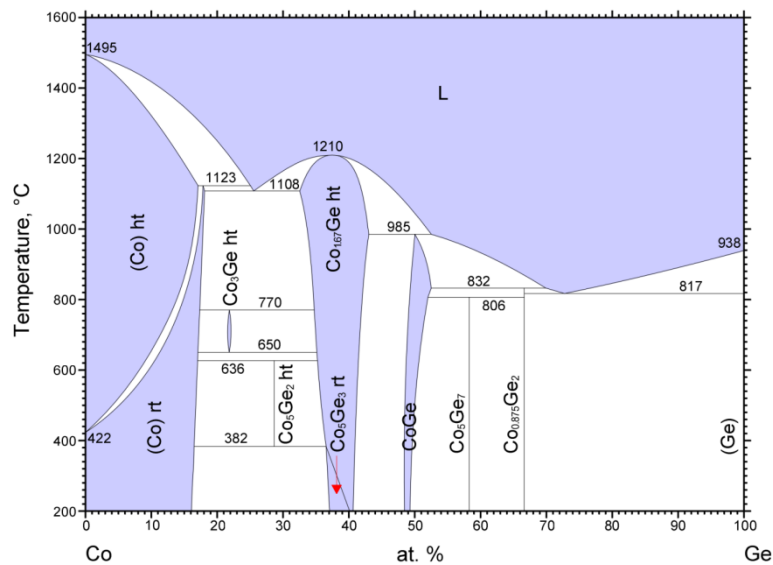


Figure 2. 22 Binary phase diagram of Co-Ge.¹⁰⁰

2.2.3 Ternary Ge-Based Nanostructures

By ternary germanates, we usually refer those ternary compounds containing Ge, O and another elements with formula $\text{M}_x\text{Ge}_y\text{O}_z$. Recently, there is increasing interest in those ternary oxide NWs, such as those ZnO-based ternary oxides.²³ While plenty of research has

been devoted to investigate elemental and binary NWs, there are still quite a lot remains to be explored in ternary compound NWs.

Ternary germanates, such as zinc germanate (ZGO) and indium germanate (IGO), are typically wide bandgap semiconductors. Also, the abundant structural defects in the materials make them good phosphors. Their luminescent materials can be efficiently tuned by proper doping. For example, ZGO doped with Mn is known to emit green light,¹⁰¹ while undoped ZGO is a native defect phosphor exhibiting white luminescence under UV excitation.¹⁰² Due to its interesting electronic and optical properties, ZGO has been widely used for many applications. For example, thin-film electroluminescent (TFEL) devices using ZGO as an active layer have been developed for potential display applications.¹⁰³ ZGO was also shown to be a stable photocatalyst for decomposition of water or organic pollutants.¹⁰⁴ However, 1D ternary ZGO nanostructures have rarely been investigated until now. Tsai *et al.* reported the growth of ZGO nanorods by aging Zn-containing Ge nanoparticles in water.¹⁰⁵ Huang *et al.* reported the synthesis of ZGO nanorods by a surfactant-assisted hydrothermal method.¹⁰⁶ Given the potential research interests that may arise with the unique ternary ZGO NWs, exploration of other synthesis methods that yield high quality NWs is critical for further studies. All previous methods were solution-involved and several drawbacks of the products, such as small aspect ratios, low yield, and severely agglomerated morphologies, may inhibit further studies of their properties and applications.^{105,106}

Further exploration of ternary germanate NW synthesis methods are crucial in order to investigate their properties and applications. Controllable syntheses of high quality (such as high purity, high aspect ratio, high yield and high crystallinity) are especially desired for further studies.

2.3 1D Nanostructures for Photodetector Applications

Photodetection is one of the most important applications of NW nanoelectronic devices. Usually, a 2-terminal or 3-terminal (transistor) semiconductor NW device is employed for photodetection application. The carrier densities and hence conductivities of the semiconductor NWs will change when illuminated with incident light with photon energy above the bandgap. The current level change will then be detected. Compared with 2-terminal (resistor) photodetectors, 3-terminal (transistor) devices allow more delicate control of the optoelectronic performances, by modifying the gate voltage. In literature, various 1D semiconducting nanostructures with different bandgaps have been used for photodetector applications. Herein we give several typical examples and discuss the literature progress and future directions.

2.3.1 Small Bandgap Semiconductor NWs

Ge, in its thin film and 1D form, has been widely investigated for photodetection applications due to its compatibility with Si. Ge photodetectors response to light with wavelengths up to 1800 nm due to its small bandgap (0.68 eV at room temperature). Visible light photodetectors using single GeNW has been demonstrated (Figure 2.24).¹⁰⁷ *p*-type GeNWs FETs were fabricated via electron beam lithography (EBL) followed by Ti electrode deposition. The FET and photoresponse behavior of the GeNW photodetector is shown in Figure 2.24.

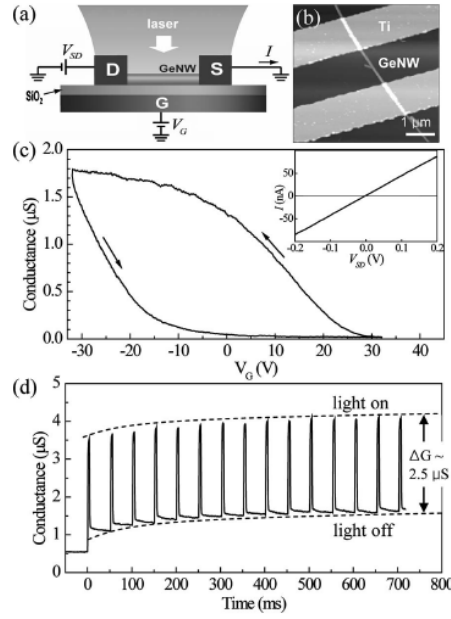


Figure 2.23(a) Schematic diagram and (b) AFM image of single GeNW photodetector. (c) Transfer characteristic of GeNW FET. (d) Photo-switching behavior of GeNW device under pulsed incident light (5 ms).¹⁰⁷

As expected for a typical *p*-type FET, conductance of the device increased with negative bias (Figure 2.23c). *I*-*V* characteristics showed a good Ohmic contact for the device (Figure 2.23c inset). Photoresponse behavior of the device when illuminated with visible light laser (532 nm, pulse duration 5 ms) is shown in Figure 2.23d. The current changed rapidly when the light was periodically turned on and off. The response time for the main photocurrent component is ~1 ms (system limit). However, it should be mentioned that a slow background photocurrent component was observed, displaying a long relaxation time (decay time) of 10 s.

2.3.2 Wide Bandgap Semiconductor NWs

Besides from the group IV NW photodetectors, another group of typical photodetectors are those using wide bandgap semiconductor NWs, such as ZnO, In₂O₃, *etc.* A typical ZnO NW photodetector is shown in Figure 2.24.¹⁰⁸

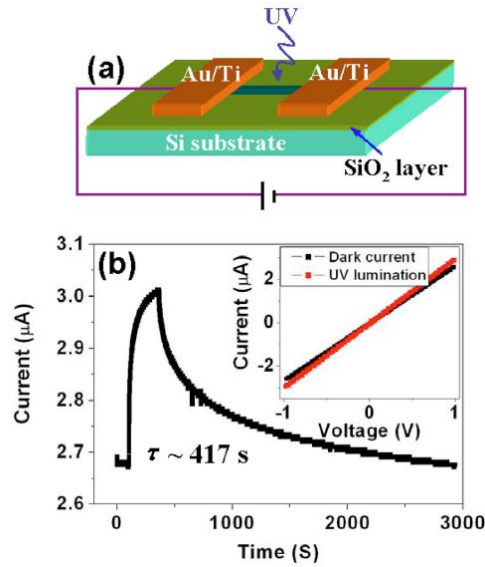


Figure 2. 24 (a) Schematic of a ZnO NW photodetector. (b) Photo-switching behavior showing slow response and reset time.¹⁰⁸

Figure 2.24a is a schematic diagram of the ZnO photodetector device, with its corresponding photoresponse curve in Figure 2.24b. For ZnO NWs with symmetric Ti/Au electrodes, good Ohmic behavior was observed (Figure 2.24b inset). The current increases upon 365 nm UV light illumination. However, slow response and reset time upto thousands of seconds were observed (Figure 2.24b).¹⁰⁸

This type of wide bandgap (usually binary oxide) NW photodetectors can be used for visible-blind photodetection. For example, the room temperature bandgaps for ZnO, In₂O₃ and SnO₂ are 3.3 eV (~376 nm), 3.6 eV (~344 nm) and 3.5 eV (~354 nm), respectively. Those types of photodetectors typically do not response to visible light with wavelengths above 400 nm.

2.3.3 Ternary Oxide Photodetectors with Even Larger Bandgap

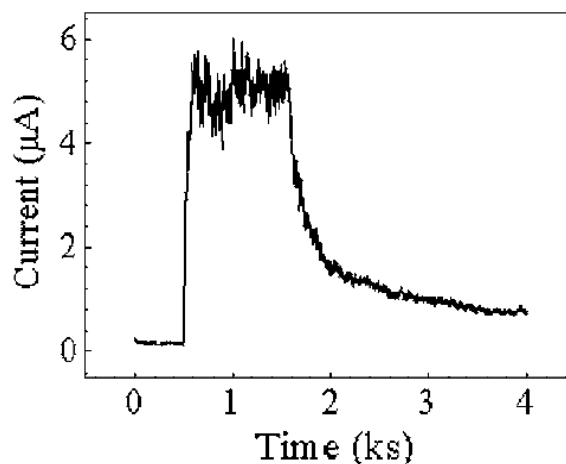


Figure 2. 25 Response and recovery characteristics of individual ZnSnO_3 NW as exposed to UV illumination at -3 V and 300 K.¹⁰⁹

Recently, photodetectors based on ternary oxide materials with even larger bandgaps are receiving increasing attention. For example, several ZnO-based ternary oxide NWs have been synthesized and used for photodetectors. Figure 2.25 shows the typical photoresponse behavior of individual ZnSnO_3 NW (bandgap ~ 3.7 eV) photodetectors.¹⁰⁹ Analogous to most of previous reports, slow recovery time >2500 s was observed.

References

- (1) Su, Y.; Li, S.; Xu, L.; Chen, Y. Q.; Zhou, Q. T.; Peng, B.; Yin, S.; Meng, X.; Liang, X. M.; Feng, Y. *Nanotechnology* **2006**, *17*, 6007-6010.
- (2) Han, X. H.; Wang, G. Z.; Jie, J. S.; Choy, W. C. H.; Luo, Y.; Yuk, T. I.; Hou, J. G. *Journal of Physical Chemistry B* **2005**, *109*, 2733-2738.
- (3) Wang, Z. L. *Advanced Materials* **2003**, *15*, 432-436.
- (4) Pan, Z. W.; Dai, Z. R.; Wang, Z. L. *Science* **2001**, *291*, 1947-1949.
- (5) Zhang, R. Q.; Lifshitz, Y.; Lee, S. T. *Advanced Materials* **2003**, *15*, 635-640.
- (6) Wang, N.; Tang, Y. H.; Zhang, Y. F.; Lee, C. S.; Lee, S. T. *Physical Review B* **1998**, *58*, 16024-16026.
- (7) Shi, W. S.; Zheng, Y. F.; Wang, N.; Lee, C. S.; Lee, S. T. *Applied Physics Letters* **2001**, *78*, 3304-3306.
- (8) Wanger, R. S.; Ellis, W. C. *Applied Physics Letters* **1964**, *4*, 89-90.
- (9) Li, Y.; Qian, F.; Xiang, J.; Lieber, C. M. *Materials Today* **2006**, *9*, 18-27.
- (10) Duan, X. F.; Lieber, C. M. *Advanced Materials* **2000**, *12*, 298-302.

- (11) Lu, W.; Lieber, C. M. *Journal of Physics D-Applied Physics* **2006**, *39*, R387-R406.
- (12) Persson, A. I.; Larsson, M. W.; Stenstrom, S.; Ohlsson, B. J.; Samuelson, L.; Wallenberg, L. R. *Nature Materials* **2004**, *3*, 677-681.
- (13) Kodambaka, S.; Tersoff, J.; Reuter, M. C.; Ross, F. M. *Science* **2007**, *316*, 729-732.
- (14) Schmidt, V.; Gosele, U. *Science* **2007**, *316*, 698-699.
- (15) Holmes, J. D.; Johnston, K. P.; Doty, R. C.; Korgel, B. A. *Science* **2000**, *287*, 1471-1473.
- (16) Hanrath, T.; Korgel, B. A. *Advanced Materials* **2003**, *15*, 437-440.
- (17) Lu, X. M.; Fanfair, D. D.; Johnston, K. P.; Korgel, B. A. *Journal of the American Chemical Society* **2005**, *127*, 15718-15719.
- (18) Greene, L. E.; Law, M.; Goldberger, J.; Kim, F.; Johnson, J. C.; Zhang, Y. F.; Saykally, R. J.; Yang, P. D. *Angewandte Chemie-International Edition* **2003**, *42*, 3031-3034.
- (19) Rao, C. N. R.; Deepak, F. L.; Gundiah, G.; Govindaraj, A. *Progress in Solid State Chemistry* **2003**, *31*, 5-147.
- (20) Fan, H. J.; Werner, P.; Zacharias, M. *Small* **2006**, *2*, 700-717.
- (21) Kuchibhatla, S.; Karakoti, A. S.; Bera, D.; Seal, S. *Progress in Materials Science* **2007**, *52*, 699-913.
- (22) Xia, Y. N.; Yang, P. D.; Sun, Y. G.; Wu, Y. Y.; Mayers, B.; Gates, B.; Yin, Y. D.; Kim, F.; Yan, Y. Q. *Advanced Materials* **2003**, *15*, 353-389.
- (23) Fan, H. J.; Yang, Y.; Zacharias, M. *Journal of Materials Chemistry* **2009**, *19*, 885-900.
- (24) Huang, Y.; Duan, X. F.; Cui, Y.; Lauhon, L. J.; Kim, K. H.; Lieber, C. M. *Science* **2001**, *294*, 1313-1317.
- (25) Gudiksen, M. S.; Lauhon, L. J.; Wang, J.; Smith, D. C.; Lieber, C. M. *Nature* **2002**, *415*, 617-620.
- (26) Lauhon, L. J.; Gudiksen, M. S.; Wang, C. L.; Lieber, C. M. *Nature* **2002**, *420*, 57-61.
- (27) Xiang, J.; Lu, W.; Hu, Y. J.; Wu, Y.; Yan, H.; Lieber, C. M. *Nature* **2006**, *441*, 489-493.
- (28) Yang, C.; Barrelet, C. J.; Capasso, F.; Lieber, C. M. *Nano Letters* **2006**, *6*, 2929-2934.
- (29) Jiang, X. C.; Xiong, Q. H.; Nam, S.; Qian, F.; Li, Y.; Lieber, C. M. *Nano Letters* **2007**, *7*, 3214-3218.
- (30) Lu, W.; Lieber, C. M. *Nature Materials* **2007**, *6*, 841-850.
- (31) Tian, B. Z.; Zheng, X. L.; Kempa, T. J.; Fang, Y.; Yu, N. F.; Yu, G. H.; Huang, J. L.; Lieber, C. M. *Nature* **2007**, *449*, 885-U8.
- (32) Dong, Y. J.; Yu, G. H.; McAlpine, M. C.; Lu, W.; Lieber, C. M. *Nano Letters* **2008**, *8*, 386-391.
- (33) Hu, Y. J.; Xiang, J.; Liang, G. C.; Yan, H.; Lieber, C. M. *Nano Letters* **2008**, *8*, 925-930.
- (34) Qian, F.; Li, Y.; Gradecak, S.; Park, H. G.; Dong, Y. J.; Ding, Y.; Wang, Z. L.; Lieber, C. M. *Nature Materials* **2008**, *7*, 701-706.
- (35) Huang, Y.; Duan, X. F.; Cui, Y.; Lieber, C. M. *Nano Letters* **2002**, *2*, 101-104.
- (36) Patolsky, F.; Zheng, G. F.; Hayden, O.; Lakadamyali, M.; Zhuang, X. W.; Lieber, C. M. *Proceedings of the National Academy of Sciences of the United States of America* **2004**, *101*, 14017-14022.
- (37) Higgins, J. M.; Ding, R. H.; DeGrave, J. P.; Jin, S. *Nano Letters* **2010**, *10*, 1605-1610.
- (38) Seo, K.; Yoon, H.; Ryu, S. W.; Lee, S.; Jo, Y.; Jung, M. H.; Kim, J.; Choi, Y. K.; Kim, B. *Acs Nano* **2010**, *4*, 2569-2576.
- (39) Lin, Y. C.; Chen, Y.; Shaios, A.; Huang, Y. *Nano Letters* **2010**, *10*, 2281-2287.
- (40) Huang, M. H.; Mao, S.; Feick, H.; Yan, H. Q.; Wu, Y. Y.; Kind, H.; Weber, E.; Russo, R.; Yang, P. D. *Science* **2001**, *292*, 1897-1899.
- (41) Yang, P. D.; Yan, R. X.; Fardy, M. *Nano Letters* **2010**, *10*, 1529-1536.
- (42) Chan, C. K.; Peng, H. L.; Liu, G.; McIlwrath, K.; Zhang, X. F.; Huggins, R. A.; Cui, Y. *Nature Nanotechnology* **2008**, *3*, 31-35.
- (43) Magasinski, A.; Dixon, P.; Hertzberg, B.; Kvit, A.; Ayala, J.; Yushin, G. *Nature Materials* **2010**, *9*, 353-358.

- (44) Kamata, Y. *Materials Today* **2008**, *11*, 30-38.
- (45) Coleman, N. R. B.; Ryan, K. M.; Spalding, T. R.; Holmes, J. D.; Morris, M. A. *Chemical Physics Letters* **2001**, *343*, 1-6.
- (46) Hanrath, T.; Korgel, B. A. *Journal of the American Chemical Society* **2002**, *124*, 1424-1429.
- (47) Hanrath, T.; Korgel, B. A. *Small* **2005**, *1*, 717-721.
- (48) Tuan, H. Y.; Lee, D. C.; Hanrath, T.; Korgel, B. A. *Chemistry of Materials* **2005**, *17*, 5705-5711.
- (49) Zaitseva, N.; Harper, J.; Gerion, D.; Saw, C. *Applied Physics Letters* **2005**, *86*.
- (50) Gerung, H.; Boyle, T. J.; Tribby, L. J.; Bunge, S. D.; Brinker, C. J.; Han, S. M. *Journal of the American Chemical Society* **2006**, *128*, 5244-5250.
- (51) Schricker, A. D.; Joshi, S. V.; Hanrath, T.; Banerjee, S. K.; Korgel, B. A. *Journal of Physical Chemistry B* **2006**, *110*, 6816-6823.
- (52) Tuan, H. Y.; Lee, D. C.; Korgel, B. A. *Angewandte Chemie-International Edition* **2006**, *45*, 5184-5187.
- (53) Ge, M.; Liu, J. F.; Wu, H.; Yao, C.; Zeng, Y.; Fu, Z. D.; Zhang, S. L.; Jiang, J. Z. *Journal of Physical Chemistry C* **2007**, *111*, 11157-11160.
- (54) Wu, Y. Y.; Yang, P. D. *Chemistry of Materials* **2000**, *12*, 605-+.
- (55) Wang, D. W.; Dai, H. J. *Angewandte Chemie-International Edition* **2002**, *41*, 4783-4786.
- (56) Wang, D. W.; Wang, Q.; Javey, A.; Tu, R.; Dai, H. J.; Kim, H.; McIntyre, P. C.; Krishnamohan, T.; Saraswat, K. C. *Applied Physics Letters* **2003**, *83*, 2432-2434.
- (57) Hanrath, T.; Korgel, B. A. *Journal of the American Chemical Society* **2004**, *126*, 15466-15472.
- (58) Kamins, T. I.; Li, X.; Williams, R. S. *Nano Letters* **2004**, *4*, 503-506.
- (59) Mathur, S.; Shen, H.; Sivakov, V.; Werner, U. *Chemistry of Materials* **2004**, *16*, 2449-2456.
- (60) Wang, D. W.; Chang, Y. L.; Wang, Q.; Cao, J.; Farmer, D. B.; Gordon, R. G.; Dai, H. J. *Journal of the American Chemical Society* **2004**, *126*, 11602-11611.
- (61) Adhikari, H.; McIntyre, P. C.; Sun, S. Y.; Pianetta, P.; Chidsey, C. E. D. *Applied Physics Letters* **2005**, *87*.
- (62) Wang, D. W.; Chang, Y. L.; Liu, Z.; Dai, H. J. *Journal of the American Chemical Society* **2005**, *127*, 11871-11875.
- (63) Wang, D. W.; Tu, R.; Zhang, L.; Dai, H. J. *Angewandte Chemie-International Edition* **2005**, *44*, 2925-2929.
- (64) Adhikari, H.; Marshall, A. F.; Chidsey, C. E. D.; McIntyre, P. C. *Nano Letters* **2006**, *6*, 318-323.
- (65) Jagannathan, H.; Deal, M.; Nishi, Y.; Woodruff, J.; Chidsey, C.; McIntyre, P. C. *Journal of Applied Physics* **2006**, *100*.
- (66) Tutuc, E.; Appenzeller, J.; Reuter, M. C.; Guha, S. *Nano Letters* **2006**, *6*, 2070-2074.
- (67) Tutuc, E.; Guha, S.; Chu, J. O. *Applied Physics Letters* **2006**, *88*.
- (68) Wang, D.; Dai, H. *Applied Physics a-Materials Science & Processing* **2006**, *85*, 217-225.
- (69) Zhang, L.; Tu, R.; Dai, H. J. *Nano Letters* **2006**, *6*, 2785-2789.
- (70) Adhikari, H.; McIntyre, P. C.; Marshall, A. F.; Chidsey, C. E. D. *Journal of Applied Physics* **2007**, *102*.
- (71) Lensch-Falk, J. L.; Hemesath, E. R.; Lopez, F. J.; Lauhon, L. J. *Journal of the American Chemical Society* **2007**, *129*, 10670-+.
- (72) Woodruff, J. H.; Ratchford, J. B.; Goldthorpe, I. A.; McIntyre, P. C.; Chidsey, C. E. D. *Nano Letters* **2007**, *7*, 1637-1642.
- (73) Chan, C. K.; Zhang, X. F.; Cui, Y. *Nano Letters* **2008**, *8*, 307-309.
- (74) Li, C. B.; Usami, K.; Muraki, T.; Mizuta, H.; Odal, S. *Applied Physics Letters* **2008**, *93*.
- (75) Sierra-Sastre, Y.; Choi, S.; Picraux, S. T.; Batt, C. A. *Journal of the American Chemical Society* **2008**, *130*, 10488-+.

- (76) Song, M. S.; Jung, J. H.; Kim, Y.; Wang, Y.; Zou, J.; Joyce, H. J.; Gao, Q.; Tan, H. H.; Jagadish, C. *Nanotechnology* **2008**, *19*.
- (77) Gu, G.; Burghard, M.; Kim, G. T.; Dusberg, G. S.; Chiu, P. W.; Krstic, V.; Roth, S.; Han, W. Q. *Journal of Applied Physics* **2001**, *90*, 5747-5751.
- (78) Wu, J.; Punchaipetch, P.; Wallace, R. M.; Coffey, J. L. *Advanced Materials* **2004**, *16*, 1444-+.
- (79) Huang, Y.; Lin, J.; Zhang, J.; Ding, X. X.; Qi, S. R.; Tang, C. C. *Nanotechnology* **2005**, *16*, 1369-1371.
- (80) Nguyen, P.; Ng, H. T.; Meyyappan, M. *Advanced Materials* **2005**, *17*, 549-+.
- (81) Pan, Z. W.; Dai, S.; Lowndes, D. H. *Solid State Communications* **2005**, *134*, 251-255.
- (82) Sun, X. H.; Didychuk, C.; Sham, T. K.; Wong, N. B. *Nanotechnology* **2006**, *17*, 2925-2930.
- (83) Yu, B.; Sun, X. H.; Calebotta, G. A.; Dholakia, G. R.; Meyyappan, M. *Journal of Cluster Science* **2006**, *17*, 579-597.
- (84) Sun, X. H.; Calebotta, G.; Yu, B.; Selvaduray, G.; Meyyappan, M. *Journal of Vacuum Science & Technology B* **2007**, *25*, 415-420.
- (85) Chen, X.; Kim, M. H.; Zhang, X.; Larson, C.; Yu, D.; Wodtke, A. M.; Moskovits, M. *Journal of Physical Chemistry C* **2008**, *112*, 13797-13800.
- (86) Zhang, Y. F.; Tang, Y. H.; Wang, N.; Lee, C. S.; Bello, I.; Lee, S. T. *Physical Review B* **2000**, *61*, 4518-4521.
- (87) Allen, J. E.; Hemesath, E. R.; Perea, D. E.; Lensch-Falk, J. L.; Li, Z. Y.; Yin, F.; Gass, M. H.; Wang, P.; Bleloch, A. L.; Palmer, R. E.; Lauhon, L. J. *Nature Nanotechnology* **2008**, *3*, 168-173.
- (88) Yin, L. W.; Li, M. S.; Bando, Y.; Golberg, D.; Yuan, X. L.; Sekiguchi, T. *Advanced Functional Materials* **2007**, *17*, 270-276.
- (89) Xiang, J.; Vidan, A.; Tinkham, M.; Westervelt, R. M.; Lieber, C. M. *Nature Nanotechnology* **2006**, *1*, 208-213.
- (90) Hu, Y. J.; Churchill, H. O. H.; Reilly, D. J.; Xiang, J.; Lieber, C. M.; Marcus, C. M. *Nature Nanotechnology* **2007**, *2*, 622-625.
- (91) Liang, G. C.; Xiang, J.; Kharche, N.; Klimeck, G.; Lieber, C. M.; Lundstrom, M. *Nano Letters* **2007**, *7*, 642-646.
- (92) Roddaro, S.; Fuhrer, A.; Brusheim, P.; Fasth, C.; Xu, H. Q.; Samuelson, L.; Xiang, J.; Lieber, C. M. *Physical Review Letters* **2008**, *101*.
- (93) Lu, W.; Xiang, J.; Timko, B. P.; Wu, Y.; Lieber, C. M. *Proceedings of the National Academy of Sciences of the United States of America* **2005**, *102*, 10046-10051.
- (94) Javey, A.; Guo, J.; Paulsson, M.; Wang, Q.; Mann, D.; Lundstrom, M.; Dai, H. J. *Physical Review Letters* **2004**, *92*.
- (95) Javey, A.; Guo, J.; Wang, Q.; Lundstrom, M.; Dai, H. J. *Nature* **2003**, *424*, 654-657.
- (96) Gu, Z. J.; Liu, F.; Howe, J. Y.; Paranthaman, M. P.; Pan, Z. W. *Crystal Growth & Design* **2009**, *9*, 35-39.
- (97) Jiang, Z.; Xie, T.; Wang, G. Z.; Yuan, X. Y.; Ye, C. H.; Cai, W. P.; Meng, G. W.; Li, G. H.; Zhang, L. D. *Materials Letters* **2005**, *59*, 416-419.
- (98) Schmitt, A. L.; Higgins, J. M.; Szczech, J. R.; Jin, S. *Journal of Materials Chemistry* **2010**, *20*, 223-235.
- (99) Yoon, H.; Seo, K.; Bagkar, N.; In, J.; Park, J.; Kim, J.; Kim, B. *Advanced Materials* **2009**, *21*, 4979-+.
- (100)
- (101) Lewis, J. S.; Holloway, P. H. *Journal of the Electrochemical Society* **2000**, *147*, 3148-3150.
- (102) Liu, Z. S.; Jing, X. P.; Wang, L. X. *Journal of the Electrochemical Society* **2007**, *154*, H500-H506.
- (103) Bender, J. P.; Wager, J. F.; Kissick, J.; Clark, B. L.; Keszler, D. A. *Journal of Luminescence* **2002**, *99*, 311-324.
- (104) Sato, J.; Kobayashi, H.; Ikarashi, K.; Saito, N.; Nishiyama, H.; Inoue, Y. *Journal of Physical Chemistry B* **2004**, *108*, 4369-4375.

- (105) Tsai, M. Y.; Yu, C. Y.; Wang, C. C.; Perng, T. P. *Crystal Growth & Design* **2008**, 8, 2264-2269.
- (106) Huang, J. H.; Ding, K. N.; Hou, Y. D.; Wang, X. C.; Fu, X. Z. *Chemsuschem* **2008**, 1, 1011-1019.
- (107) Ahn, Y. H.; Park, J. *Applied Physics Letters* **2007**, 91.
- (108) Zhou, J.; Gu, Y. D.; Hu, Y. F.; Mai, W. J.; Yeh, P. H.; Bao, G.; Sood, A. K.; Polla, D. L.; Wang, Z. L. *Applied Physics Letters* **2009**, 94.
- (109) Xue, X. Y.; Chen, Y. J.; Li, Q. H.; Wang, C.; Wang, Y. G.; Wang, T. H. *Applied Physics Letters* **2006**, 88.

CHAPTER 3 Experimental Methods

3.1 NW Growth Processes

3.1.1 Furnace Setup

The growth chamber used in this study is a high-temperature horizontal quartz-tube furnace (Advance Pinnacle Technologies Pte Ltd, ELITE furnace), equipped with gas gauge and vacuum pump. A schematic diagram of the furnace setup for NW growth is shown in Figure 3.1.¹

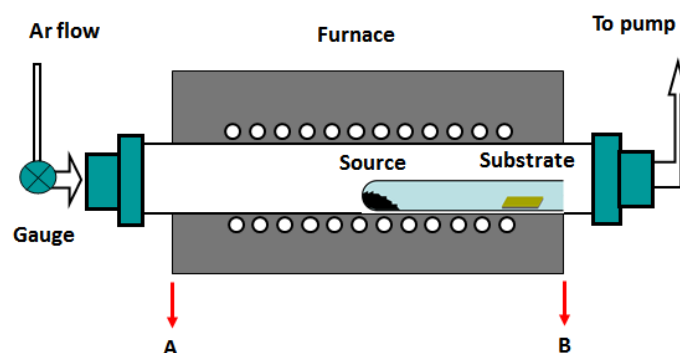


Figure 3. 1 Furnace setup used for NW growth.¹

The furnace length is ~1 m (from point A to B in Figure 3.1) and the large quartz tube length is ~1.5 m. The out diameter (OD) and inner diameter (ID) of the large quartz tube are 25 mm and 20 mm, respectively. Maximum temperature of the furnace setup is 1200 °C. During NW growth, a small quartz tube (OD 15 mm, ID 13 mm, length 300 mm) with one end sealed is usually used to contain the source materials and growth substrates (Figure 3.1). This small quartz tube is of great importance to enhance the vapor concentration in the growth chamber, which will be discussed in detail in later chapters. Source materials are placed at the sealed end of the small quartz tube near the center (upstream) of the furnace. Growth substrates were placed at the open end (downstream) of the chamber to collect growth products. Gas flows (such as Ar, O₂, *etc.*) are introduced from the upstream end with flow rate controlled by a

digital gauge (0-500 sccm). A vacuum pump is connected to the downstream end of the large quartz tube to achieve a low pressure conditions for NW growth.

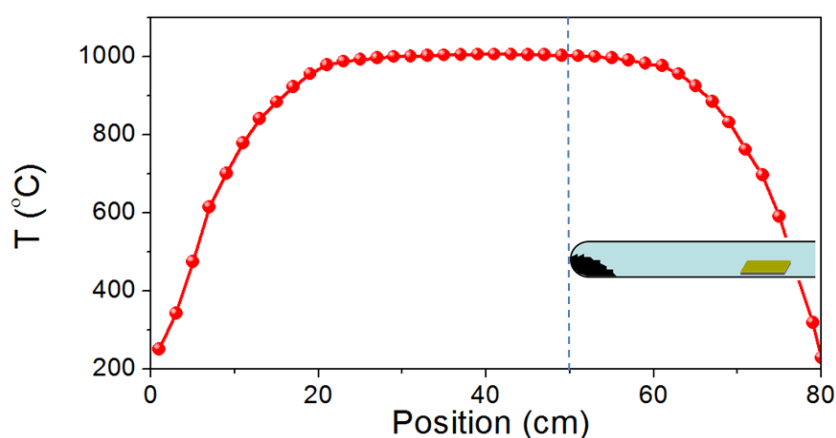


Figure 3. 2 Temperature profile of the furnace with a central temperature of 1000 °C. Location of the small quartz tube at the downstream end is indicated. Locations of the growth substrates vary in different growth round to the test the growth temperature effect.

Temperature profile of the furnace chamber with a highest central temperature of 1000 °C is shown in Figure 3.3. Uniform temperature can be kept at the central segment (~40 cm). The temperature decreases from 1000 °C to ~250 °C at the ending downstream segment (~20 cm). This temperature gradient is used for NW growth in our studies. Location of the small quartz tube is indicated in Figure 3.3. The source materials are located at the highest temperature of 1000 °C and the growth substrates were located at the low temperature region. Positions of the growth substrates vary in different growth rounds (*e.g.* 300-700 °C) to test the effect of growth temperature and to achieve optimum morphology.

3.1.2 Growth Substrate Preparation

Si(100) substrates are used in this study as growth substrates to collect the products. The substrates are usually cut into small pieces (8 mm × 10 mm) to fit the size of the small quartz tube. Those small Si pieces are usually sonicated in deionized (DI) water for 5 min followed by 5 min sonication in ethanol before dried using N₂ flow.

Au catalysts are coated on the Si substrates when necessary. The Au film is coated using a sputter coater equipped with Au target. Ar plasma generated by the applied electric field would be attracted to the Au target and the bombarded Au atoms would deposit on the Si substrates located below the target. The film coating rate is $\sim 0.3 \text{ nm s}^{-1}$ at a current level of 18 mA. Usually a film of 6-9 nm is used in our experiments, corresponding to a coating time of 20-30 s. No further treatments such as thermal annealing are needed before usage.

3.1.3 Source Material Preparation

Solid phase source materials are used in our studies. Powders with desired compositions and molar/weight ratios are mechanically ball milled to obtain a uniformly mixed source powder. For the growth of different types of nanostructures, such as GeNW, ZGO NW or IGO NW with different morphologies, the source materials (compositions and molar/weight ratios) would be changed correspondingly to obtain the desired structures. A proper amount of mixed source powders are placed at the sealed end of the small quartz tube, which are then evaporated at the high temperature furnace region to provide vapor source for NW growth. Details of the source materials used for the growth of each type of nanostructure will be provided later in each chapter.

3.1.4 NW Growth Conditions

The prepared growth substrates and source materials are loaded into the small quartz tube, which is then inserted into the large quartz tube at specific locations. The large quartz tube is first carefully sealed and pumped without gas flow to remove air. A base pressure on the order of 10^{-3} mbar is achievable in our furnace system. A thorough checking of the system vacuum conditions is required before initiating the NW growth process.

The heating and cooling processes are controlled by the program embedded in the furnace system. For example, the furnace can be heated up to 1000 °C at a ramping rate of 10 °C/min and held at 1000 °C for 60 min before cooling down to room temperature naturally. Pressure inside the reaction chamber can be tuned by the gas flow. The measured pressure as a function of Ar flow rate is shown in Figure 3.3. The pressure was measured at room temperature with the pump fully opened and is almost linear with the flow rate reaching a maximum of 3.5 mbar at 500 sccm (system limit).

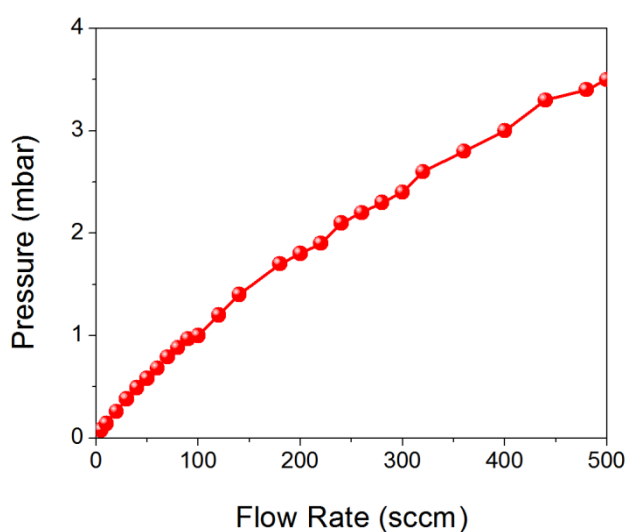


Figure 3. 3 Pressure as function of Ar gas flow rate at room temperature.

Growth temperature is controlled by changing the position of the growth substrate and the temperature can be determined according to the temperature profile (Figure 3.2). A series of substrates are usually placed across a wide temperature region (*e.g.*, 300-900 °C) to test the optimum growth conditions, although later substrates are only placed at the optimum temperature region to obtain good products.

The final products obtained are combinational results of various growth parameters, including growth temperature, pressure, gas ambient (Ar or O₂), source materials, catalyst, growth

period, *etc.* The specific growth conditions will also be presented in each chapter in correspondence to the specific nanostructures.

3.2 Characterizations

In general we used 4 types of instruments to characterize the nanostructures in this study: X-ray diffraction (XRD), scanning electron microscopy (SEM), transmission electron microscopy (TEM) and energy dispersive spectroscopy (EDS).

3.2.1 XRD

XRD was used to characterize the crystal structure of the products. Two types of XRD instruments were used in this study (Rigaku and Shimazu Standard, voltage 40 kV, current 40 mA), both for thin film characterizations with $\text{CuK}\alpha$ radiation ($\lambda = 1.5418 \text{ \AA}$). The products were mounted on the Si substrates (as-grown samples or with post-growth treatments) for XRD characterization. The usage of thin film XRD instruments help to avoid diffraction signals from the underlying substrates and ease further analyses. Typically, the scanning was performed in the range of $10\text{-}80^\circ$ with a fixed X-ray incident angle of 0.5° , a scanning rate of $1^\circ/\text{min}$ and a scanning step of 0.02° . Indexing of the as-obtained diffraction data can be performed using software like “Match” with ICDD database (International Centre for Diffraction Data). A typical digital photograph of the Rigaku XRD system is shown in Figure 3.4.



Figure 3. 4 Digital photograph of the Rigaku XRD system.

3.2.2 SEM

SEM was used to characterize the morphology and structures of the nanomaterials or nanodevices. Several types of SEM instruments were used in this study, including thermal emission SEM (JEOL 6360) and field emission SEM (JEOL 6340F, JEOL 7600F). Field emission SEM (operating at 5 kV) gives better resolution compared with thermal emission SEM (operating at 15 kV). For the morphological characterizations of the as-grown products, no further treatments like Au coating (to enhance the conductivity and avoid charging effect) are needed since the products grown on Si substrates possess good conductivity. A typical digital photograph of the JEOL 6340F SEM system is shown in Figure 3.5.



Figure 3. 5 Digital photograph of the SEM system (JEOL 6340F).

3.2.3 TEM

TEM (JEOL 2010 and JEOL 2100F, operating at 200 kV) was used to characterize the detailed morphology and crystal structure of the nanostructures. The as-grown samples were ultra-sonicated in ethanol for typically 30 s to disperse the NWs in solution. Then several drops of NW solutions were dropped onto a Cu grid coated with lacey carbon film. The TEM samples were dried in air before analysis.



Figure 3. 6 Digital photograph of the TEM system (JEOL 2100F).

3.2.4 EDS

EDS attached in the TEM system was used to characterize the chemical compositions of the nanostructures with a high resolution. Compared with the EDS in SEM system, EDS in TEM can provide more accurate compositional analysis, even on an individual NW. EDS spectrum can be collected in the JEOL 2100F system with characteristic peaks which can be used to identify the chemical elements. EDS mapping profile can also be collected using the scanning TEM (STEM), providing a direct view of the elemental distribution in the nanostructures.

3.3 Device Fabrications and Property Measurements

3.3.1 Device Fabrications

In our studies, the NW devices were fabricated by photolithography. Schematic diagrams of the lithography steps are shown in Figure 3.7.² Note that the NWs were dispersed on the substrates either before or after the photolithography and electrode deposition processes. Photoresist (PMMA) is spin coated on the SiO₂/Si substrates resulting in a uniform film coating (~1 μm). Then the photoresist film is baked (180 °C, 15 min) and exposed to UV light source with patterns generated through the photomask (step 2). The exposed substrates are developed using wet chemical etching (MIBK/IPA) to remove the exposed areas (step 3). Metal film with desired thickness is then deposited on the substrates via sputtering (step 4). Finally the electrode patterns can be obtained by simply removing the PMMA with wet chemicals like acetone.

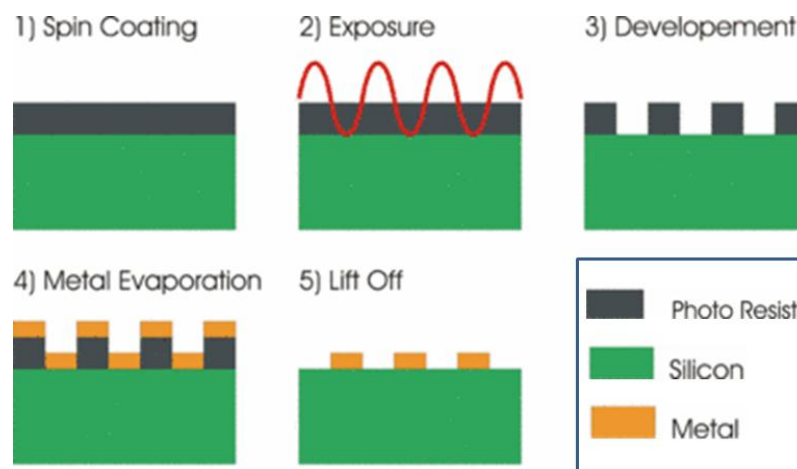


Figure 3. 7 Schematic diagrams of the photolithography processes.²

We have also used focused-ion-beam (FIB, FEI Novaetch Nanolab DualBeam 600i) to deposit Pt contacts on NWs in this study. A typical photograph of the FIB system is shown in Figure 3.8. A maximum ion beam resolution of 7 nm is achievable in this system at 30 kV voltage. A representative SEM image of NW device with FIB-deposited Pt contacts is shown

in Figure 3.9. The Pt contacts are of crucial importance in this case to measure the electrical and optoelectronic properties of the NW device.



Figure 3. 8 Digital photograph of the FIB system (FEI Novaetch Nanolab DualBeam 600i).

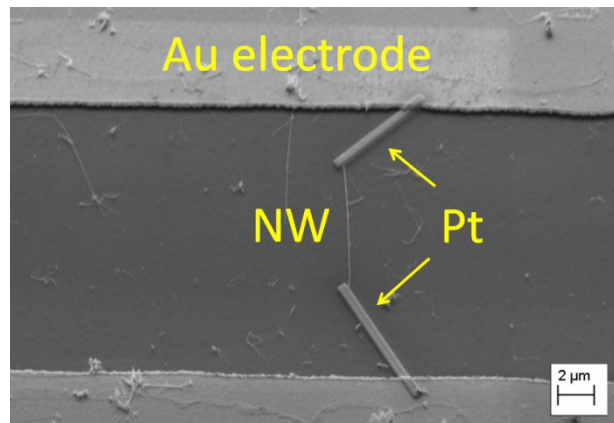


Figure 3. 9 SEM image of a typical NW device with FIB-deposited Pt contacts.

3.3.2 Property Measurements

Electrical properties of the NW devices were measured in Keithley semiconductor parameter analyser (Figure 3.10). Optical microscope in the system is equipped with tungsten-halogen lamp. Intensity of this white light source can be tuned in the range of $0-0.8 \text{ mW cm}^{-2}$ at a magnification of 50 (objective lens) and was used as the incident light for the photodetector measurement of Ge NW devices. Portable UV lamp (254 and 365 nm) was added in the

Keithley system for the performance measurements of photodetectors using wide bandgap semiconductor NWs.

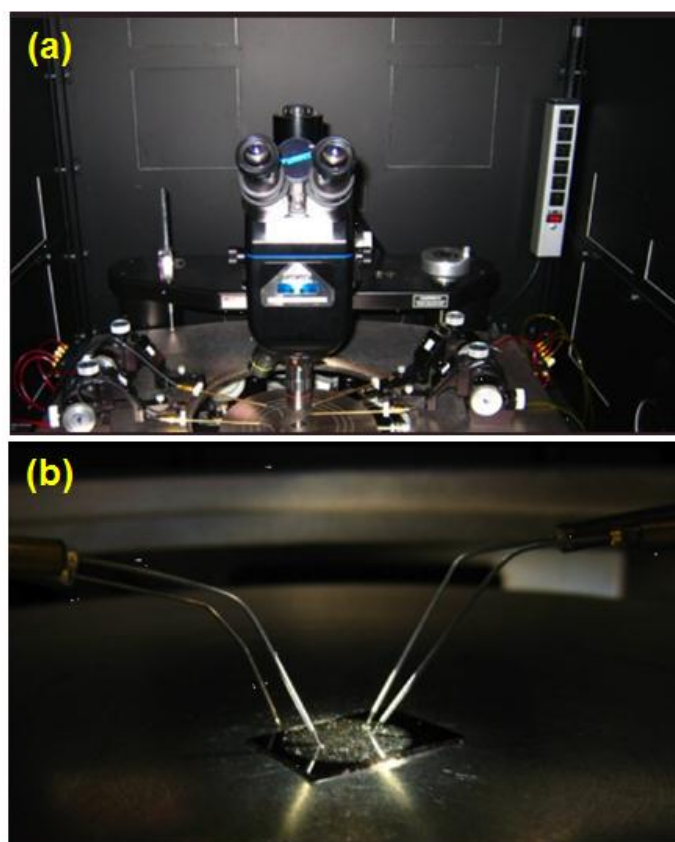


Figure 3. 10 Photograph of the Keithley system: (a) overview and (b) probe tips.

References:

- (1) Yan, C. Y.; Lee, P. S. *Journal of Physical Chemistry C* **2009**, *113*, 14135-14139.
- (2) <http://www.mpi-halle.mpg.de/departement2/research-areas/nanowires-nanoobjects/nanowires-by-metal-assisted-etching/abstract/nanowires-by-laser-interference-lithography-and-metal-assisted-etching/>.

CHAPTER 4 Elemental GeNWs: Catalytic Growth and Applications in Visible Light Photodetectors

4.1 Objective

Majority of the research in GeNW synthesis is based on the VLS mechanism.¹ During the NW growth, a metal catalyst particle forms eutectic liquid alloy with Ge at the growth temperature. The liquid droplet readily supersaturates and precipitation of solid Ge leads to axial NW growth. Until now, Au is the dominant catalyst used for semiconductor NW synthesis, due to its chemical inertness, thermal stability and the ability to form eutectic at low temperature. In this chapter, we will first present the synthesis and characterizations of GeNWs via Au-catalyzed VLS method. High quality GeNWs were grown by CVD method in a horizontal quartz tube furnace. Detailed characterizations confirmed the morphology, crystal structure and chemical compositions of the NWs. The effects of growth temperature and pressure were also investigated.

Despite serving as excellent universal catalysts for NW growth, Au has been found to diffuse into the semiconductor NWs during growth.² The contamination of Au is a long-standing concern because it is highly detrimental to the carrier mobility in future electronic devices.²⁻⁴ Thus, it is critical to develop suitable alternative metal catalysts to advance NW-based device technologies. Efforts have been dedicated to seek non-Au catalysts for semiconductor NW seeding. Alternative metal catalysts for oxide NW seeding have been reported, such as Sn for zinc oxide NWs and various metals of different groups for tin oxide.^{5,6} Also, non-Au metal catalysts for Si and GeNW seeding have been reported, such as Al,⁷ Mn,⁸ In,⁹ and several metal compounds.¹⁰ Especially, Bi was employed to catalyze the growth of group III-V

semiconductors,¹¹ zinc chalcogenides,¹² and GeNWs¹³ in solution phase. In this chapter, we will investigate the vapor phase GeNW growth using Bi catalysts. The successful synthesis of Si or GeNWs using electronically friendly Bi catalysts is of great importance for future device applications.

GeNWs have been considered as promising building blocks in potential high-speed nanoelectronic devices, due to its high carrier mobility and compatibility with Si. Numerous reports can be found on the studies of GeNW electronic devices.^{14,15} However, few reports can be found on the optoelectronic property studies (such as photodetectors). Ahn *et al.* reported the fabrication of single GeNW transistor for the detection of visible light.¹⁶ Polycrystalline GeNW arrays embedded in AAO templates were also used as photoresistors.¹⁷ Much work still remains to be done for the exploration of GeNWs in optoelectronic devices. For example, the fabrication of single NW transistor is rather expensive, complex and time consuming, due to the usage of electron beam lithography (EBL) for device fabrication.¹⁶ Also, the GeNW photodetectors showed slow response and reset time, limiting their applications in future high-speed devices.^{16,17} In this chapter, we will also present our work on the employment of GeNW networks as efficient detection channels in visible light photodetectors. The network devices only require facile and cost-effective fabrication processes and exhibit superior performances (fast photoresponse time) compared to single-NW devices. Our studies showed that network devices are promising alternative solutions to single NW devices for large scale industrial applications.

4.2 Au-Catalyzed Growth of GeNWs

4.2.1 Au-Ge Binary Phase Diagram

For those NWs synthesized via VLS mechanism, binary phase diagram can be used to predict possible growth conditions and catalysts.¹⁸ Au-Ge binary phase diagram¹⁹ is shown in Figure 4.1. The eutectic temperature of Au-Ge is 361 °C at a Ge atomic concentration of 28%. The NWs actually can grow at a temperature much lower than 361 °C via VLS process due to the supersaturation effect,²⁰ which leads to significant lowering of the alloy melting point. High quality GeNWs have been reported to grow at a temperature as low as 275 °C through chemical vapor deposition (CVD) method.^{21,22} The low temperature growth is specially desired for possible integration of the NWs with semiconductor technology.

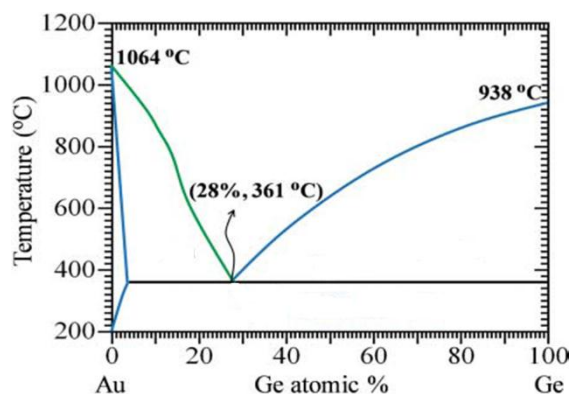


Figure 4. 1 Au-Ge binary phase diagram.²⁰

4.2.2 Experimental Methods

Schematic diagram of the furnace setup for GeNW growth is shown in Figure 4.2. Mixed Ge and carbon powder (~0.5 g, weight ratio 1:1) was placed at the sealed end of a small quartz tube. Cleaned Si (100) substrates pre-coated with 9 nm Au film were placed at the open end of the small quartz tube for product collection. Then the small quartz tube was loaded into the furnace chamber, with sealed end at the central high temperature region. Temperature of the furnace was increased to 1000 °C at a rate of 15 °C min⁻¹ and kept for 60 min under a

constant Ar flow of 200 sccm. The temperature of the Si substrates during growth was in the range of 300-500 °C. The furnace was allowed to cool naturally to room temperature after growth.

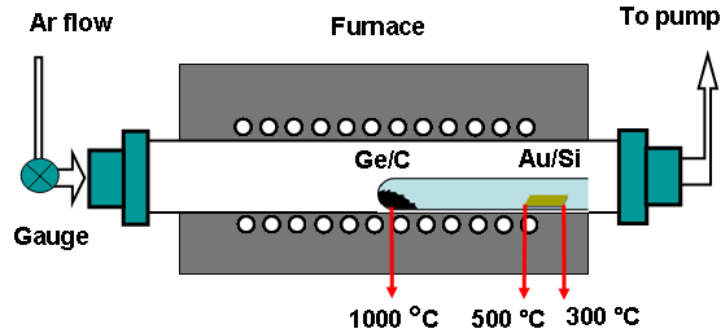


Figure 4. 2 Experimental setup used for GeNW growth using Au catalyst.

4.2.3 Morphological and Structural Characterizations

When the furnace was cooled down to room temperature, a brown fluffy layer is visually observable on the Si substrate. The products were first characterized using SEM. Typical low and high magnification SEM images of the NWs are shown in Figure 4.3.

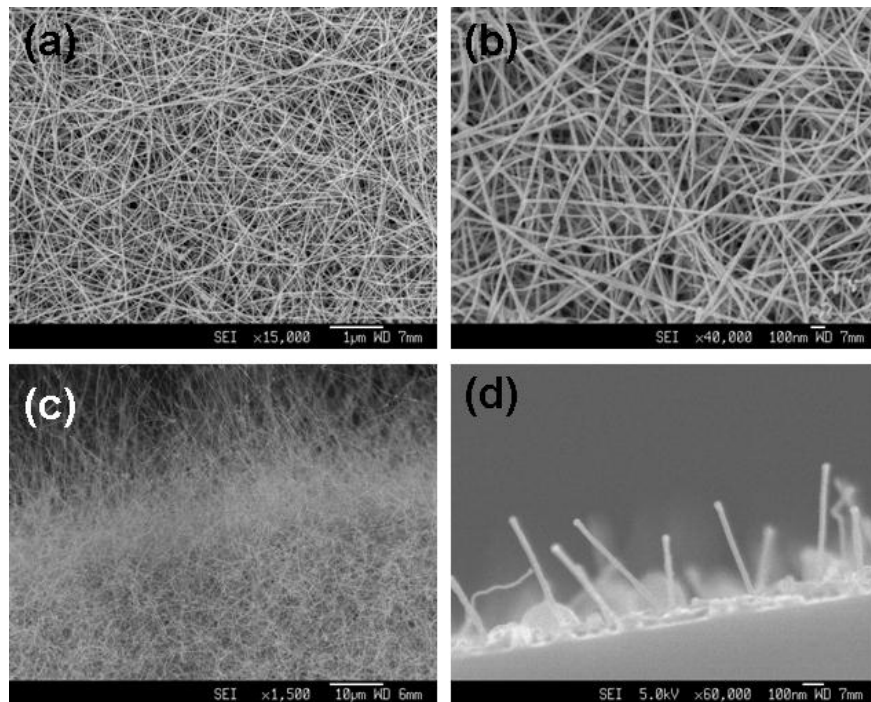


Figure 4. 3 SEM images of GeNWs synthesized using Au as catalysts: (a) low magnification; (b) high magnification; (c) NWs grow out of the edge of the substrate; (d) cross-sectional view of the short Ge nanorods.

Large quantities of NWs can be observed on the substrates. Diameters of the GeNWs are in the range of 10-100 nm, with lengths determined by the growth time. In Figure 4.3a, the lengths are up to tens of micrometers, while in Figure 4.3d, the lengths are well below 1 μm . Diameter of the NWs can be controlled by the size of the Au catalyst particles, since the diameter of the Au catalyst particle is essentially the same as that of the NW.²³ Figure 4.4 shows the NW diameter distribution of two samples grown with different Au coating thickness. The two samples were coated with Au of 6 nm and 9 nm, respectively. We expect that for a thicker coating, the size of the nanoparticles after annealing would be correspondingly larger, leading to larger NW diameter. Gaussian fit of the distribution is shown in Figure 4.4 (solid lines). The average diameters for 6 nm and 9 nm coatings are 27 nm and 43 nm, respectively.

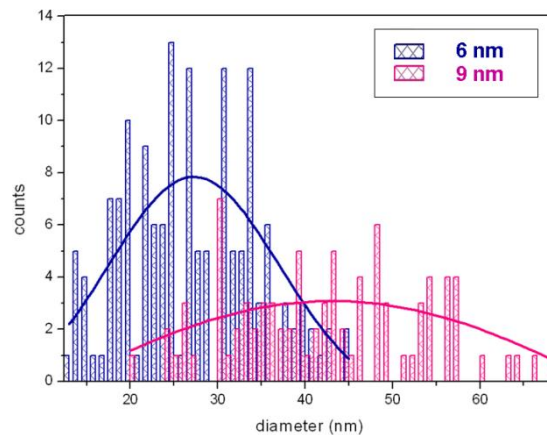


Figure 4. 4 Diameter distribution of the samples coated with different Au thickness. Solid lines are corresponding Gaussian fit.

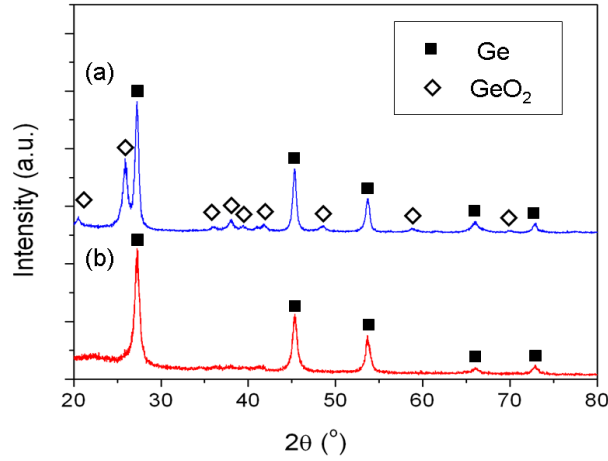


Figure 4. 5 XRD patterns show the crystal phase of the as-synthesized GeNWs: (a) both GeO_2 and Ge phases detected. (b) Pure Ge phase synthesized with a better vacuum condition.

The crystal phase of the as-synthesized GeNWs is analyzed using XRD. Typical XRD patterns are shown in Figure 4.5. The patterns are collected from NWs of different batches. The vacuum conditions in the quartz tube furnace vary with the seal conditions when reloading the samples. For those NWs synthesized with a high background pressure (i.e. more residual air in the chamber), XRD pattern shows the formation of both GeO_2 and Ge phase (Figure 4.5a). GeO_2 phase possesses a hexagonal crystal structure (JCPDS 36-1463: $a=4.985$ Å, $c=5.648$ Å), and Ge phase possesses a typical diamond cubic phase (JCPDS 4-0545: $a=5.6576$ Å). When the furnace was carefully sealed and pumped down to a basement pressure around 5×10^{-2} mbar before growth, typically the NWs are composed of pure Ge phase (Figure 4.5b).

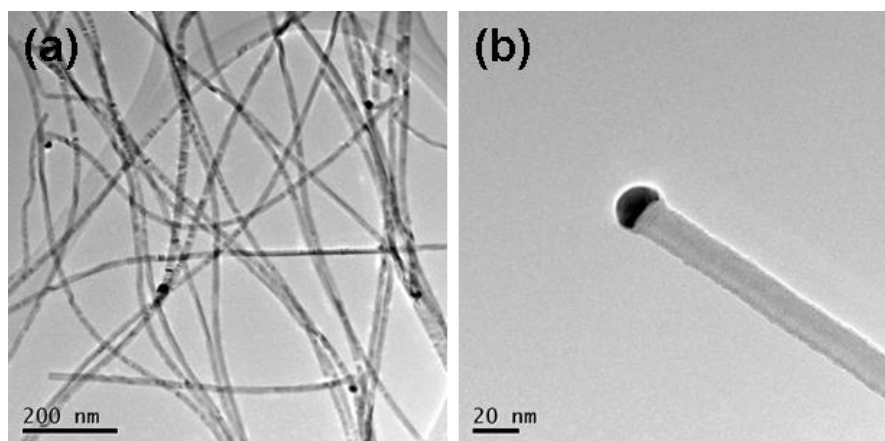


Figure 4. 6 (a) Low magnification TEM image of the GeNWs with uniform diameter through the length; (b) high magnification TEM image of a single GeNW, showing the Au catalyst particle at the front (dark spot).

Detailed crystal structures of the NWs are analyzed using TEM. As-synthesized GeNWs are dispersed in ethanol by ultra-sonication. Then solution containing the NWs is dispersed on Cu grid coated with holey carbon film. With a proper NW concentration in ethanol, several drops of the solution can lead to deposition of abundant NWs on the carbon film. Representative TEM images of the GeNWs are shown in Figure 4.6. All the NWs are straight with uniform diameters through the length. Diameters of the NWs in Figure 4.6a are in the range of 10-50 nm. A high magnification TEM of a single GeNW with its catalyst tip (dark spot) is shown in Figure 4.6b. The metal capping catalyst particle at the front reveals that VLS mechanism is responsible for the NW growth process.

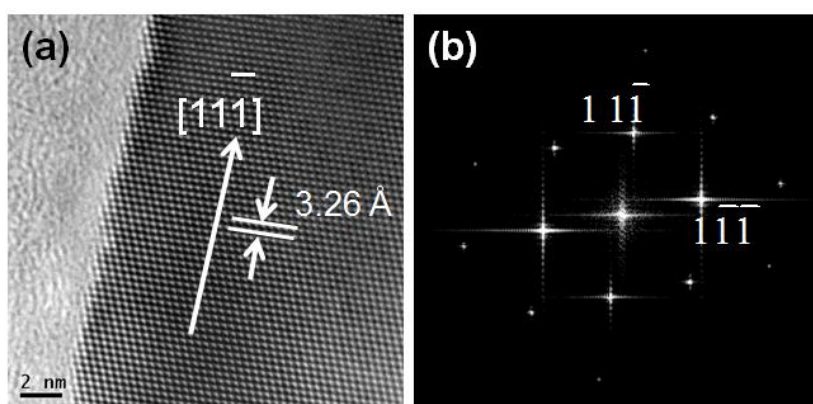


Figure 4. 7 (a) HRTEM and (b) FFT pattern of a GeNW. The HRTEM image is taken along $[101]$ zone axis. Growth direction of the NWs is along $[111]$ direction.

A lattice-resolved HRTEM image of the GeNWs is shown in Figure 4.7a. The NW possesses a perfect single crystal structure with no defects. The corresponding two dimensional fast Fourier transform (FFT) pattern is shown in Figure 4.7b. Index to the pattern suggests that the HRTEM is taken along the $[101]$ zone axis. Growth direction of the GeNW is along $[111]$ direction. Measured spacing of 3.26 \AA corresponds to the spacing between (111) planes of cubic Ge phase, confirming that the growth direction of the NW is along $[111]$.

All the NWs characterized show the same growth direction of $[111]$. HRTEM images of NWs with different diameters are shown in Figure 4.8. Determination of the growth direction is based on lattice spacing measurements and indices of the corresponding FFT patterns.

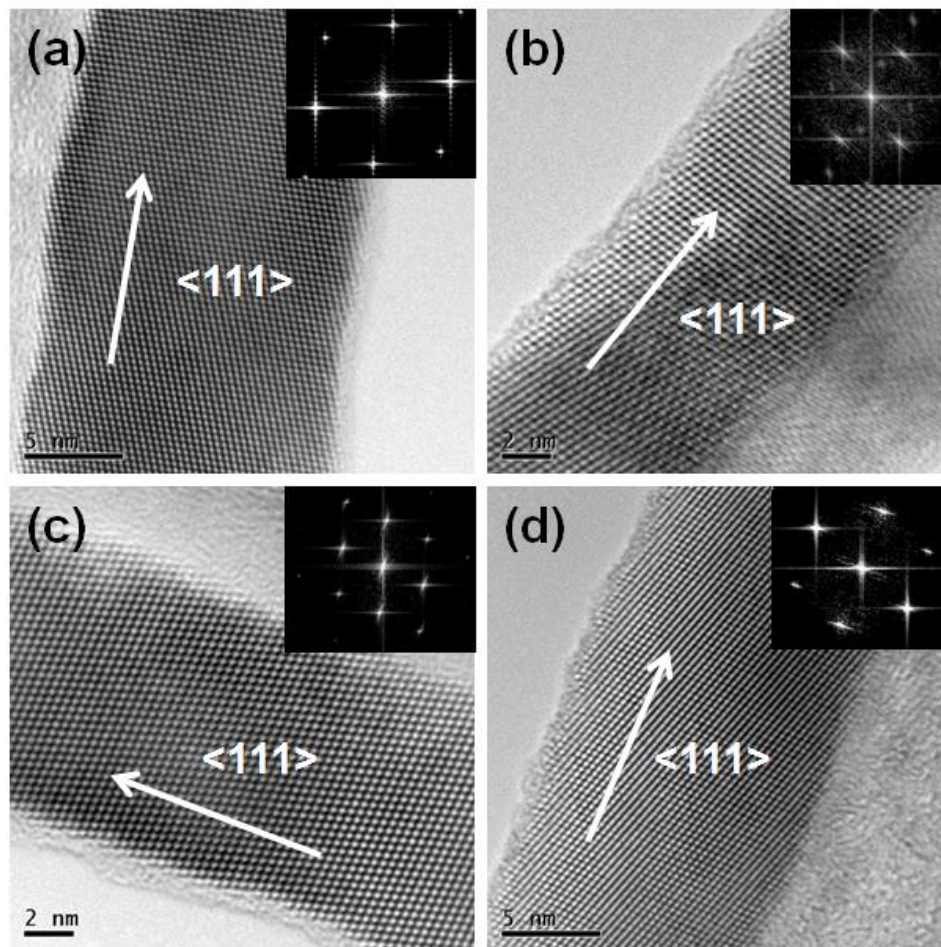


Figure 4. 8 HRTEM images and corresponding FFT patterns of GeNWs with different diameters. All the NWs characterized show the same growth direction along $\langle 111 \rangle$.

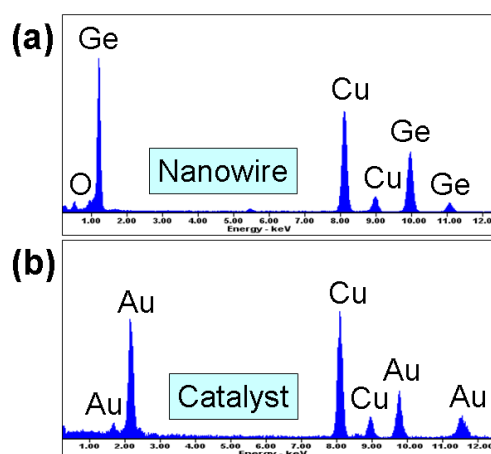


Figure 4. 9 EDS spectra of the (a) NW stems and (b) catalyst particles.

Chemical compositions of the NWs and catalyst particles are analyzed using EDS. EDS spectra taken from the NW stems and catalyst particles are shown in Figure 4.9a and b, respectively. The results show that the NWs are composed of Ge and the catalyst particles are composed of Au. Peaks of Cu come from the Cu grid used to support the NW for TEM characterization. The EDS spectra confirm the successful synthesis of GeNWs using Au as catalysts via VLS growth mechanism.¹

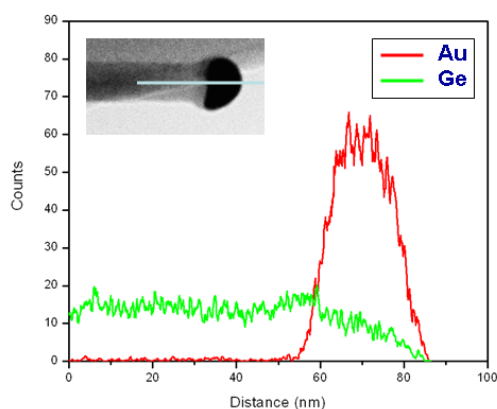


Figure 4. 10 EDS line scanning profile across a catalyst particle at the front of NW. Ge (green line) and Au (red line) distribution are shown in the profile.

EDS line scanning profile can be used to determine the elemental composition distribution either along the radial or axial directions. Figure 4.10 is a typical EDS line scanning profile across a catalyst particle. Ge distributes uniformly along the NW and Au concentration is

below the detection level in the NW. The strong peak at the dark spot region reveals that the metal catalyst particle is mainly composed of Au. The line scanning spectrum gives a better view of the composition distribution along the axial growth direction of the NW, which would help to improve the understanding of the basic growth mechanisms.

Other characterization methods, such as optical microscopy was also used to characterize the morphologies of the GeNWs. Optical images of the GeNWs as grown on Si substrates without any treatments are shown in Figure 4.11a and b. One-dimensional nanostructures can be viewed under optical microscopy. Droplets of ethanol containing the GeNWs are dispersed on the Si substrates. Corresponding optical microscopy images of different magnifications are shown in Figure 4.11c and d. Diameters of the NWs are in the range of 10-100 nm. Unlike SEM, which is more capable of showing the 3D morphology, the focus depth of the optical microscopy is quite limited. As a result, part of the NWs not on the focus plane appears to be blurred in the images. Still, optical microscopy is useful for preliminary characterization due to the simple operation procedure, while SEM requires much more stringent operation conditions such as high vacuum. Also, optical microscopy may be useful for the observation of several types of special samples, such as NWs in liquids or samples without good conductivity.

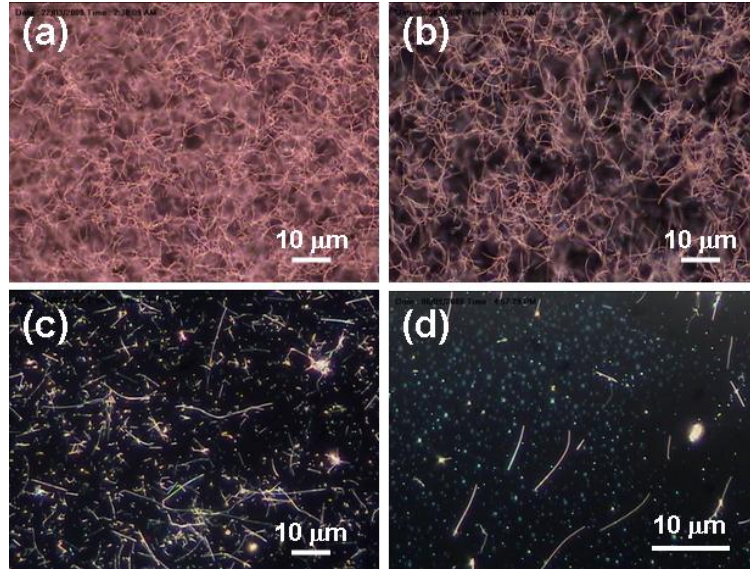


Figure 4. 11(a,b) Optical images of as-synthesized GeNWs on Si substrate with different densities; (c,d) optical images of GeNWs dispersed on Si substrates with different magnifications.

4.2.4 Effect of Growth Temperature and Pressure on the NW Morphology

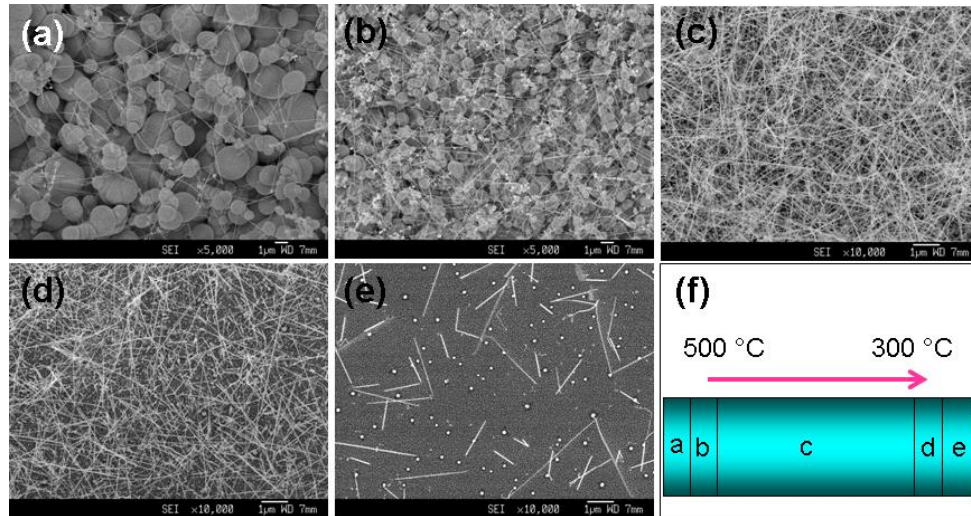


Figure 4. 12 Temperature-dependent morphologies between the temperature region of 300-500 °C.

In our furnace, the best GeNW morphologies are obtained during a temperature region of 300-500 °C. This temperature region corresponds to a 3 cm long distance in the furnace, according to the predetermined temperature profiles. But for a Si substrate lies in this region, the Ge nanostructure morphologies are not uniform. Typically, Ge large particles deposit at

the beginning of the wafer, and gradually the products change to NWs over a distance of several millimeters. Figure 4.12 illustrates the morphology variations. The products of five representative regions (Figure 4.12f) on the substrate are shown. At the front (Figure 4.12a, region a), large particles with diameters of several micrometers deposit on the wafer. When the temperature decreases, both the size and amount of the particles begin to decrease and the yield of NWs gradually increases (Figure 4.12b, region b). Pure production of NWs can be observed on most parts of the substrate (Figure 4.12c, region c). The density of the NWs would decrease with the lowering of the growth temperature (Figure 4.12d and e). This can be tentatively explained considering the different thermal conductivities of the Ar gas ($\sim 0.016 \text{ W m}^{-1} \text{ K}^{-1}$ at room temperature) and bulk Si substrate ($\sim 150 \text{ W m}^{-1} \text{ K}^{-1}$ at room temperature). The temperature profile of the furnace was measured in air. Thus, at region a, temperature of the carrier gas containing Ge vapor is around 500°C , but the actual temperature of the Si substrate should be lower due to the much higher thermal conductivity. We can expect that hot Ge vapor would condense significantly on the substrate due to the sudden temperature change, while the gas would be in thermal equilibrium with the Si substrate after a short distance. A proper Ge vapor supply and deposition rate leads to the growth of high purity NWs.

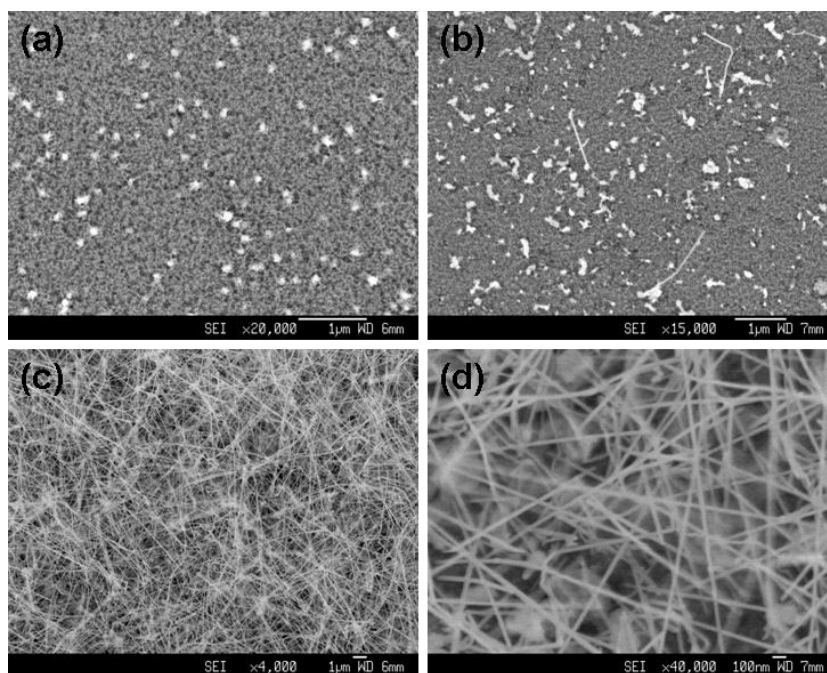


Figure 4. 13 Effect of vapor pressure inside the quartz tube on the synthesis of GeNWs: (a,b) nanoparticles or nanorods of very low yield were produced at a vapor pressure of 1×10^{-3} mbar with no introduction of Ar flow; (c,d) large scale NWs were synthesized when the vapor pressure was increased to 4.2 mbar with a Ar flow of 300 sccm.

Another critical aspect for the synthesis of large scale and high yield GeNWs is the vapor pressure inside the quartz tube during growth process. Controlled experiments were carried out under a background pressure of 1×10^{-3} mbar without introduction of Ar gas. Typical morphologies are shown in Figure 4.13a and b. Only particles or short nanorods of very low yield can be occasionally observed on the substrate. Large scale NWs can be readily synthesized at a pressure of 4.2 mbar with an Ar flow of 300 sccm (Figure 4.13c and d). No obvious morphological differences were viewed over an Ar flow range of 50-400 sccm.

4.3 Bi-Catalyzed Growth of GeNWs

4.3.1 Bi-Ge Binary Phase Diagram

Au has been the dominant metal catalyst particle for GeNWs growth due to its chemical inertness and low eutectic temperature with Ge but contamination of Au is a long-standing

concern because Au has negative effects on the performance of minority carrier in nanoelectronic devices.² Thus, it is critical to develop suitable alternative metal catalysts to advance NW-based device technologies. There are few reports on the use of non-gold catalysts for NW growth.

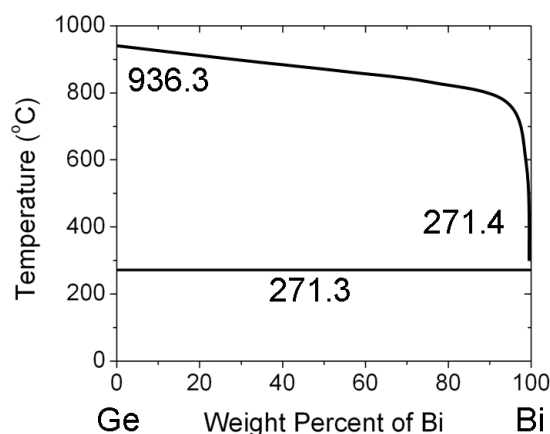


Figure 4. 14 Binary phase diagram of Bi-Ge.

On the basis of Bi-Ge phase diagram (Figure 4.14), there are no stoichiometric compounds in Bi-Ge binary systems.¹⁹ Also, Bi is a good candidate for GeNW synthesis due to the low eutectic point of Bi-Ge. The eutectic temperature of Bi-Ge (271 °C) is even lower than that of Au-Ge (361 °C). Low eutectic temperature is critical for NW synthesis under mild conditions, making them compatible with semiconductor integration technologies. Also, low temperature synthesis is desirable for NW growth on organic substrates and for solution-phase synthesis to alleviate solvent decomposition.¹³

4.3.2 Experimental Methods

Mixed bismuth, germanium and carbon powders (molar ratio Bi:Ge:C=1:20:20) were used as source materials and loaded at the center of the furnace. Central temperature was increased to 1000 °C at a rate of 10 °C min⁻¹ and kept for 60 min under a constant Ar flow of 200 sccm. Either cleaned Si substrates or Cu grids were placed at the lower temperature region (around

300 °C) to collect the products. We found that Bi has the ability to catalyze GeNW growth in vapor phase. Detailed structure and composition analyses were carried out using SEM, TEM and EDS.

4.3.3 Morphological and Structural Characterizations

Figure 4.15 contains the representative SEM images of the Bi-catalyzed GeNWs grown on Si substrate (Figure 4.15a) and Cu grid (Figure 4.15b-d). Apart from the 1D NWs, Bi nanoparticles were also observed on the substrates.

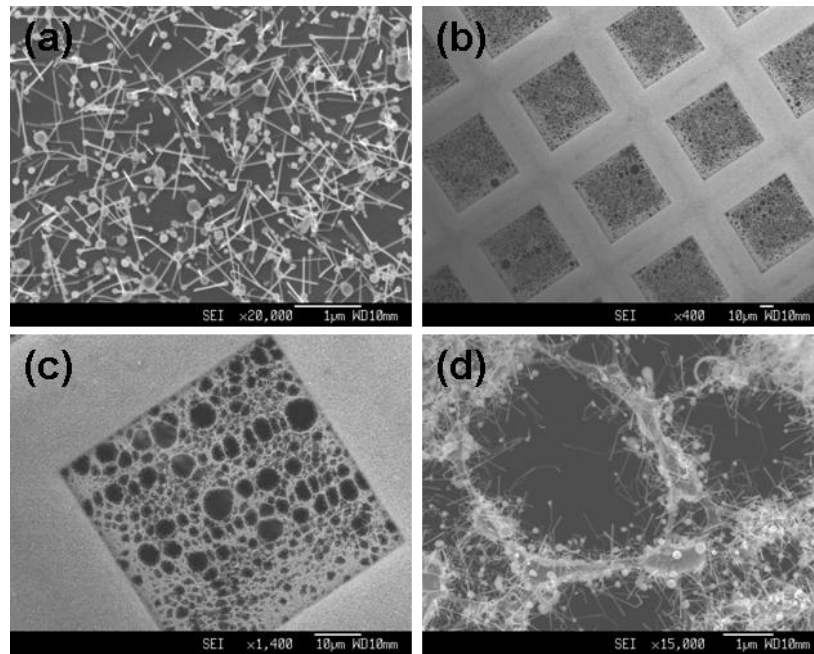


Figure 4. 15 (a) SEM image of Bi-catalyzed GeNWs grown on Si substrate. The large particles are Bi particles deposited on the substrate. (b-d) SEM images of different magnifications of GeNWs grown on Cu grid. GeNWs can be observed at the edges of the holey carbon film (d).

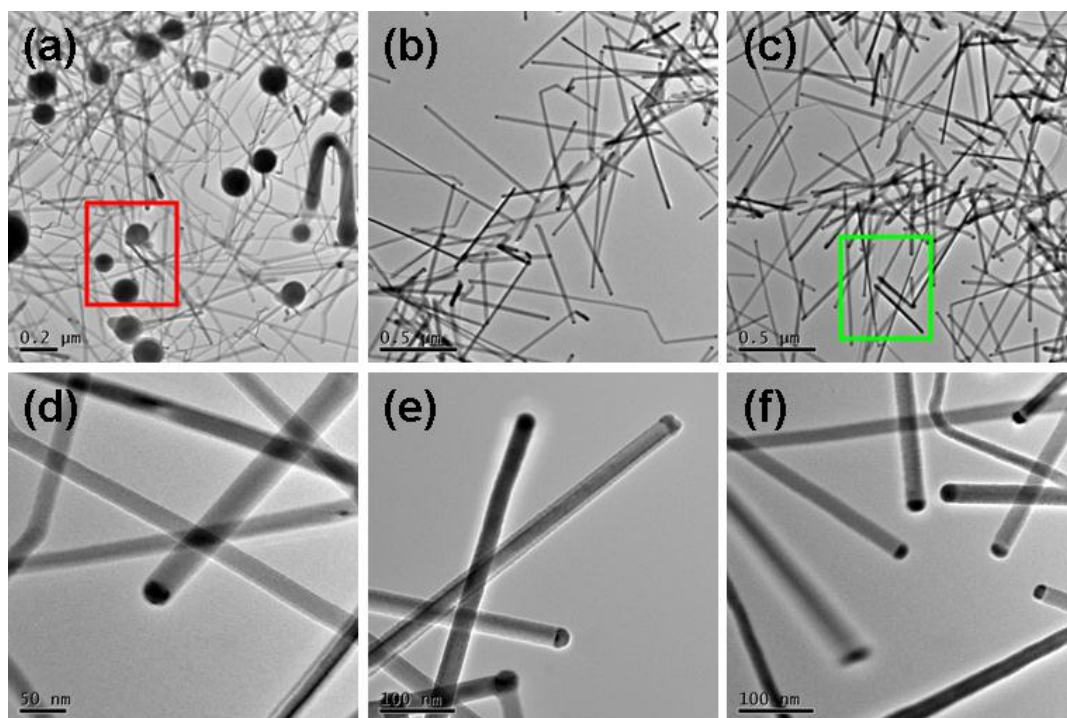


Figure 4. 16 (a-c) Low magnification and (d-f) high magnification TEM images of the GeNWs grown on Cu grids. Metal catalyst particles (dark spots) can be clearly observed at the growth fronts as shown in (d-f).

The NWs grown on Cu grids were used for TEM characterization without further treatments. Low magnification and high magnification TEM images of the GeNWs are shown in Figure 4.16a-c and d-f, respectively. Most of the NWs are straight with lengths of micrometers long. Diameters of the NWs are in the range of 10-40 nm. As shown in Figure 4.16a, besides the 1D NW structures, large particles were also deposited on the Cu grid. Metal catalyst particles (Figure 4.16d-f) were clearly observed at the growth fronts of the NWs, which is a characteristic phenomenon revealing the VLS growth mechanism. The NWs are of high yield and high purity when grown using the experimental conditions described above (molar ratio Bi:Ge:C=1:20:20).

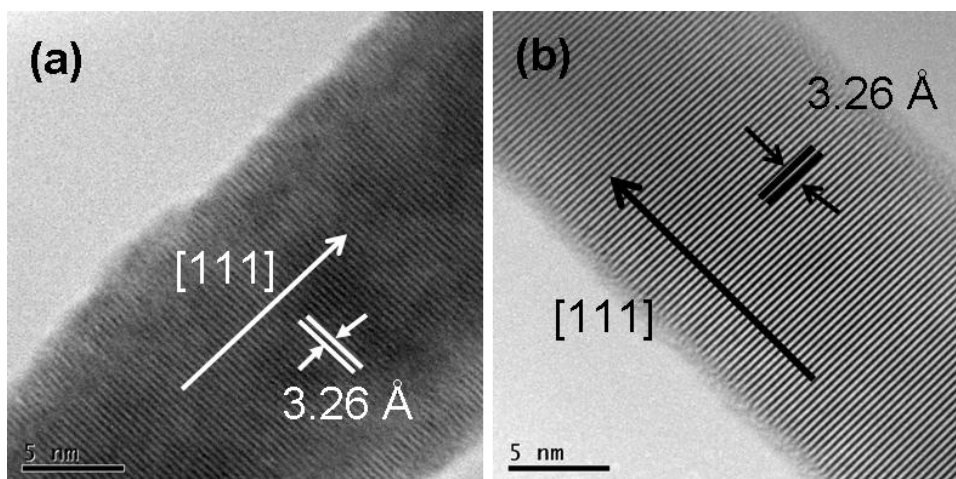


Figure 4. 17 HRTEM images of the GeNWs. All the NWs characterized show the growth direction along [111].

HRTEM images of the GeNWs are shown in Figure 4.17. The NWs are single crystalline with growth direction along [111], which is the same as those grown using Au as catalysts. The GeNWs grown in solution phase with Bi catalysts were also growing primarily along [111] directions.¹³ Measured lattice spacing of 4.26 Å corresponds to the spacing between (111) planes of Ge with diamond cubic structure.

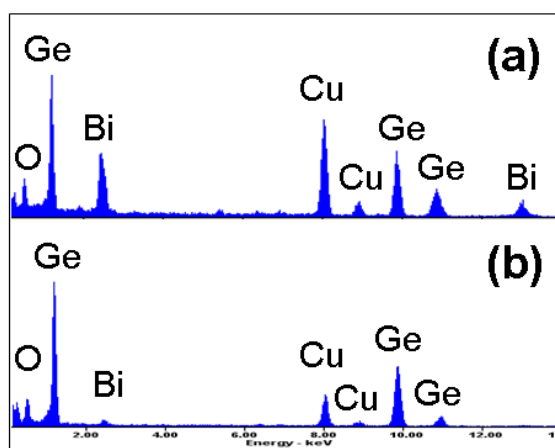


Figure 4. 18 EDS spectra taken from different regions of the sample: (a) areas including large metal particles; (b) areas that only include NWs.

Chemical compositions of the NWs and catalyst particles were analyzed using EDS attached to the TEM system. EDS spectra were taken from two different regions as marked by red and green rectangles in Figure 4.16a and c, respectively. Corresponding results are shown in

Figure 4.18a and b. The spectrum from areas without large particles shows a small peak of Bi while the Bi peak is much stronger for areas with the large particles. The comparison reveals that the large metal particles are composed of Bi. The small Bi peak originates from the catalyst particles at the growth fronts (Figure 4.16d-f).

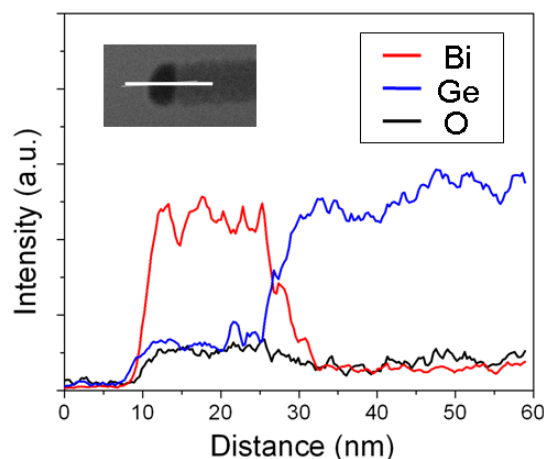


Figure 4. 19 EDS line scanning profile across a GeNW and its Bi catalyst particle.

EDS line scanning profile across a catalyst particle is shown in Figure 4.19. The scanning results show that the catalyst particle and the NW are composed of Bi and Ge, respectively. This confirms the successful synthesis of GeNWs using Bi as metal catalysts. Ge and O elements are absent from the catalyst particle.

4.3.4 Growth Mechanisms

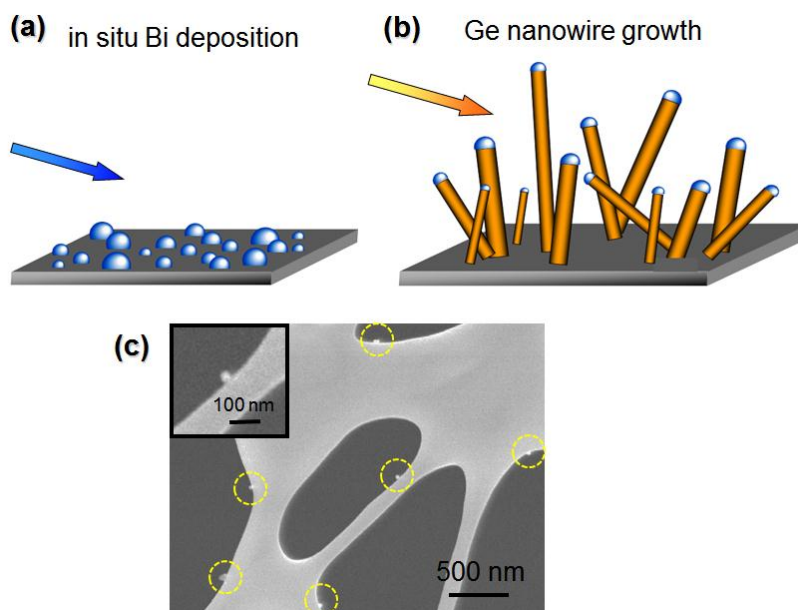


Figure 4. 20 (a,b) Schematic illustration of the GeNW growth process using Bi catalyst. **(c)** SEM image of the Cu grid (substrate) after a short deposition time of 5 min. Bi nanoparticles (highlighted by circles) can be observed on the substrate.

The growth process of GeNWs with Bi catalyst particles can be explained by VLS mechanism.¹ The melting point of Bi (271.3 °C) is much lower than that of Ge (936.3 °C); thus we expect that Bi would evaporate first when the furnace was heated to 1000 °C. This is confirmed by our SEM observations of the Cu grid after a short deposition time of 5 min (Figure 4.20c), where Bi nanoparticles can be clearly viewed. Liquidus droplets of Bi condensed on the carbon film when Bi vapor was brought to lower temperature region by Ar flow (Figure 4.20a). Ge vapor concentration would increase significantly when the temperature was increased above its melting point (936.3 °C). Continuous adsorption of Ge vapor to the droplet surface resulted in axial NW growth after supersaturation (Figure 4.20b).

4.3.5 Effect of Bi/Ge Molar Ratio on the NW Morphology

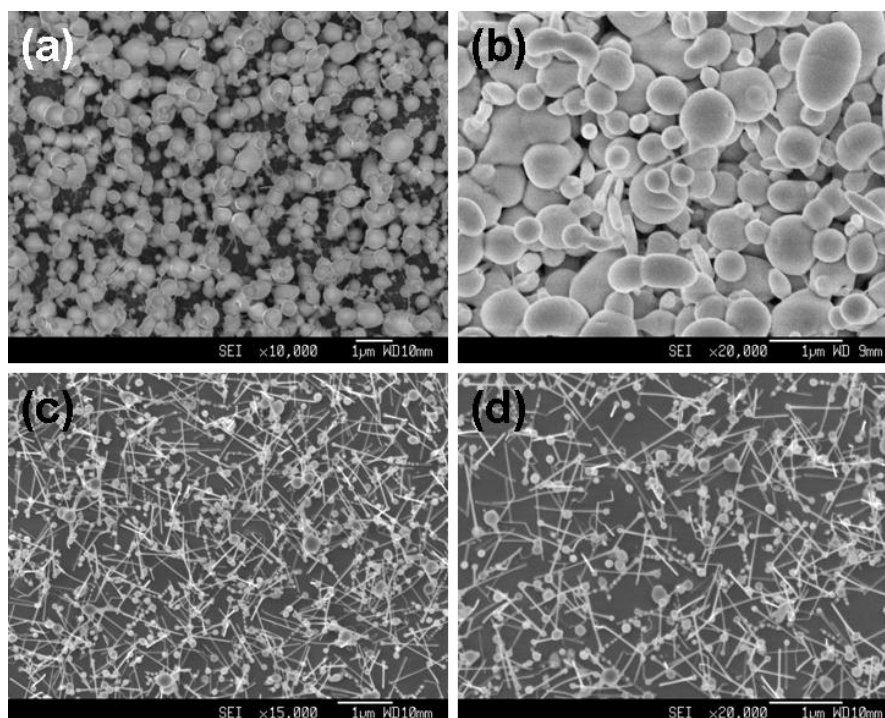


Figure 4. 21 SEM images of the products synthesized using source materials of different Bi/Ge molar ratios: (a,b) 1:5; (c,d) 1:20.

One key aspect which enables the successful synthesis of GeNWs is the molar ratio of Bi/Ge in the source materials. Controlled experiments showed that the best NW morphologies were obtained with a Bi/Ge ratio of 1/20. When the molar ratio is higher than 1/10, mainly large Bi particles of micrometer sizes or continuous Bi films formed on the substrate. Representative product morphologies using source materials with a Bi/Ge molar ratio of 1/5 are shown in Figure 4.21a and b. The multilayer particle deposition and large diameter of the Bi particles significantly inhibit the formation of NWs. However, both the yield and purity of the NWs could be greatly improved when source materials with a Bi/Ge ratio of 1/20 were used (Figure 4.21c and d). The density of the NWs started to decrease when the molar ratio was even lower. A proper Bi content in the source materials is critical to ensure the formation of small Bi particles with desired densities, which later serve as catalyst particles for GeNW

growth. In the case of Ge synthesis in solution phase, similar yield and purity variations with catalyst concentration were also reported.¹³

4.4 Single GeNW and Networks for Visible-Light Photodetectors

4.4.1 Introduction

Semiconducting 1D nanomaterials have been widely used for chemical,²⁴ biological²⁵ and light sensors.²⁶ The nanostructures are expected to exhibit better performances (such as high sensitivity, high selectivity, fast response and reset time, *etc*) than their bulk or thin film counterparts due to the high surface-to-volume ratio. Photodetection is one of the most important applications of NW sensors and extensive studies have been reported in literature.^{17,26-29} However, it should be highlighted that most of the previous studies focused on the photodetection using single-NW devices, which required complex, low-yield and high-cost lithography techniques. Moreover, the difficulty in NW assembly has seriously hindered the development of large scale single-NW devices. Alternatively, macroscale NW-network devices are of increasing interest recently since they exhibit sufficiently good or even better performances but only require facile and low-cost fabrication techniques.³⁰⁻³²

Ge ($E_g = 0.68$ eV at room temperature) has been considered as a promising material for photodetection because it responds to a wide spectral range (from ultraviolet to infrared) and is compatible with Si technology.^{33,34} Previously, GeNW arrays embedded in anodized aluminium oxide (AAO) template¹⁷ and single GeNW field effect transistors (FETs)³⁵ have been used for visible light detection. Herein, we fabricated visible-light photodetectors using single-NW and NW-networks, respectively. And we demonstrate that the photoresponse time

of GeNW photodetectors can be significantly improved by using percolated GeNW networks, instead of single NW, as building blocks.

4.4.2 Device Fabrication Methods

For device fabrication, standard optical-lithography followed by Cr/Au (10/50 nm) deposition and liftoff was used to define the contact electrodes. GeNWs suspended in ethanol were dispersed on top of the electrodes. The NW concentration in solution was adjusted to obtain single-NW and NW-network devices. The contact conditions of single-NW devices were improved by Pt deposition in FIB system (assisted by our collaborators Prof. Gan's group in NTU). Photoresponse characteristics of the GeNW photodetectors were measured in Keithley semiconductor parameter analyzer. Tungsten-halogen lamp with tunable light intensity in the probe station was used as light source. Typical wavelength spectra of the light source are shown in Figure 4.22.³⁶ All the measurements were performed at room temperature in ambient conditions.

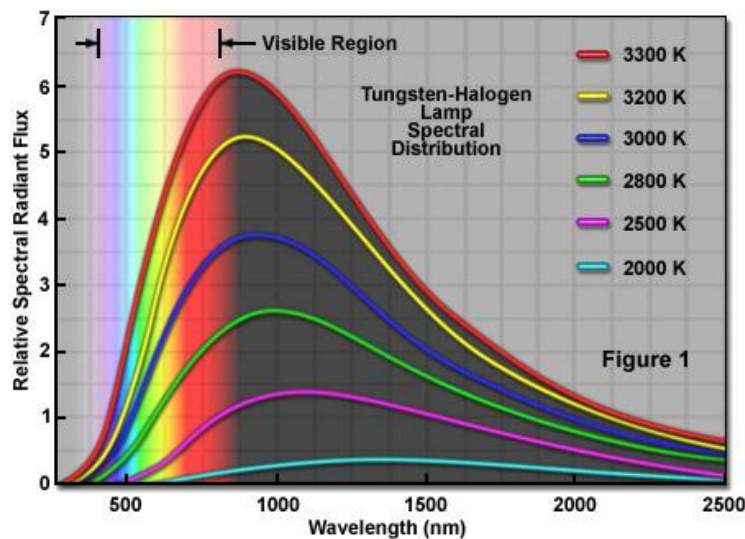


Figure 4. 22 Typical wavelength spectra from the tungsten-halogen lamp at different emission temperatures.³⁶ The light source used in present study was the tungsten-halogen lamp in the optical microscope of the probe station. The light intensity of the lamp can be tuned within the range of 0.02–0.8 mW cm⁻⁴.

4.4.3 Comparative Studies of Single NW and Network Devices

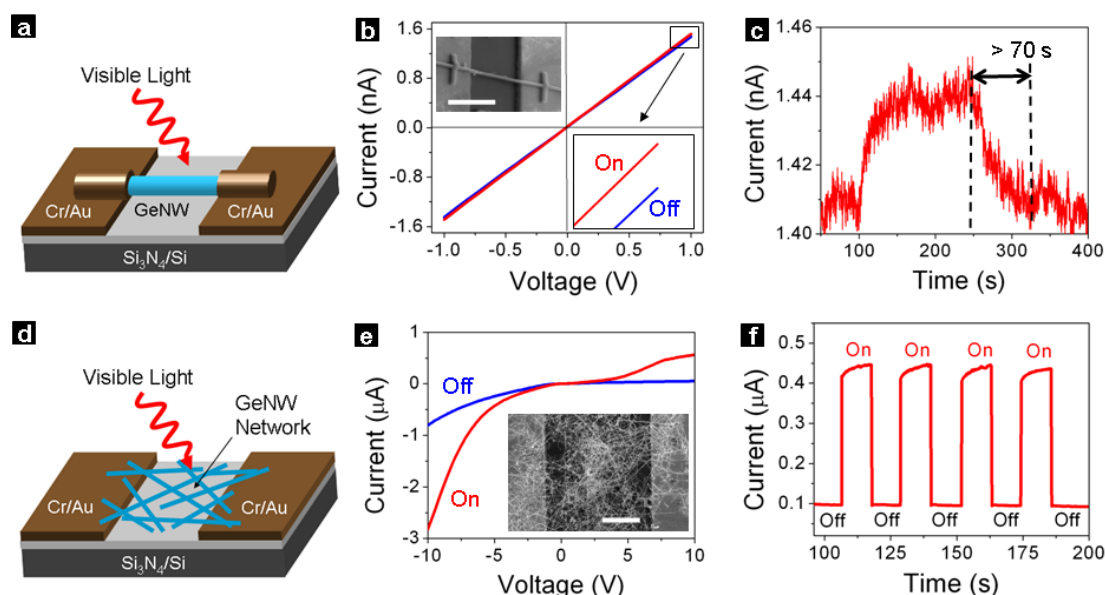


Figure 4. 23 Comparison of the photoresponse behaviors of single-NW device and network device. Schematic models, I - V curves and photoresponse characteristics of (a-c) single-NW device and (d-f) NW-network device.

Visible light photodetectors based on single NW and NW networks were fabricated for comparison studies. Schematic model, I - V curve and photoresponse characteristic of the single-NW devices are shown in Figure 4.23a-c, respectively. Diluted NW solution was used to reduce the NW concentration and facilitate single-NW device fabrication. Focused-ion-beam (FIB) deposited Pt pads were used to obtain reliable contacts between the NW and underlying Au electrodes. A representative SEM image of the single-NW device is shown in Figure 4.23b inset. Ohmic conductance was observed for those single-NW devices, as suggested by the highly linear I - V characteristic curves (Figure 4.23b). When the light was turned on ($\sim 0.8 \text{ mW cm}^{-2}$), the conductance increases from 1.41 nS to 1.44 nS at a fixed bias of 1 V. To further characterize the photoresponse behavior of the single-NW device, current as a function of time was measured when the light was turned on ($\sim 0.4 \text{ mW cm}^{-2}$) and off, as shown in Figure 4.23c. Slow response and reset time was observed. For example, the measured photocurrent reset time is larger than 70 s for the single-NW device (Figure 4.23c).

Slow response and reset time of tens of seconds were typically observed for other the single-NW devices in literature. For example, the photocurrent of single ZnO NW photodetector cannot recover to its initial value even after ~ 2500 s.³⁷ A slow current decay process was also observed by He *et al.* in ZnO NW UV sensors (>1000 s).³⁸

However, the response and reset time can be greatly improved by using NW networks (instead of single NW) as the active detection channel. Photoresponse performances of the network devices are shown in Figure 4.23e-f. Non-linear I - V curves were typically observed for the network devices (Figure 4.23e), indicating a barrier-dominated conducting mechanism (details will be discussed below). The current as a function of time was measured to characterize the response and reset time for the network device, when the light was periodically turned on and off. A fully reversible switching behavior was observed. More importantly, the network devices exhibited fast response and reset time within 1 s. An enlarged view of the current decay process with a reset time of 0.2 s is shown in Figure 4.24a.

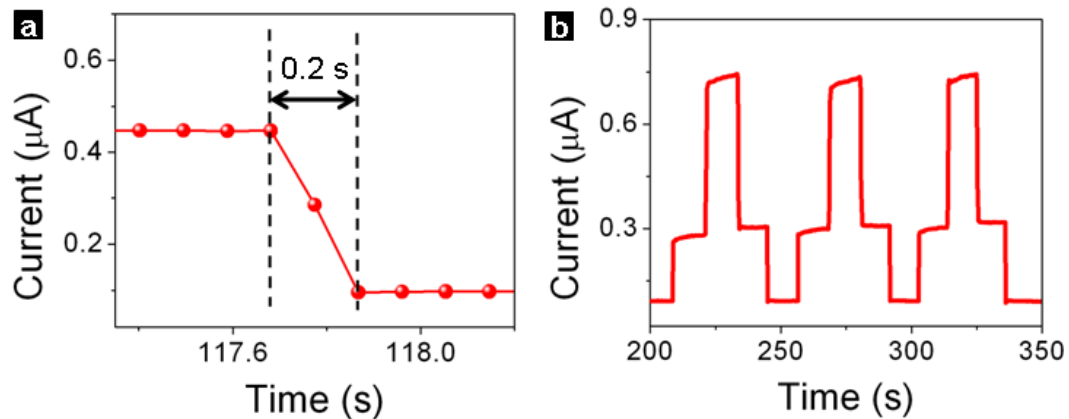


Figure 4. 24 (a) Enlarged view of a current decay process showing the fast reset time of 0.2 s. (b) Multiple step photoresponse characteristics of network devices.

Fast photoresponse time is a highly desirable characteristic for commercial light sensing applications. It enriches the potential functionalities of photodetectors, such as the efficient tracing of light with variational intensities. As a typical example, the multi-step light

detection using NW-network device was demonstrated (Figure 4.24b). The light intensities for the 3 steps are $\sim 0.02 \text{ mW cm}^{-2}$, 0.3 mW cm^{-2} and 0.8 mW cm^{-2} , corresponding to the current levels of $0.1 \text{ }\mu\text{A}$, $0.3 \text{ }\mu\text{A}$ and $0.7 \text{ }\mu\text{A}$, respectively. As can be clearly viewed, the fast response and reset time of the network devices enables the efficient depiction of the light intensity variations. However, the significant delay resulted from the slow response and reset time for the single-NW device makes them inferior choices. Note that the relative yield of single-NW and NW-network devices can be controlled by tuning the NW concentration in solution and the solution volume dropped between the electrodes.

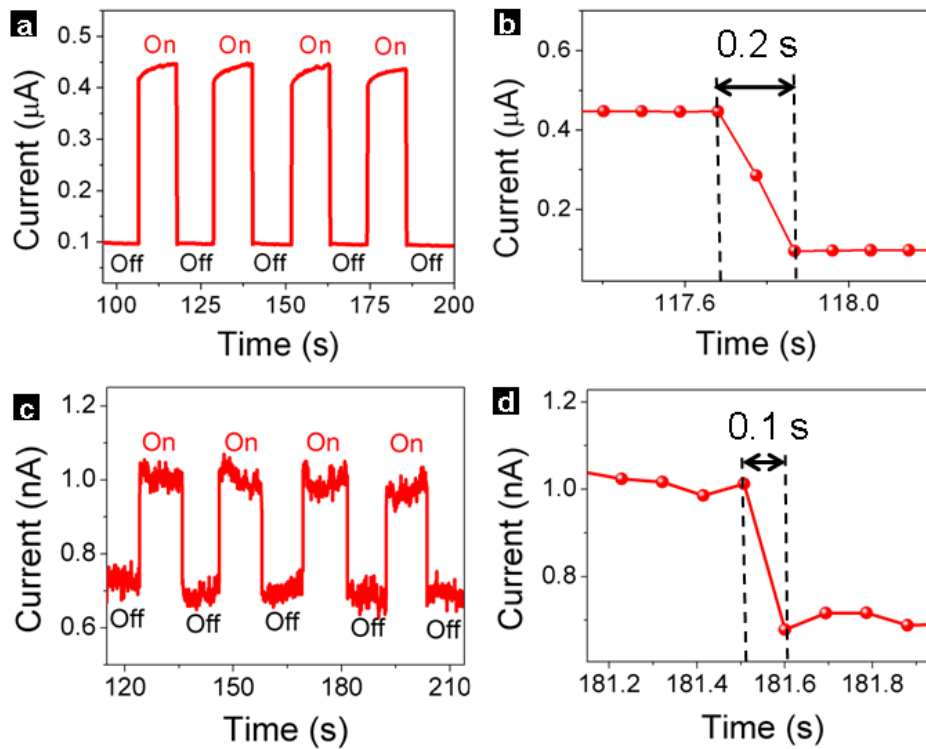


Figure 4. 25 Photoresponse characteristics of two typical NW-network devices, showing the fast photoresponse time observed.

For our network devices, the NW densities were estimated to be typically in the range of 100-500 (area between the source-drain contacts is $15 \times 500 \text{ }\mu\text{m}^2$). Although the current values of the network devices varied from device to device due to the different NW densities and contact conditions (conduction mechanisms will be discussed below), fast photoresponse time was exclusively observed for all the network devices, indicating a good reproducibility.

Comparison of two typical NW-network devices showing different current values but fast photoresponse times is shown in Figure 4.25. The device in Figure 4.25a-b is the one from Figure 4.23d-f, with a fast response time of 0.2 s. The ON and OFF currents are 0.44 μA and 0.09 μA , respectively. Another NW-network devices showed much lower ON and OFF current values of ~ 1 nA and ~ 0.7 nA, respectively. However, fast response time of 0.1 s (which is the detection limit in our measurement system) is also observed. The conductance variation of network devices is a result of several factors, such as the NW amounts lying between the electrodes, contact points and junctions in the networks, *etc.* Further explanations of those factors affecting the network conductances will be presented in the following section.

4.4.4 Conduction and Detection Mechanisms

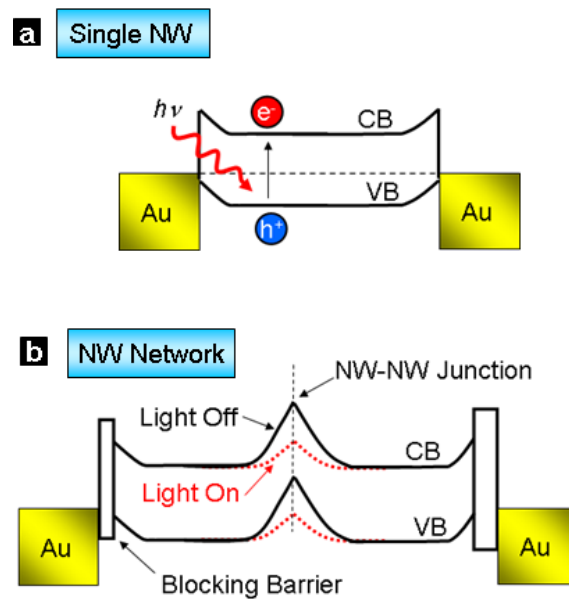


Figure 4. 26 Schematic band diagrams for single-NW device with Ohmic contact and network device with non-Ohmic contact, at zero bias. Rectangles represent the partial contributions that are not light-sensitive (see text for more details).

Next we discuss the electron conduction mechanisms for the GeNW photodetectors. Schematic band diagrams of the single-NW and NW-network devices are shown in Figure 4.26a and b, respectively. It is known that GeNWs without surface passivation quickly form a

thin oxide layer at the surface.^{39,40} The high density of Ge/GeO_x interfacial states (negative charge traps) would induce hole accumulation at the NW surface, resulting in *p*-type semiconducting behavior for the namely undoped GeNWs.^{41,42} It has also been experimentally demonstrated that the Fermi level at metal/Ge interface is strongly pinned near the valance band edge of Ge,⁴³ as shown in Figure 4.26a and b. As a result, the Schottky barrier at Au-GeNW interface is expected to be negligible considering the *p*-type conduction and Fermi level pinning (FLP) effect. This is consistent with the Ohmic conductance observed for single-NW devices (Figure 4.23b). It should be noted that the FIB-improved good contact conditions also contribute to the Ohmic conductance, by reducing the blocking barriers at the contact regions (see Figure 4.26b and discussion below).

Non-Ohmic and asymmetric conductance was observed for NW-network devices (Figure 4.23e), and can be understood based on the following aspects. First, significant blocking barriers exist at the Au-GeNW interfaces (Figure 4.26b), due to the poor contact conditions of the drop-cast process without further improvement (such as Pt deposition by FIB). The two blocking barriers possess different heights or widths, probably due to the different NW numbers and contact conditions. This explains why asymmetric conductance was observed for network devices (Figure 4.23e). The Au-GeNW blocking barrier (as well as the NW-NW junction barrier shown below) may physically originate from the small contact area, thin surface insulating layer and surface adsorbates. Note that this blocking barrier can be effectively reduced during FIB etching/deposition processes, by enlarging the contact area, removing the surface insulating layer and adsorbates (Figure 4.27). Thus, good Ohmic contact was observed for the single-NW devices (Figure 4.23b). Second, the electron conduction in percolated NW networks is dominated by the NW-NW junction barriers (as indicated in Figure 4.26b),^{32,44,45} which are not readily available in single-NW devices.

Previous studies of individual NW-NW junction also revealed the dominant resistance of the junction barrier.^{46,47} Both the blocking barrier at the Au-GeNW interface and NW-NW junction barrier contribute to the non-Ohmic conductance of the network devices. In Figure 4.26b, the rectangles (with different widths and heights) are used to represent the partial contributions from the small contact area and surface insulating layer, which are not light-sensitive. The rectangles are omitted in the NW-NW junction barrier for clarity purpose. The bending bands are used to represent the electron depletion/hole accumulation layers (response to incident light), which originate from the surface charge/adsorbates.

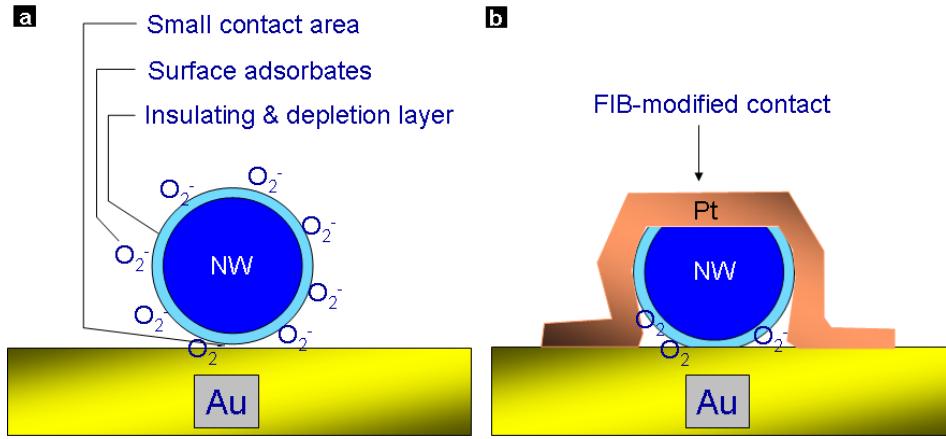


Figure 4. 27 Schematic models for the Au-GeNW contact (a) before and (b) after FIB modification.

The different conduction mechanisms for the single-NW and NW-network devices lead to the distinct photoresponse behaviors. It is known that for GeNWs exposed in air, oxygen molecules would adsorb on the NW surface by capturing free electrons [$O_2(g) + e^- \rightarrow O_2^-(ad)$].^{27,35} Both the charge traps and oxygen adsorbates contribute to the surface electron depletion and hole accumulation. Upon light illumination, electron-hole pairs can be generated [$h\nu \rightarrow e^- + h^+$]. The holes (dominant carriers for *p*-type NW) would be attracted to the NW surface to fill the charge traps (discharging process) or desorb the oxygen adsorbates. The carrier densities would gradually increase as the traps are filled and the oxygen adsorbates are desorbed. It should be noted that both the hole diffusion (to discharge the

negative charge traps)⁴¹ and oxygen desorption processes²⁷ are quite slow, as have already been demonstrated in previous studies. Consequently, the carrier density (and hence conductivity) of the GeNW would increase gradually upon light illumination. For single-NW device with Ohmic contact, the resistance is determined by the NW itself. The slow increase of the NW conductivity resulted in the slow response time (Figure 4.23c). An analogous current decaying process can be observed when the light was turned off. The slow surface trap charging and oxygen re-adsorption processes (reverse processes) lead to the slow photocurrent reset time, which was shown to be over 70 s (Figure 4.23c).

The fast response and reset time for NW-network devices can be attributed to the barrier dominated conductance. Note that the surface charge and adsorbates induced band-bending (Figure 4.26b) are sensitive to incident light and can be treated as Schottky barriers.³² The NW-NW junction barrier is analogous to two back-to-back Schottky barriers. The increased carrier density (upon illumination) in GeNW would narrow the barrier width, which is equivalent to a lowering of the effective barrier height. As a result, the conductivity of the percolated NW network would increase, since the narrowed (lowered) barriers allow easier electron tunneling and transportation. It should be highlighted that this light-induced barrier height modulation is much faster than the trap discharging or oxygen diffusion processes (which usually accounts for photodetectors with Ohmic contact). For example, previous studies showed that the photocurrent response time for Au-CdS⁴⁸ and Pt-ZnO²⁹ Schottky barriers were typically below 1 s. However, the time required for trap discharging or oxygen diffusion was usually on the order of several minutes or up to hours.^{27,41,49-52} Previously, Zhou *et al.* reported that the reset time of ZnO NW photodetectors could be enhanced by intentionally deposited Schottky contact on single NW.²⁹ Here we show that the NW network devices with Schottky-like barrier dominated conductance exhibited comparable

performances. More importantly, network devices require less-intense lithography techniques and allow potential large-scale fabrications.

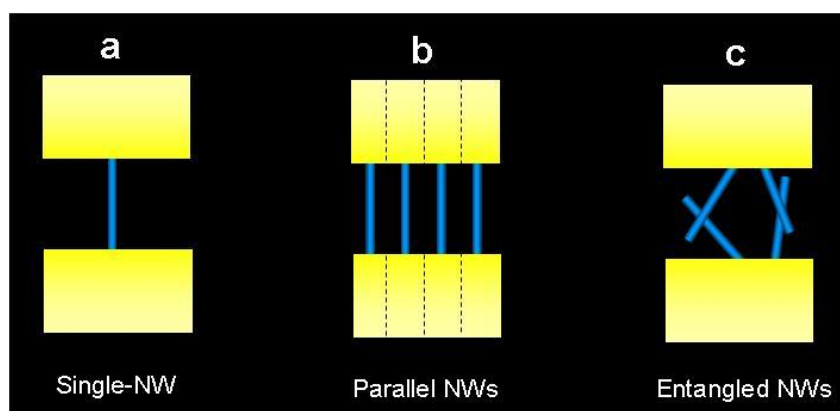


Figure 4. 28 Schematic diagrams of single-NW, parallel-NW and entangled-NW devices.

As discussed above, the fast photoresponse time is associated with the intrinsic property of the NW-NW junctions, which dominate the electron conduction in entangled NW networks. Recently, photodetectors using multiple ZnS nanobelts were demonstrated.⁵³ While most of the ZnS nanobelts were in direct contact with the counter electrodes (quasi-parallel), no photoresponse time enhancement was observed when compared with single ZnS nanobelt devices.⁵³ The parallel NW device (positioned side-by-side, Figure 4.28) can be treated as multiple single-NW devices working simultaneously and independently. They should exhibit the same photoresponse time as single-NW device, although the current values would be enlarged correspondingly. Note that it is not necessary to remove the Au catalysts for photodetector applications. Although Au serves as deep level trap and is detrimental to the carrier mobility of Ge, the photosensing properties have little to do with the mobility. The response time and wavelength selectivity are associated with the intrinsic properties of semiconductor bandgap, oxygen adsorption/desorption and responsive behaviors of NW junctions.

4.5 Conclusions

In this chapter, we have presented the synthesis of high quality GeNWs using both conventional Au and novel Bi catalysts. Comparative studies of single GeNW and network devices for visible light detection are also demonstrated.

Single-crystalline GeNWs were grown via Au-catalyzed VLS method. Detailed morphology, crystal phase and chemical compositions of the NWs were characterized using XRD, SEM, TEM and EDS. Diameter of the NWs can be controlled by the thickness of the Au film predeposited on the substrate. The effect of growth temperature and pressure were also carefully optimized to obtain the best NW morphology.

We have demonstrated the usage of Bi as novel catalysts to direct the vapor phase growth of GeNWs through a facile coevaporation method. Mixed Bi and Ge powders were used as source materials and the Bi nanoparticles (catalysts) would deposit at the low temperature region first due to the much lower melting temperature than Ge. Those Bi nanoparticles can serve as efficient catalysts for GeNW growth according to the Bi-Ge binary phase diagram, which shows a low eutectic temperature of 271 °C. High quality GeNWs with uniform diameters were successfully grown on substrates. Further characterizations confirmed the chemical compositions of the catalyst and NW stem, verifying our proposed growth mechanism. The Bi/Ge molar ratio in the source material has to be carefully optimized to achieve high purity NW growth.

Photodetectors using single GeNW and network detection channels were fabricated and characterized. Single NW photodetectors showed Ohmic conductance (improved with FIB) and slow reset time (>70 s). However, asymmetric I - V curves were observed for the network

devices, indicating a barrier dominated resistance for the network conduction channel. Fast photoresponse time (<1 s) was observed for all the network devices. Detailed conduction and photodetecting mechanisms of the single NW and network devices are presented. The fast photoresponse time of network devices is enabled by the unique junction dominated conductance, which is not available in single NW devices. We suggest that network devices are highly promising solutions for future industrial photodetector applications.

References:

- (1) Wanger, R. S.; Ellis, W. C. *Applied Physics Letters* **1964**, *4*, 89-90.
- (2) Allen, J. E.; Hemesath, E. R.; Perea, D. E.; Lensch-Falk, J. L.; Li, Z. Y.; Yin, F.; Gass, M. H.; Wang, P.; Bleloch, A. L.; Palmer, R. E.; Lauhon, L. J. *Nature Nanotechnology* **2008**, *3*, 168-173.
- (3) Sprokel, G. J.; Fairfield, J. M. *J. Electrochem. Soc.* **1965**, *112*, 200-203.
- (4) Bullis, W. M. *Solid State Electron.* **1966**, *9*, 143-168.
- (5) Ding, Y.; Gao, P. X.; Wang, Z. L. *Journal of the American Chemical Society* **2004**, *126*, 2066-2072.
- (6) Nguyen, P.; Ng, H. T.; Meyyappan, M. *Advanced Materials* **2005**, *17*, 1773-+.
- (7) Wang, Y. W.; Schmidt, V.; Senz, S.; Gosele, U. *Nature Nanotechnology* **2006**, *1*, 186-189.
- (8) Lensch-Falk, J. L.; Hemesath, E. R.; Lopez, F. J.; Lauhon, L. J. *Journal of the American Chemical Society* **2007**, *129*, 10670-+.
- (9) Sun, X. H.; Calebotta, G.; Yu, B.; Selvaduray, G.; Meyyappan, M. *Journal of Vacuum Science & Technology B* **2007**, *25*, 415-420.
- (10) Tuan, H. Y.; Lee, D. C.; Korgel, B. A. *Angewandte Chemie-International Edition* **2006**, *45*, 5184-5187.
- (11) Fanfair, D. D.; Korgel, B. A. *Crystal Growth & Design* **2005**, *5*, 1971-1976.
- (12) Fanfair, D. D.; Korgel, B. A. *Crystal Growth & Design* **2008**, *8*, 3246-3252.
- (13) Lu, X. M.; Fanfair, D. D.; Johnston, K. P.; Korgel, B. A. *Journal of the American Chemical Society* **2005**, *127*, 15718-15719.
- (14) Greytak, A. B.; Lauhon, L. J.; Gudiksen, M. S.; Lieber, C. M. *Applied Physics Letters* **2004**, *84*, 4176-4178.
- (15) Xiang, J.; Lu, W.; Hu, Y. J.; Wu, Y.; Yan, H.; Lieber, C. M. *Nature* **2006**, *441*, 489-493.
- (16) Ahn, Y. H.; Park, J. *Applied Physics Letters* **2007**, *91*, 162102.
- (17) Polyakov, B.; Daly, B.; Prikulis, J.; Lisauskas, V.; Vengalis, B.; Morris, M. A.; Holmes, J. D.; Erts, D. *Advanced Materials* **2006**, *18*, 1812-+.
- (18) Duan, X. F.; Lieber, C. M. *Advanced Materials* **2000**, *12*, 298-302.
- (19) Massalski, T. B. *Binary Alloy Phase Diagrams*; 1st ed.; ASM International Metals Park, Ohio, 1986.
- (20) Kodambaka, S.; Tersoff, J.; Reuter, M. C.; Ross, F. M. *Science* **2007**, *316*, 729-732.
- (21) Wang, D. W.; Tu, R.; Zhang, L.; Dai, H. J. *Angewandte Chemie-International Edition* **2005**, *44*, 2925-2929.

- (22) Wang, D. W.; Dai, H. J. *Angewandte Chemie-International Edition* **2002**, *41*, 4783-4786.
- (23) Gudiksen, M. S.; Lieber, C. M. *Journal of the American Chemical Society* **2000**, *122*, 8801-8802.
- (24) McAlpine, M. C.; Ahmad, H.; Wang, D. W.; Heath, J. R. *Nature Materials* **2007**, *6*, 379-384.
- (25) Zheng, G. F.; Patolsky, F.; Cui, Y.; Wang, W. U.; Lieber, C. M. *Nature Biotechnology* **2005**, *23*, 1294-1301.
- (26) Kind, H.; Yan, H. Q.; Messer, B.; Law, M.; Yang, P. D. *Advanced Materials* **2002**, *14*, 158-+.
- (27) Soci, C.; Zhang, A.; Xiang, B.; Dayeh, S. A.; Aplin, D. P. R.; Park, J.; Bao, X. Y.; Lo, Y. H.; Wang, D. *Nano Letters* **2007**, *7*, 1003-1009.
- (28) Hsieh, C. H.; Chou, L. J.; Lin, G. R.; Bando, Y.; Golberg, D. *Nano Letters* **2008**, *8*, 3081-3085.
- (29) Zhou, J.; Gu, Y. D.; Hu, Y. F.; Mai, W. J.; Yeh, P. H.; Bao, G.; Sood, A. K.; Polla, D. L.; Wang, Z. L. *Applied Physics Letters* **2009**, *94*.
- (30) Unalan, H. E.; Zhang, Y.; Hiralal, P.; Dalal, S.; Chu, D. P.; Eda, G.; Teo, K. B. K.; Chhowalla, M.; Milne, W. I.; Amaratunga, G. A. J. *Applied Physics Letters* **2009**, *94*.
- (31) Cao, Q.; Kim, H. S.; Pimparkar, N.; Kulkarni, J. P.; Wang, C. J.; Shim, M.; Roy, K.; Alam, M. A.; Rogers, J. A. *Nature* **2008**, *454*, 495-U4.
- (32) Yan, C. Y.; Singh, N.; Lee, P. S. *Applied Physics Letters* **2010**, *96*, 053108.
- (33) Tang, L.; Kocabas, S. E.; Latif, S.; Okyay, A. K.; Ly-Gagnon, D. S.; Saraswat, K. C.; Miller, D. A. B. *Nature Photonics* **2008**, *2*, 226-229.
- (34) Assefa, S.; Xia, F. N.; Vlasov, Y. A. *Nature* **2010**, *464*, 80.
- (35) Ahn, Y. H.; Park, J. *Applied Physics Letters* **2007**, *91*.
- (36)
- (37) Zhou, J.; Gu, Y. D.; Hu, Y. F.; Mai, W. J.; Yeh, P. H.; Bao, G.; Sood, A. K.; Polla, D. L.; Wang, Z. L. *Applied Physics Letters* **2009**, *94*, 191103.
- (38) He, J. H.; Chang, P. H.; Chen, C. Y.; Tsai, K. T. *Nanotechnology* **2009**, *20*, 135701.
- (39) Zhang, L.; Tu, R.; Dai, H. J. *Nano Letters* **2006**, *6*, 2785-2789.
- (40) Wang, D. W.; Chang, Y. L.; Wang, Q.; Cao, J.; Farmer, D. B.; Gordon, R. G.; Dai, H. J. *Journal of the American Chemical Society* **2004**, *126*, 11602-11611.
- (41) Hanrath, T.; Korgel, B. A. *Journal of Physical Chemistry B* **2005**, *109*, 5518-5524.
- (42) Sdong, H. K.; Jeon, E. K.; Kim, M. H.; Oh, H.; Lee, J. O.; Kim, J. J.; Choi, H. J. *Nano Letters* **2008**, *8*, 3656-3661.
- (43) Nishimura, T.; Kita, K.; Toriumi, A. *Applied Physics Letters* **2007**, *91*.
- (44) Sysoev, V. V.; Goschnick, J.; Schneider, T.; Strelcov, E.; Kolmakov, A. *Nano Letters* **2007**, *7*, 3182-3188.
- (45) Kolmakov, A.; Potluri, S.; Barinov, A.; Montes, T. O.; Gregoratti, L.; Nino, M. A.; Locatelli, A.; Kiskinova, M. *Acs Nano* **2008**, *2*, 1993-2000.
- (46) Cui, Y.; Lieber, C. M. *Science* **2001**, *291*, 851-853.
- (47) Duan, X. F.; Huang, Y.; Cui, Y.; Wang, J. F.; Lieber, C. M. *Nature* **2001**, *409*, 66-69.
- (48) Lubberts, G.; Burkey, B. C.; Bucher, H. K.; Wolf, E. L. *Journal of Applied Physics* **1974**, *45*, 2180-2190.
- (49) Lao, C. S.; Park, M. C.; Kuang, Q.; Deng, Y. L.; Sood, A. K.; Polla, D. L.; Wang, Z. L. *Journal of the American Chemical Society* **2007**, *129*, 12096-+.
- (50) Liu, Y.; Zhang, Z. Y.; Xu, H. L.; Zhang, L. H.; Wang, Z. X.; Li, W. L.; Ding, L.; Hu, Y. F.; Gao, M.; Li, Q.; Peng, L. M. *Journal of Physical Chemistry C* **2009**, *113*, 16796-16801.
- (51) He, J. H.; Chang, P. H.; Chen, C. Y.; Tsai, K. T. *Nanotechnology* **2009**, *20*.
- (52) Fang, F.; Futter, J.; Markwitz, A.; Kennedy, J. *Nanotechnology* **2009**, *20*.
- (53) Fang, X. S.; Bando, Y.; Liao, M. Y.; Zhai, T. Y.; Gautam, U. K.; Li, L.; Koide, Y.; Golberg, D. *Advanced Functional Materials* **2010**, *20*, 500-508.

CHAPTER 5 Synthesis of Zn_2GeO_4 (ZGO) NWs

for Selective Deep-UV Photodetection

5.1 Objective

Apart from Ge, we are also interested in exploring other Ge-based compounds for innovative photodetector applications. Ternary germanates are typically wide bandgap semiconductors, which are of particular interest for photodetector applications with high wavelength selectivity. Zinc germanate (ZGO, Zn_2GeO_4) is a representative ternary wide bandgap germanate materials with interesting optical and electronic properties.

ZGO, a ternary oxide with a wide bandgap of 4.68 eV, has attracted great attentions for various applications. For example, ZGO doped with Mn is known to emit green light¹, while undoped ZGO is a native defect phosphor exhibiting white luminescence under UV excitation.² Thin-film electroluminescent (TFEL) devices using ZGO as active layer have been developed for potential display applications.^{1,3} ZGO was also shown to be stable photocatalyst for decomposition of water or organic pollutants.^{4,5} However, most of the previous studies focused on the optical properties of ZGO and studies on the (opto-)electronic properties are quite limited. We are interested in exploring novel ZGO nanostructures for photodetector applications.

The fabrication of bulk phase ZGO is relatively simple by solid state reaction. However, the controllable synthesis of ZGO nanostructures is still a great challenge in literature. Until very recently, ZGO nanorods were successfully obtained by solution-involved methods, *i.e.*, either by surfactant-assisted hydrothermal method⁵ or aging Zn-containing Ge nanoparticles in

water.⁶ The nanorods obtained are of small aspect ratio and severely agglomerated. Fabrication of ZGO NW electronic devices is rather difficult using those short nanorods and hence it is necessary to explore alternative synthetic methods, to produce high quality NWs (high yield, high purity, large aspect ratio, high crystallinity, *etc*).

In this chapter, we will demonstrate the successful synthesis of high quality ZGO nanowires via Au-catalyst VLS mechanism. The as-grown products were carefully characterized to give a comprehensive view of their morphology, crystal phases and chemical compositions. Detailed growth mechanisms are also discussed aiming to achieve decent control over the NW structures. ZGO NW based superstructures (kinked NWs and nanorings) and heterostructures (branched ZGO-ZnO nanotrees) are also presented, demonstrating a high level morphological control. Finally, ZGO NWs were used as efficient photodetectors for selective detection of deep-UV light. NW networks were used as the detection channels in those devices, since they were shown to be superior choices than single-NW in the studies of Ge NW photodetectors. We are able to achieve fast photoresponse time (<1 s) in ZGO NW network devices and we have also demonstrated the excellent wavelength selectivity.

5.2 Chemical Vapor Deposition of ZGO NWs

5.2.1 Experimental Methods

Mixed ZnO, GeO₂ and carbon powder (~0.5 g, molar ratio of 2:1:3) was placed at the sealed end of the small quartz tube. Si(100) substrate with 9 nm Au film was placed at the open end of the small quartz tube for product collection. Central temperature of the surface was increased to 1000 °C at a rate of 15 °C min⁻¹ and kept for 60 min under a constant Ar flow of 200 sccm (pressure 1.9 mbar). The Si substrate was located in the temperature region of 500-

400 °C. Different temperature regions have been tested for the NW growth through a series of experiments, and this was determined to be the optimum temperature region with the best NW growth in terms of yield and purity. After growth the furnace was allowed to cool naturally to room temperature.

5.2.2 Structural Characterizations

We would like to mention that compared with elemental or binary nanomaterials, synthesis of ternary nanomaterials with stoichiometric compositions is more complex and challenging. The simultaneous vapor supply of different source materials were previously achieved by placing precursor powders at different temperature zones.^{7,8} However, in our case where Ge and ZnO were used as source materials, we suggest that the coevaporation at 1000 °C is essential to ensure sufficient Ge and Zn vapor supplies for the growth of ZGO NWs. First, the melting point of bulk Ge is 937 °C. Based on our experiments of Ge NW growth (Ge powder as source material), sufficient Ge vapor supply and hence a moderate NW growth rate can only be obtained when the source powder was heated up to 950-1000 °C. The vapor pressure was significantly lower when lower heating temperature was used (e.g. 900 °C) since the Ge powders were still in solid state (no melting observed after growth). Second, mixed ZnO and carbon powder was one of the most common source materials for ZnO NW growth in vapor phase. Previous reports showed that heating temperatures above 900 °C were essential to generate sufficient Zn vapor through carbothermal reactions.^{9,10} Thus, a heating temperature of 1000 °C was used to generate Ge (through direct evaporation of Ge powder) and Zn (through carbothermal reduction of ZnO) vapors for NW growth in our experiment.

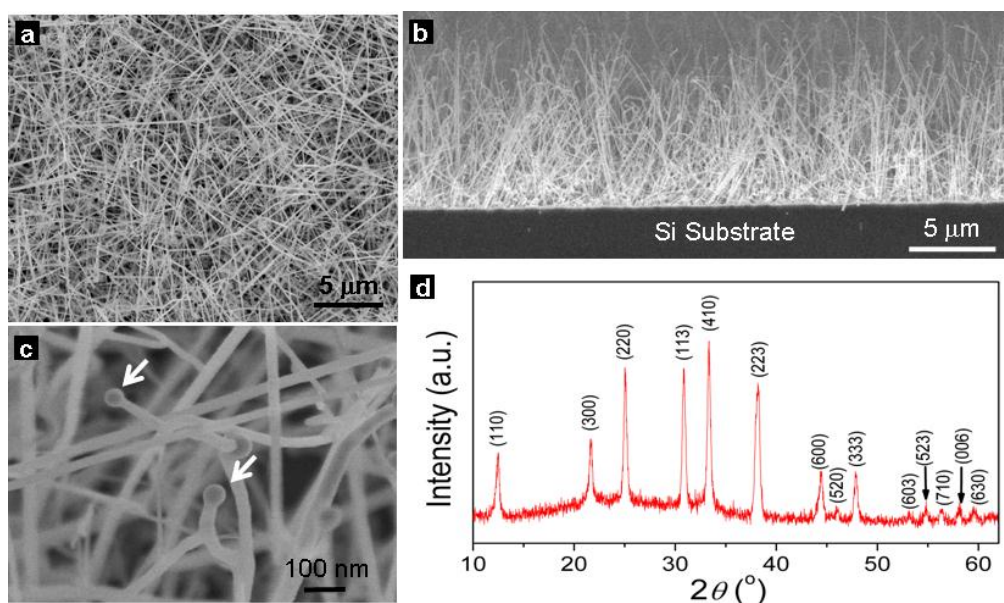


Figure 5. 1 (a) Low magnification top-view and (b) cross-sectional view SEM images of the dense ZGO NWs. (c) Enlarged SEM image showing the Au catalyst particles at the NW growth fronts. (d) XRD pattern showing a pure rhombohedral ZGO phase.

Morphologies and crystal structure of the products were first characterized using SEM and XRD. Figure 5.1a is a typical top-view SEM image of the NWs. Large quantities of NWs with a high density were successfully grown on the substrate. Enlarged view of the NWs is shown in Figure 5.1c. Metal catalyst particles can be clearly observed at the growth fronts of the NWs (indicated by arrows). Figure 5.1b is a representative cross-section view of the as-grown NWs. The diameters of the NWs are in the range of 10-80 nm with lengths of tens of micrometers. Diameter of the catalyst particle is slightly larger than that of the NW stem (Figure 5.1c). The crystal structure of the NWs was analyzed using XRD and a typical diffraction pattern is shown in Figure 5.1d. The pattern can be readily indexed to ZGO phase with a rhombohedral crystal structure (JCPDS card 11-0687: $a = 15.231 \text{ \AA}$, $c = 9.53 \text{ \AA}$). No other impurities such as Ge, ZnO or GeO_2 were detected. The XRD result indicates that the NWs are composed of a pure ZGO phase. Note that the aspect-ratios of the as-synthesized NWs are significantly higher than the nanorods obtained by solution-involved methods before,^{5,6} making them ideal candidates for further study of their electrical, optical and

chemical properties. Successful demonstration of the ZGO NWs for photodetection applications will be shown later in the chapter.

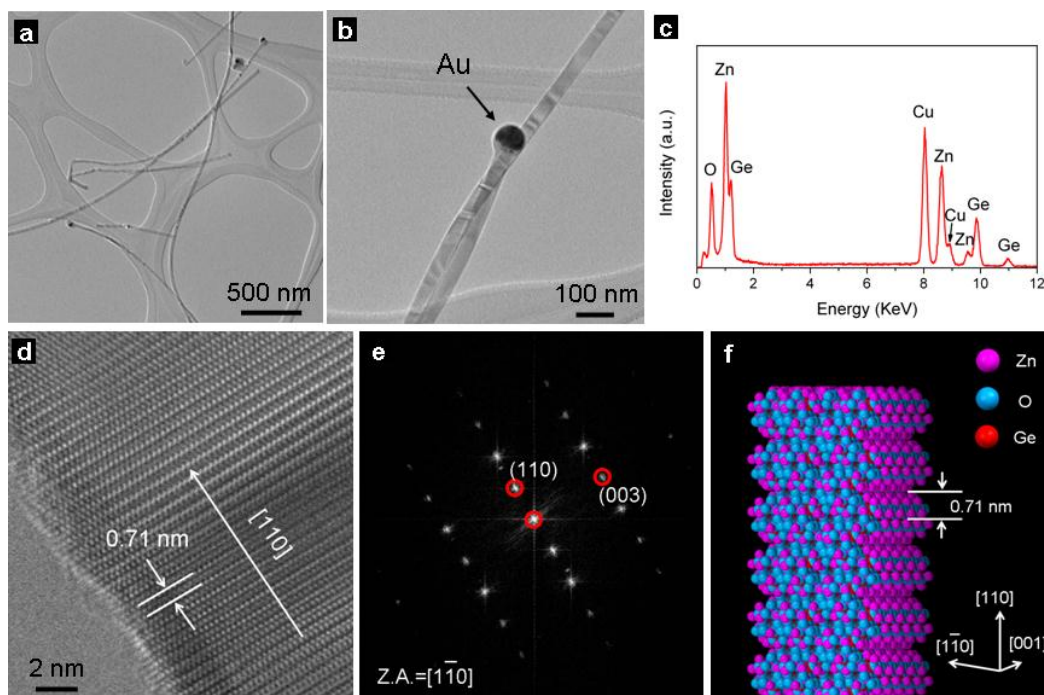


Figure 5. 2 (a) Low magnification TEM image showing the general morphology of ZGO NWs. (b) Enlarge view of two overlapping NWs, showing the Au catalyst particle. (c) EDS spectrum recorded from individual NW. (d) HRTEM image and (e) FFT pattern of the ZGO NW. The HRTEM image was taken along $[1-10]$ zone axis, showing a NW growth direction along $[110]$. (f) Space filled structure model for a ZGO NW growing along $[110]$ direction.

The structures and compositions of the NWs were further analyzed using TEM and EDS. Figure 5.2a is a typical low magnification TEM image of the ZGO NWs. Figure 5.2b is a high magnification view of two overlapping NWs, showing the metal catalyst particle at the growth front of the NW. The presence of the catalyst particles indicates that a VLS mechanism lies behind the NW growth process. Chemical compositions of the NWs were characterized using EDS attached to the TEM system. EDS spectrum taken from individual NW is shown in Figure 5.2d, revealing that the NW is composed of Zn, Ge and O. The atomic ratio of Zn to Ge is around 2, which is consistent with the stoichiometric value for ZGO. Peaks of Cu come from the Cu grid used for TEM characterization. Detailed crystal structures of the straight ZGO NWs were characterized using HRTEM. Typical HRTEM

image of the ZGO NW recorded along $[1-10]$ zone axis is shown in Figure 5.2d. Its corresponding 2D fast Fourier transforms (FFT) is shown in Figure 5.2e. Growth direction of the NW is along $[110]$ direction of the rhombohedral ZGO phase. Measured lattice spacing of 0.71 nm corresponds to the spacing between adjacent (110) planes (Figure 5.2d). Note that unlike the previously reported ternary NWs which were typically structural defective, the ZGO NWs obtained by our method are single-crystalline. Space-filled structure model along the $[1-10]$ zone axes is shown in Figure 5.2f. The atomic structure models are compiled along the $[110]$ direction in order to be consistent with the experimental HRTEM observations. As shown in Figure 5.2f, the atomic arrangement viewed along $[1-10]$ zone axis is layer-like. Experimental observations (Figure 5.2d) show excellent agreement with the space-filled structure models. Further examinations revealed that majority of the straight NWs grew along $[110]$ direction, with a small number of them exhibiting other growth directions.

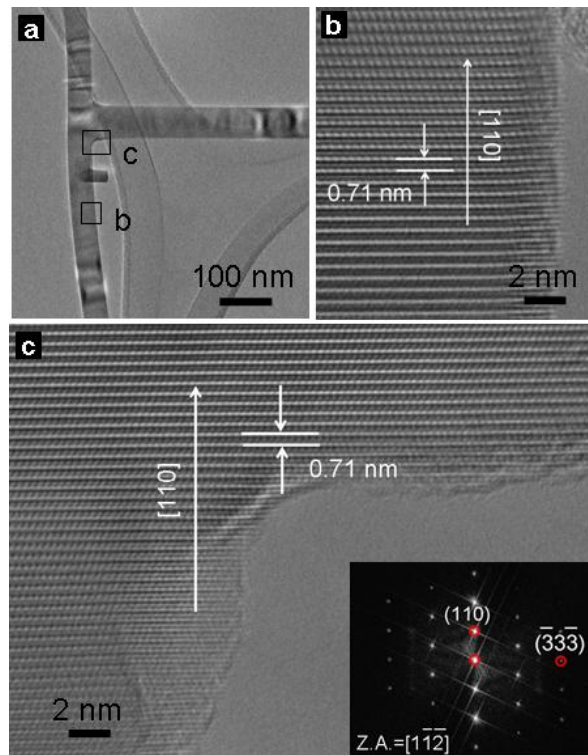


Figure 5. 3 (a) Low magnification TEM image of a branched NW structure. (b,c) HRTEM images of the backbone NW and backbone-branch junction. The corresponding positions are indicated by squares in (a). Inset in (c) is the FFT pattern along $[1-1-2]$ zone axis.

Apart from the simple straight ZGO NWs shown above, branched ZGO NWs were also observed during TEM characterizations, as shown in Figure 5.3. The branches possess preferential growth directions which are perpendicular to the backbone NWs. The specific orientations of the branches indicate the homoepitaxial growth considering the same chemical composition of the backbone and branches. Crystallographic relationships of the branched structures were characterized by HRTEM in more detail. A typical TEM image (Figure 5.3a) shows a perpendicularly grown branch with respect to the backbone NW. Corresponding HRTEM images of the backbone NW and junction (indicated by squares in Figure 5.3a) are shown in Figure 5.3b and c, respectively. The HRTEM images reveal that the branched ZGO NWs are single crystalline with no defects observed at the backbone-branch junction, in agreement with homoepitaxial growth. Growth direction of the backbone NW is along $[110]$, which is the same with the straight NWs. The branch grow along $[-11-3]$ direction, terminating with $(-11-1)$ top surface (Figure 5.3c inset); the perpendicular crystallographic relationship between the backbone NW and branch is consistent with the angle between these two directions for the rhombohedral ZGO structure.

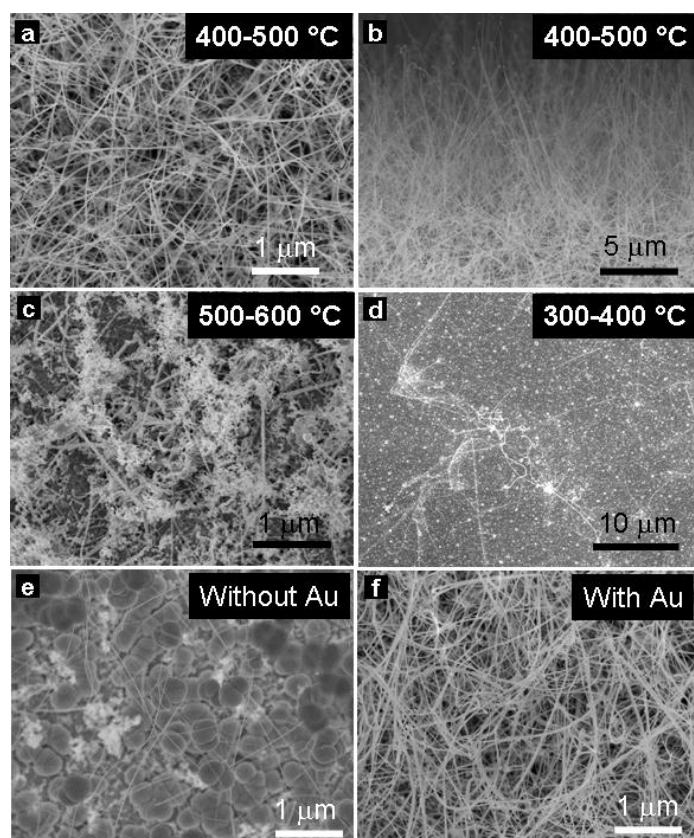


Figure 5. 4 Morphologies of ZGO NWs grown under different conditions. (a,b) Dense and uniform NWs grown between 400-500 °C. (c) Short nanorods with sponge-like impurities were deposited between 500-600 °C. (d) Very few NWs were grown between 300-400 °C. (e,f) Au catalyst was shown to be essential for the growth of high quality NWs.

Comparison experiments were performed to investigate the temperature and catalyst effects on the NW morphologies. The optimum growth temperature was found to be 400-500 °C (Figure 5.4a-b). Dense NWs with a high purity were deposited in this temperature region. However, only sparse and short nanorods with abundant sponge-like impurities were observed in 500-600 °C (Figure 5.4c). The NWs grown at 300-400 °C (Figure 5.4d) showed significantly lower yield. The optimum growth temperature was affected by various factors, such as growth mechanism, vapor pressure, oxygen concentration, source materials and even the geometric shape of the furnace system.¹¹ In our system, we have observed that the optimum deposition temperature for binary ZnO and GeO₂ NWs were also in the range of 400-500 °C. As will be shown in Figure 5.5, the growth of ternary ZGO NWs were attributed to the co-adsorption and precipitation of Zn and Ge species. Thus, it is expected that the

optimum temperature region for ZnO and GeO₂ NWs growth will also produce the best ZGO NWs. Au catalysts also play crucial role in the growth of high quality ZGO NWs (Figure 5.4e-f). Only large micro-particles with few NWs were obtained without Au catalyst (Figure 5.4e), in contrast to the dense NW deposition with Au (Figure 5.4f). This indicates that compared with the direction deposition of ZGO NWs through VS mechanism, VLS growth method is more efficient for ZGO NW production.

5.2.3 Growth Mechanisms

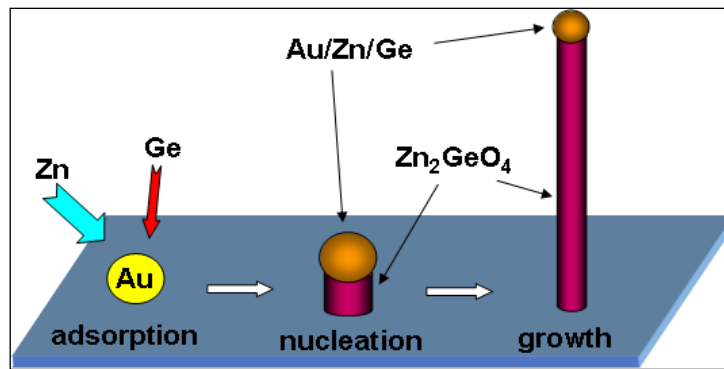
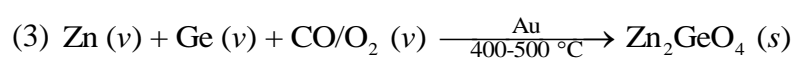
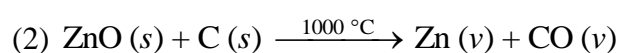
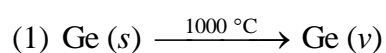


Figure 5. 5 Schematic diagram of the VLS growth process for ternary ZGO NWs. The coevaporation and adsorption of Zn and Ge vapor to the Au catalyst resulted in the growth of ternary ZGO phase.

The ZGO NWs were synthesized via VLS mechanism, where Au serves as catalyst to direct the NW growth (Figure 5.5). The detailed evaporation and deposition processes for the ternary and stoichiometric reactions are described as following: Zn and Ge vapors were generated at the high temperature region (1000 °C) either through carbothermal reduction of ZnO or direct evaporation of Ge. The vapors would diffuse to the lower temperature region due to the concentration gradients.¹² Au nanoparticles serves as preferential adsorption sites of the vapors due to their large accommodation coefficient,¹³ forming liquidus Au-Zn-Ge ternary alloy. Note that although the data of Au-Zn-Ge ternary phase diagram is lacking until now, we suggest that the catalyst particles were in liquid state during growth because the catalysts exhibit spherical shapes with smooth surfaces, which is a key indicator of the liquid

state during growth.^{14,15} When the Au nanoparticles reached supersaturation with Zn and Ge, precipitation at the alloy-substrate interface resulted in NW nucleation and growth. The relative Zn/Ge vapor concentration is controlled by the molar ratio of ZnO/Ge in the source materials and the optimum value was found to be 2 (see experimental section). The molar ratio of ZnO/Ge in the source materials determines the relative Zn/Ge concentration in the vapor and hence in the ternary Au/Zn/Ge alloy, and finally leads to the precipitation of stoichiometric ZGO NWs. However, we would like to highlight that a ZnO/Ge ratio of 2/1 in the source materials does not mean that the Zn/Ge ratio in the vapor during growth is also strictly 2/1. For example, the Zn/Ge atomic ratio in the vapor might be 3/2. But if 6.7% of the Zn and 5% of the Ge species were adsorbed and contributed to the NW growth, then we have a Zn/Ge ratio of 2/1 in the final products. Our growth process is kind of result-oriented. We found that a ZnO/Ge ratio of 2/1 would yield ZGO NWs with excellent purity, however, the detailed growth processes such as the Zn/Ge ratio in the vapor are yet unknown. Instead of the growth of Ge or ZnO NWs, the simultaneous evaporation, adsorption and precipitation of Ge and Zn containing species result in the formation of ternary ZGO phase. It was also shown previously that the ZGO phase was a thermodynamically stable phase for the ternary Zn-Ge-O system.⁶ CO or mixed CO/CO₂ vapors were generated in the carbothermal reduction reactions and acted as the oxygen sources.^{9,16} The oxygen source may also come from the residual oxygen in the furnace chamber.¹⁷ The evaporation and deposition processes can be briefly described as:



Apart from acting as the reduction agent in equation (2), carbon also serves to maintain the Ge vapor pressure during growth. Since the formation of Ge/C compound is not thermodynamically favorable,¹⁸ addition of carbon drastically prevents the molten Ge from agglomeration into large droplets. The high surface area of the Ge particles and hence a relatively constant Ge vapor pressure were retained.¹⁸

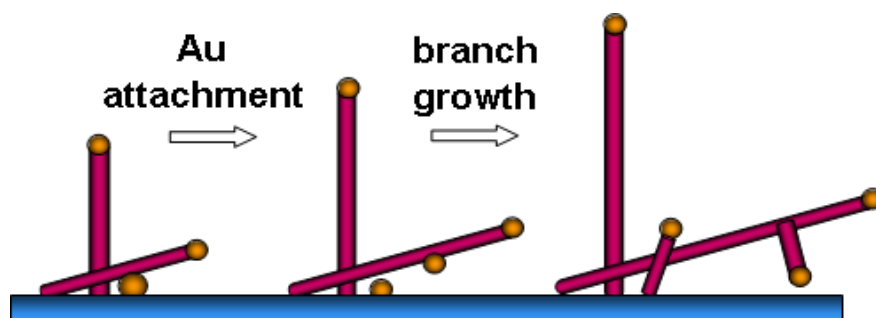


Figure 5. 6 Growth model for the branched ZGO NWs.

A growth model for the synthesis of branched ZGO NWs is shown in Figure 5.6. Previously, several methods were employed for the synthesis of branched NW structures, including secondary catalyst deposition,^{19,20} catalyst surface migration²¹⁻²⁵ and direct condensation of catalyst from the vapor phase.²⁶ However, in our case, no secondary Au catalysts were deposited to direct the branch growth. Significant Au surface diffusion is also not expected due to the usage of oxide source materials and relatively abundant residual oxygen concentration, which was shown to inhibit the Au diffusion previously.^{21,22} We suggest that the Au catalysts for secondary branching come from the Au droplets on the Si substrate, which may attach to the primary NW surface during growth and induce branch formation.¹⁷ The ZGO NWs on the substrate are of high density and multilayer stacking. The Au droplets may attach to the NW surface during growth, especially for those NWs lying at the bottom layer (nearest to the substrate surface). Consequently, the attached Au nanoparticles served as catalysts for branch growth upon continuous vapor adsorption. In contrast to the branches induced by catalysts from secondary-deposition,^{19,20} the density of ZGO branches is much

lower (typically only one branch grown on each backbone NW). Also, unlike the branches induced by catalysts from surface migration,^{23,25} the ZGO branches showed comparable diameters with the backbone NW. Moreover, only ~5% of the as-synthesized NWs were found to be branched. The low branch density, comparable diameters and low yield of the branched products can be understood according to the growth model described above.

In brief, our pioneer work on the vapor phase deposition of high quality ZGO NWs paves the way for further investigations of their interesting properties. We have demonstrated systematically the controlled synthesis of high purity ZGO NWs with high aspect ratios, as well as the effect of growth temperature and catalysts. Our understandings on the growth of this novel ternary oxide material enriches the knowledge on the controlled growth of complex ternary systems and can be readily extended to other ternary oxide nanostructures.

5.3 Pressure-Induced Kink Formation in ZGO NWs

5.3.1 Experimental Methods

While the ZGO NWs grown under stable conditions (i.e., fixed temperature and pressure) are almost exclusively straight, we demonstrate that kinked ZGO NWs can be obtained under dynamically modulated growth conditions. This may shed light on an innovative method to control the NW structures and hence properties.

The kinked ZGO NWs were grown under periodically changed pressures, with the other growth conditions kept unchanged. In a typical synthesis round of kinked NWs, Ar gas was periodically switched on (200 sccm, pressure 1.9 mbar) and off (no Ar gas, background pressure 0.03 mbar) for typical 10 cycles. The gas was turned on for 5 min and off for 5 min

in each cycle. The furnace was naturally cooled down at 1.9 mbar to room temperature after growth.

5.3.2 Single-Crystalline Kinked ZGO Superstructures

Typical TEM images of the kinked ZGO NWs are shown in Figure 5.7. Instead of the straight NWs shown in Figure 5.7, kinks were observed in the NWs synthesized under dynamically changed pressures. Previously, regularly kinked Si NWs (zigzag-shaped nanochains) were synthesized by the CVD method.²⁷ A constant angle of 120° was observed between the adjacent segments, due to the preferential <112> growth directions.²⁷ However, the ZGO NWs grown by our method showed no obvious kinking trends, i.e., no regular kinking behavior was observed. Various angles between the two straight segments were observed, as shown in Figure 5.7a-d. It should be highlighted that the entire kinked NW remains single-crystalline, despite the formation of kinks. HRTEM images of the joint sections are shown in Figure 5.7e-f. The continuous and uniform lattice fringes suggest a single-crystalline structure of the joint section. Further characterizations showed that all the kinked ZGO NWs are single-crystalline.

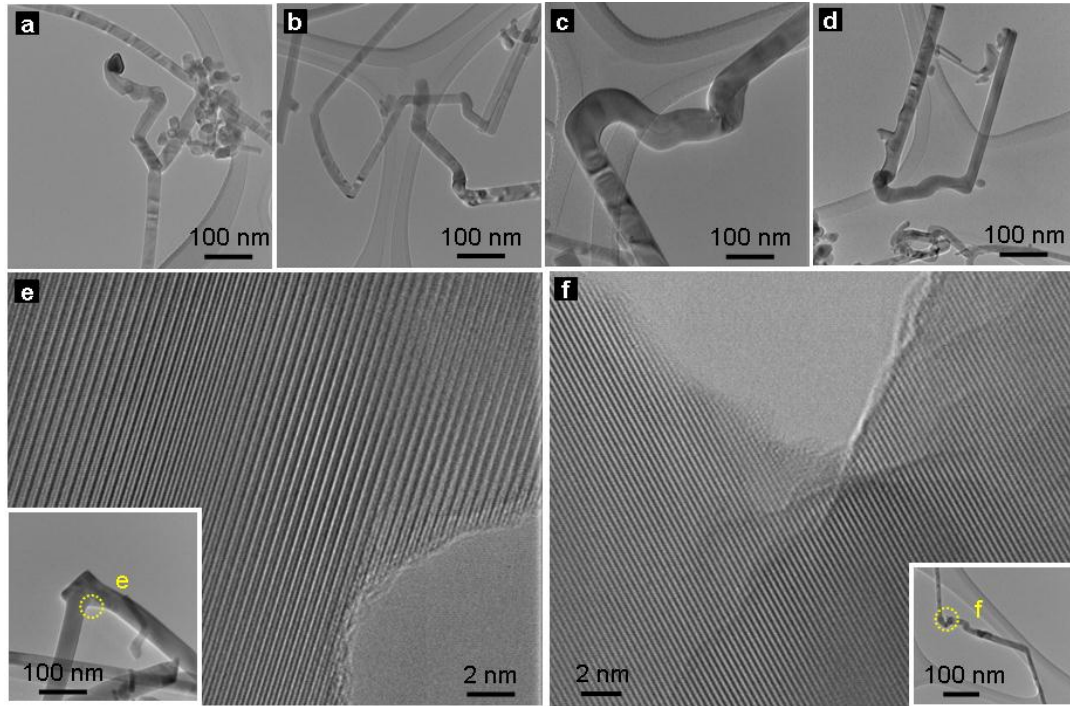


Figure 5. 7 (a-d) Low magnification TEM images of the kinked ZGO NWs. Unlike the straight NWs grown under stable growth conditions, the vapor perturbation introduces kinks in the ZGO NWs. (e-f) HRTEM images of the joint sections showing the single-crystalline structures of the kinked NWs. No structural defects were observed in the kinked NWs. Insets are the corresponding low magnification TEM images indicating the positions of the joint sections.

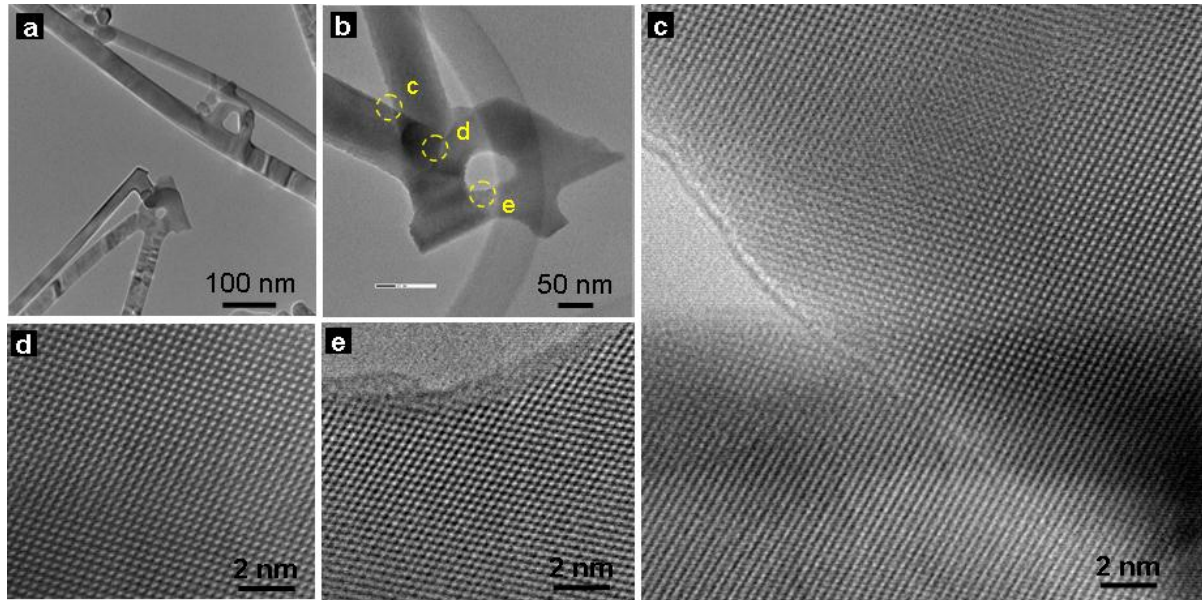


Figure 5. 8 Structural characterization of single-crystalline ZGO nanorings. (a-b) Low magnification TEM images showing the circular ring-shaped structures. (c-e) HRTEM images of different locations of the nanoring, verifying that the entire nanoring is single-crystalline.

We suggest that this controllable introduction of kinks in NWs can be employed to fold the NWs into single-crystalline nanorings. Typical examples of the ZGO nanorings are shown in

Figure 5.8. Random kinking was observed in the ZGO NWs, as shown in Figure 5.7. It is possible that the NWs would kink backward and weld with the other parts, forming single-crystalline ring-shaped nanostructures. The single-crystallinity of the nanorings is confirmed by HRTEM analyses. As shown in Figure 5.8c-e, lattice-resolved HRTEM images recorded from different locations of the nanoring (Figure 5.8b) showed uniform and consistent atomic arrangements, verifying the single-crystalline structure.

5.3.3 Expansion to Other Groups of Materials

Our further studies revealed that the present method for nanoring fabrication is generic, and can be readily applied to other materials. For example, we have been able to produce In_2O_3 single-crystalline nanoring by the vapor perturbation method (Figure 5.9). Previously, ZnO nanorings or nanorods were observed,²⁸ and the formation was attributed to the minimization trend of the electrostatic energy produced by polar charges. For other materials, closed ring-shaped nanostructures originating from 1D NWs have rarely been reported, to the best of our knowledge. But we suggest that the vapor perturbation induced NW kinking is not material dependent. Novel functional oxide nanorings could be fabricated for nanodevice applications.

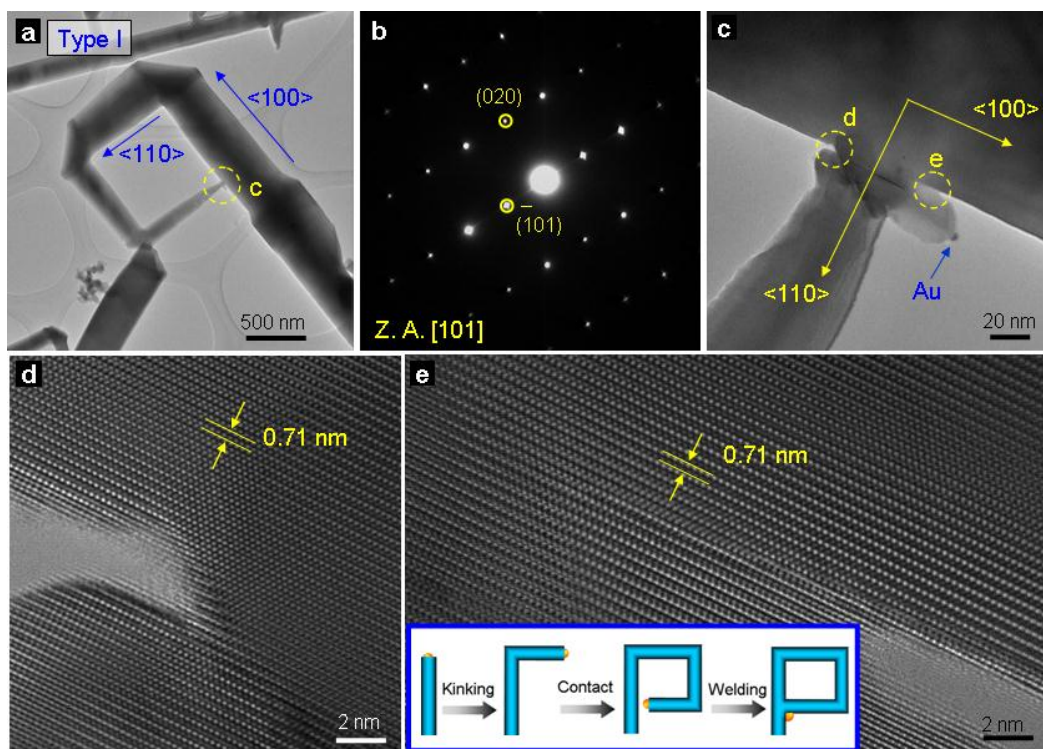


Figure 5. 9 Detailed structures of the type I nanorings formed by NW self-welding. (a) TEM image and (b) ED pattern of a typical single-crystalline type I nanoring. (c) Enlarged view of the tip-backbone joint section. Au catalyst can be viewed at the growth front. (d,e) HRTEM images of the joint sections, showing the defect-free crystallographic structure. Inset in (e) is the schematic diagram of the type I nanoring formation processes.

As a representative example, the successful synthesis of In_2O_3 nanorings is presented in Figure 5.9. Figure 5.9a is a typical low magnification TEM image of a In_2O_3 nanoring formed by kinking and welding of an individual backbone NW (self-welding). The initially straight In_2O_3 NW would kink towards another perpendicular direction due to the vapor perturbation. It is possible that the kinked tip would contact and weld with its backbone after several perturbation cycles. Corresponding ED pattern (Figure 5.9b) reveals that the entire nanoring structure is single-crystalline, with the kinked segments growing along $\langle 100 \rangle$ and $\langle 110 \rangle$ directions. The formation of square-shaped nanoring can be attributed to the preferential perpendicular kinking behavior for cubic In_2O_3 (which is different from the ZGO case). The inner length of the square varies from 786 nm to 840 nm due to the tapering of the NW, which resulted from the un-catalyzed VS growth on the NW sidewall.²⁹ Here we focus on the structural analyses of the tip-backbone joint section, since we have already shown that the

kinking does not introduce any structural defects. An enlarged view of the tip-backbone joint section is shown in Figure 5.9c. The tip growth direction was redirected to $\langle 100 \rangle$ direction after being in contact with the backbone. The Au nanoparticle (diameter ~ 6 nm) verifies the VLS growth mechanism, as indicated by the arrow in Figure 5.9c. It should be noted that the tip successfully welded with the backbone and formed a closed single-crystalline nanoring structure. HRTEM images of the joint section are shown in Figure 5.9d and e. It can be clearly viewed that the tip and backbone exhibit the same atomic arrangements. More importantly, no structural defects, such as twin boundaries, were observed at the tip-backbone interface, which is a solid evidence for the formation of single-crystalline nanoring. The measured distance of 0.71 nm (Figure 5.9d and e) is consistent with the calculated spacing between adjacent (110) planes of cubic In_2O_3 .

5.3.4 Kinking Mechanisms

The kinking mechanism for the ZGO and In_2O_3 NWs are discussed below. According to previous extensive studies, NWs grown under stable conditions are usually straight without kinks, which means that the kinetic driving-force is negligible under those stable conditions.³⁰ However, the driving force for kink formation can be exaggerated by vapor perturbation,²⁷ which was shown to be an effective approach to introduce kinks in ZGO and In_2O_3 NWs (Figure 5.7 and 5.9). The formation processes of the single-crystalline kinked In_2O_3 NWs can be described as following (taken In_2O_3 NW as example): First, the straight In_2O_3 NWs deposited at high pressure (with Ar gas flow) grow preferentially along $\langle 100 \rangle$ directions, as have also been observed in previous reports.^{31,32} Then the Ar gas was stopped during perturbation. While the partial pressure of In vapor was essentially unchanged under constant evaporation temperature, the modulation of total pressure changes the mean free path of In vapor;²⁵ that is, the In vapor supply decreases with reduced total pressure, resulting in a lower

supersaturation value in the catalyst particle. Consequently, VS growth, a much slower growth process, dominates in the low pressure period due to the greatly reduced VLS growth rate. When Ar gas was re-introduced into the furnace, the supersaturation value in the catalyst particles would increase gradually. During this process, preferential nucleation at the three phase boundaries³³ gradually changes the catalyst orientation.²⁷ The NW would grow along another $\langle 100 \rangle$ or $\langle 110 \rangle$ direction when the supersaturation value resumes to its initial level before perturbation. Note that although $\langle 100 \rangle$ directions are the thermodynamically favorable growth directions for the NWs grown by our thermal evaporation method, the *metastable* $\langle 110 \rangle$ -oriented segments have been frequently observed in the kinked NWs (Figure 5.9). Very recently, it was also shown to be possible for NWs to grow along *metastable* directions although they are kinetically forced.³⁰ The NWs would follow the *metastable* direction until the accumulated driving force is large enough to induce kink formation.³⁰ Growth along metastable directions was also frequently observed in the kinked ZGO NWs (Figure 5.7). We would like to highlight that the preferential kinking behavior is highly material-dependent. For example, unlike the strictly perpendicular kinking observed for In_2O_3 NWs (Figure 5.9), erratic kinking behaviors without obvious trends were typically observed for the ternary ZGO NWs (Figure 5.7-8). Not only the kinking angles between straight segments showed large variations (Figure 5.7), randomly curved segments with “wormy” trajectories were also observed. However, the exact reasons of why ZGO NWs exhibited random kinking behaviors instead of growing along preferential directions are yet unclear and require further studies.

5.4 Branched ZGO-ZnO Heterostructures

5.4.1 Secondary Deposition Methods

A secondary growth process was carried out for ZnO branches growth on primary ZGO NWs. The as-grown ZGO NWs were used as substrates for branch growth without any treatment. Mixed ZnO and carbon powder (~0.5 g, molar ratio of 1:1) was used as source materials. Typically, the furnace temperature was increased to 1000 °C at a rate of 15 °C min⁻¹ and kept for 60 min. Ar gas mixed with 10 % O₂ (total pressure 2.2 mbar) was used as carrier gas for ZnO branch growth. The Si substrates with ZGO NWs on top were placed at different temperature regions to investigate the temperature dependent morphologies.

5.4.2 Epitaxial Growth of Aligned ZnO Nanorod Arrays

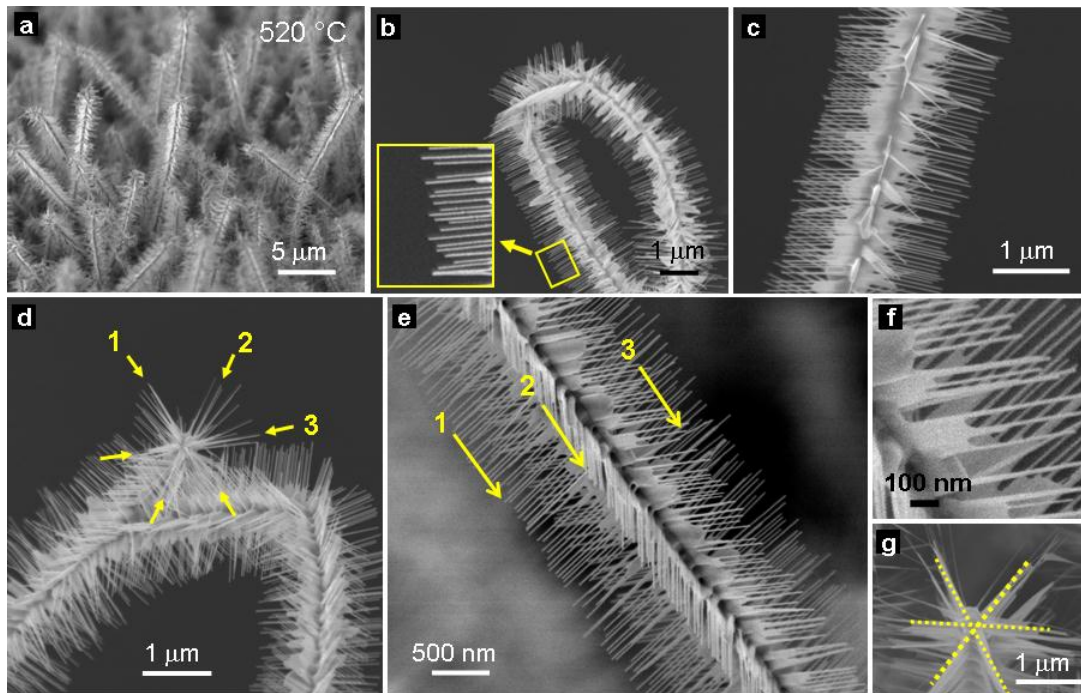


Figure 5. 10 SEM images of the branched NW heterostructures after a secondary ZnO branch growth at 520 °C. (a) Low magnification image. (b-e) High magnification images showing the well-aligned ZnO branches. The arrows and numbers in (d) and (e) indicate the 6-fold symmetry of the branches, as viewed from the (d) top and (e) side. (f) Enlarged view of the branches, showing the coalescence at the bottom. (g) View of 6-fold symmetry from the top, as indicated by dashed lines.

Thin ZnO NW branches were successfully grown on the primary ZGO NWs after a secondary vapor phase deposition process (Figure 5.10). The secondary growth was performed at ~520 °C, the optimum growth temperature as determined from the growth of

pure ZnO NWs in our system. The primary ZGO NWs were uniformly covered with thin ZnO branches (Figure 5.10a). Enlarged SEM images of the heterostructures were shown in Figure 5.10b-f. Well-aligned ZnO branches showed preferential growth directions, which were all perpendicular to the ZGO backbone NWs. 6-fold symmetry of the branches can be clearly identified from the top (Figure 5.10d and g) and side (Figure 5.10e) views. The arrows and numbers in Figure 5.10d and e indicate three of the six folds. The thin ZnO branches have uniform diameters ~ 20 nm. Lengths of the branches are in the range of 0.8-1.2 μm after 60 min growth. It is noteworthy that coalescence of the thin ZnO NWs can be observed at the bottom of the branches (Figure 5.10f). Moreover, it is expected that the lateral coalescence of the thin branches can be promoted under certain conditions, such as high growth temperature, leading to the growth of nanobelt branches (Figure 5.12). The results and mechanisms will be discussed later.

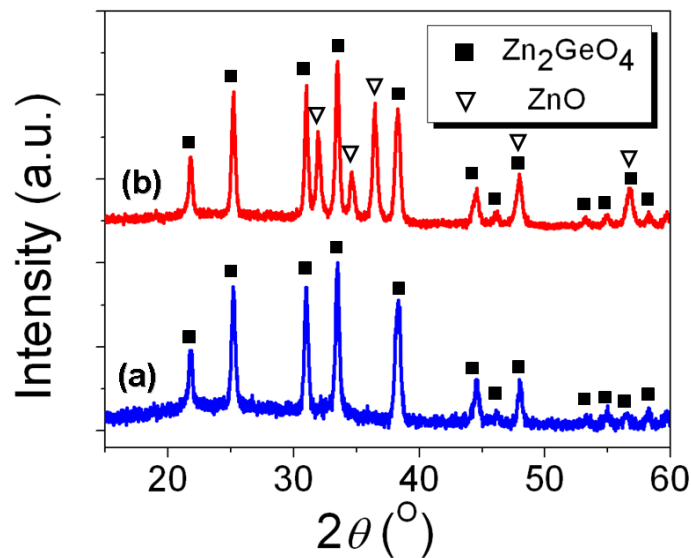


Figure 5. 11 XRD patterns of the nanostructures (a) before and (b) after secondary ZnO deposition. While a pure ZGO phase was detected before growth, an additional ZnO was detected after secondary deposition.

The crystal phases of the primary NWs (before secondary growth) and heterostructures (after secondary growth) were characterized using XRD (Figure 5.11). The primary NWs showed a pure ZGO phase (Figure 5.11a) with rhombohedral crystal structure. No other impurity peaks

were detected. After secondary growth, an additional ZnO phase with hexagonal crystal structure (JCPDS card 36-1451: $a = 5.2498 \text{ \AA}$, $c = 5.2066 \text{ \AA}$) was detected. The XRD results confirmed the successful ZnO deposition on the ZGO NWs. Together with the SEM observations before and after the secondary growth process, it is evident that the heterostructures are composed of ZGO backbones with ZnO branches.

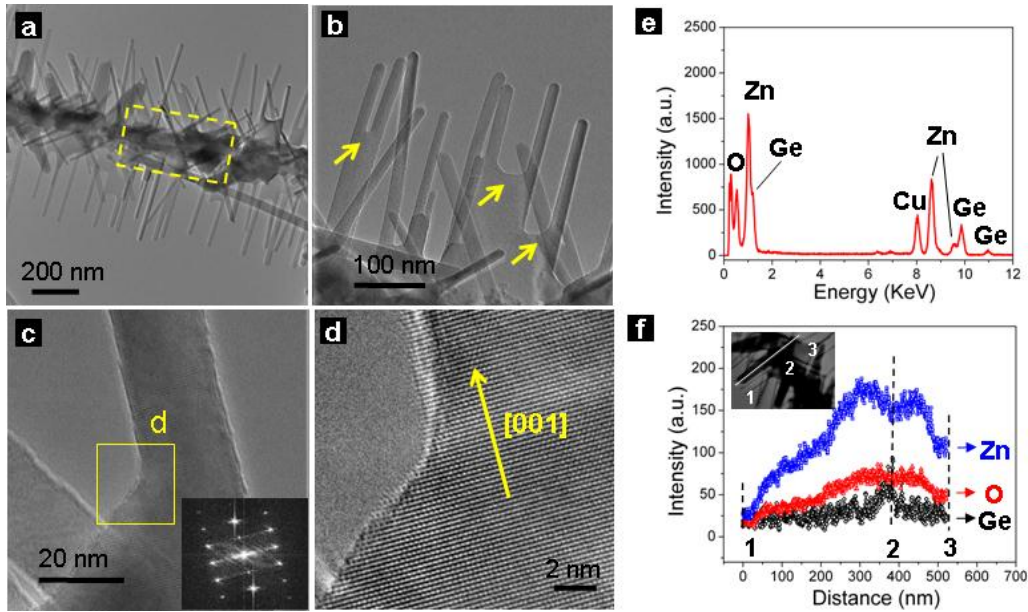


Figure 5. 12 (a) Low magnification TEM image of the branched heterostructures. (b) Enlarged view of the branches. Arrows indicate the coalescence between thin NWs. (c) Enlarged view of an individual ZnO branch, with its HRTEM image shown in (d). Inset in (c) is the corresponding FFT pattern. The ZnO branch NWs grow along [001] direction. (e) EDS spectrum recorded from the whole heterostructures in (a). (f) EDS line scanning profiles confirming the ZGO backbone NW with ZnO branches.

TEM and EDS analyses were performed to characterize the structure and composition of the branched heterostructures in more detail. Although the heterostructures were partially destroyed by ultra-sonication when preparing the TEM sample, the configuration of aligned branches on backbone NW can still be observed (Figure 5.12a). A typical enlarged view of the ZnO branches is shown in Figure 5.12b. Coalescence of the thin branches at the bottom can be clearly viewed (indicated by arrows in Figure 5.12b), which is consistent with the SEM results (Figure 5.12f). Since no metal catalysts were deposited on the primary NW surface before the secondary growth, and the branch growth fronts are free of catalyst

particles (Figure 5.12b), a VS mechanism could be adopted for the ZnO branch growth.^{34,35} Figure 5.12c is a high magnification TEM image of an individual ZnO branch with larger diameter at the bottom. HRTEM image (Figure 5.12d) reveals that the entire coalesced branch is single crystalline with no structure defects observed. Growth direction of the ZnO NWs was along *c*-axis of the hexagonal structure, a typical growth direction for ZnO NWs.³⁶ EDS spectrum taken from the whole heterostructures (including backbone NW and branches) is shown in Figure 5.12e, revealing the presence of Zn, Ge and O. Quantitative analysis showed that the atomic ratio of Zn/Ge was around 4/1. The Zn concentration is higher than the stoichiometric value for pure ZGO (2/1) due to the presence of ZnO branches. EDS line scanning was performed to further verify the elemental distributions (Figure 5.12f). The scanning path is indicated by a white line in STEM image (Figure 5.12f inset), with number '2' denoting the position of the backbone ZGO NW. The branch (from 1 to 2) is composed of Zn and O; and Ge can only be detected in the backbone NW (position 2). The elemental distribution in the line scanning profiles is consistent with XRD results, which showed ZnO growth on the ZGO primary NWs (Figure 5.11). Moreover, as indicated by the dashed square in Figure 5.12a, a ZnO shell was found depositing on the primary ZGO NW, similar to previous report.³⁵ EDS line scanning result (Figure 5.12f) with increasing Zn and O concentration around the ZGO NW also verifies the existence of the ZnO shell.

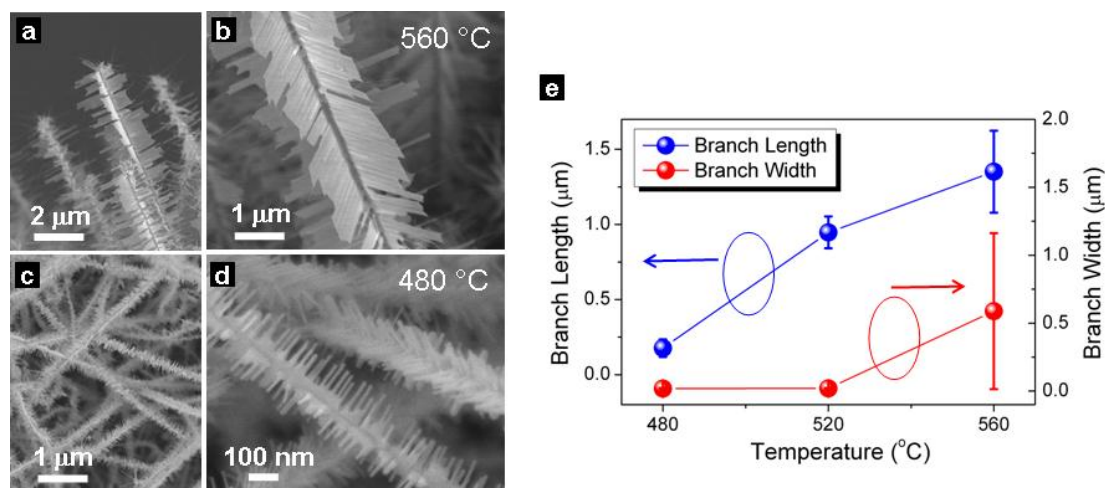


Figure 5. 13 SEM images showing the heterostructure morphologies grown at (a,b) 560 °C and (c,d) 480 °C. (e) Statistical results showing the branch lengths and branch widths as a function of growth temperature.

Previously, it was shown that lateral growth rate of the ZnO NWs was temperature dependent.^{37,38} Thus the secondary branch growth was performed at different temperature regions aiming to control the morphology of the heterostructures. Representative SEM images of the heterostructures grown at 560 °C and 480 °C are shown in Figure 5.13a-b and Figure 5.13c-d, respectively. The branches grown at high temperature (560 °C) showed severe lateral coalescence, forming belt-like or sheet-like branches. As can be clearly viewed, the lengths (~1.5 μm) and widths (as wide as 2.6 μm) for the branches grown at 560 °C are significantly larger than those grown at 480 °C (lengths ~120 nm, widths or diameters ~20 nm). Statistical results of the branch lengths and widths as a function of growth temperature is shown in Figure 5.13e. Both the branch lengths and widths showed increasing dependence with growth temperature. It is worth mentioning that the branches grown at 480 °C (Figure 5.13d) and 520 °C (Figure 5.10) showed uniform diameters in the range of 15-28 nm. However, the widths of the coalesced nanobelts exhibited much larger variations in the range of 60-2600 nm, resulting in the higher standard deviation value (Figure 5.13e). The heterostructures with well-defined geometry and high crystallinity show the possibility to control the morphology of nanostructures.

5.4.3 Detailed Mechanistic and Crystallographic Analyses

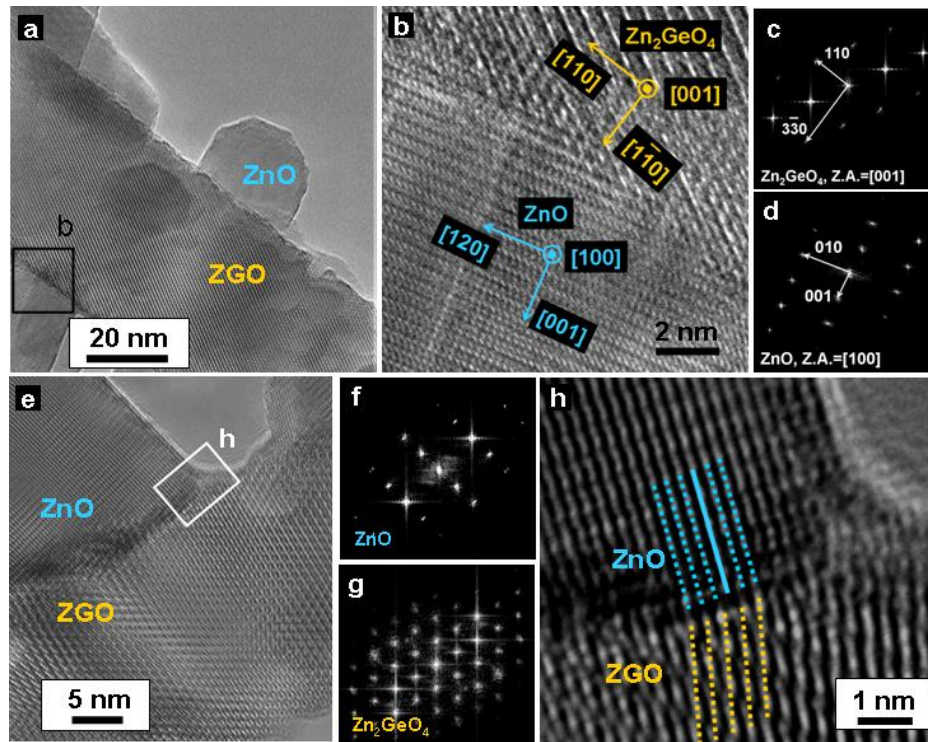


Figure 5. 14 (a) TEM image of a ZGO backbone with ZnO nuclei. (b-d) HRTEM image and corresponding FFT patterns of the interface. (e-g) TEM image and FFT patterns showing the consistent crystallographic relationship between ZGO and ZnO. (h) Structure defects such as misfit dislocations were observed at some of the ZGO-ZnO interface to release strain.

The formation of aligned ZnO branches is attributed to the epitaxial relationship with ZGO backbone NW. Previously, epitaxial growth of ZnO (hexagonal structure) on various materials was reported. Especially, epitaxial growth was achieved with those materials with different crystal structures and large lattice mismatches, such as Ge (cubic structure),³⁹ Ga₂O₃ (monoclinic structure)³⁴ and In₂O₃ (cubic structure).⁴⁰ In our case, the ZGO NWs exhibit similar crystal structure (rhombohedral structure) with ZnO and epitaxial growth can be readily expected. A low magnification TEM image of short ZnO branches grown perpendicularly on a ZGO backbone is shown in Figure 5.14a. Note that the angle between the branch and backbone deviates slightly from 90 ° owing to the specific 3D orientations.²⁰ HRTEM images of the ZGO-ZnO interface revealing the detailed crystal structures are shown in Figure 5.14b and e. It is evident that the ZGO-ZnO interface is free of, for example,

amorphous sheath-layer. And the extension of clear lattice fringes from the ZGO backbone to ZnO branch reveals a crystalline interface, *i.e.*, epitaxial growth. Fast Fourier transforms (FFT) of the ZGO and ZnO parts are shown in Figure 5.14c and d, respectively. The patterns can be indexed as the diffractions along the [001] axis of ZGO and [100] axis of ZnO, respectively. The growth directions of the ZGO backbone and ZnO branch are along [110] and [001], respectively. The crystallographic orientations of the heterostructure are shown in Figure 5.15. It should be noted that in hexagonal structure of ZnO, the crystal direction normal to the (010) face is [120]. According to the FFT indices, an epitaxial relationship between the (001) face of ZnO and (1-10) face of ZGO exists, as schematically shown in Figure 5.15b. Unlike the homoepitaxial growth where the branches follow the same crystallography of the backbone,²⁰ the ZnO does not follow the [1-10] direction normal to the ZGO side-facet. The [001] branch growth direction can be attributed to the strong tendency of ZnO to grow in the *c* direction.³⁴ Analogous to the well-known sapphire *a*-(110) plane,^{36,41} the ZGO (1-10) plane is a rectangular lattice with small lattice mismatches with the ZnO hexagonal (001) plane. The lattice mismatch between 3[100] of ZnO ($3 \times 5.2498 = 9.749 \text{ \AA}$) and [001] of ZGO (9.53 \AA) is 2.3%, and the mismatch along [120] direction of ZnO is only 1.1%. The small lattice mismatch is considered to be the main driving force of epitaxial growth in the process of minimizing the interfacial strain energy.

Structure defects such as misfit dislocations were observed at some of the ZGO-ZnO interfaces to relax strain and reduce the interfacial elastic energy. The dislocation formation was widely reported for crystal growth in lattice-mismatched systems.^{42,43} As a typical example, HRTEM image of a short ZnO branch grown on ZGO NW is shown in Figure 5.14e. Growth directions of the ZnO and ZGO are along [001] and [110], respectively, consistent with those shown in Figure 5.14b. Enlarged view of the interface region (marked by square in

Figure 5.14e) with misfit dislocations is shown in Figure 5.14h (indicated by dashed lines). The spacing for 5(010) of ZnO ($5 \times 0.28 = 1.40$ nm) is almost the same with 2(110) of ZGO ($2 \times 0.71 = 1.42$ nm), as shown in Figure 5.14h [note that the distance between dashed yellow lines is half of the spacing between ZGO (110) planes].

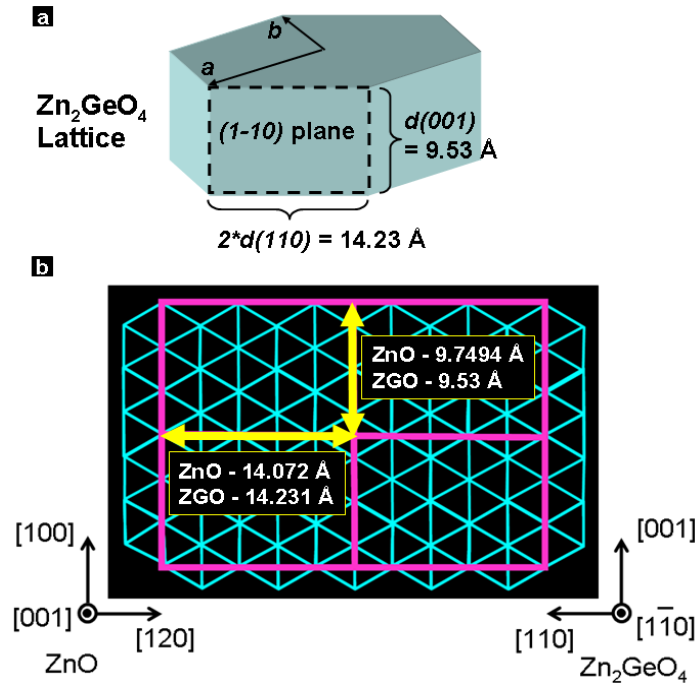


Figure 5. 15 Schematic models of (a) hexagonal ZGO lattice and (b) the epitaxial relationship between (001) surface of ZnO and (1-10) surface of ZGO. The red rectangles show the lattices of ZGO (1-10) plane.

Based on the above analyses, the detailed growth mechanism of the branched heterostructures is described as following: During secondary vapor deposition, Zn vapor was generated at the high temperature region through carbothermal reactions. Instead of the direct gas convey in conventional process,⁴⁴ the Zn vapor would diffuse to the lower temperature region in a more stable manner due to the usage of double-tube system. ZGO NWs on top of Si substrates were located at the low temperature region (400-500 °C). The primary ZGO NW surface is atomically rough and, thus, is energetically favorable nucleation sites for ZnO.^{34,45} At the initial growth stage, sparsely distributed ZnO nuclei are first deposited on the NW surface. The ZnO nuclei would preferentially elongate along [001] direction due to the strong

tendency of *c*-axial growth. Driven by the epitaxial growth between ZnO *c*-plane and ZGO side-faces, the ZnO branches showed perpendicular growth directions to the ZGO backbones. Meanwhile, apart from the longitude growth of ZnO branches, continuous ZnO deposition also resulted in the formation of thin ZnO shells surrounding the ZGO core, as evidenced in Figure 5.12a. Simultaneous growth of ZnO in all directions (longitude branch elongation and radial shell formation) was also reported previously.³⁴ Finally, ZGO NW heterostructures with ZnO shells and aligned branches were developed after growth of ~60 min. Symmetry of the ZnO branches is determined by the cross-sectional shapes of the backbone NWs.^{34,35} The ZGO NWs grown along [110] direction⁴⁵ are likely enclosed by $\pm(1-10)$, $\pm(001)$ and $\pm(1-11)$ faces and exhibit quasi-hexagonal cross-sections. Thus the ZnO branches are expected to show 6-fold symmetry, as observed in Figure 5.10d, e and g. It is also possible that structures with 2- or 4-fold symmetries may be formed as intermediate products.^{34,40} However, they tend to convert into 6-fold which is the ideally symmetrical structure,³⁴ and thus, only 6-fold symmetrical heterostructures can be observed after growth.

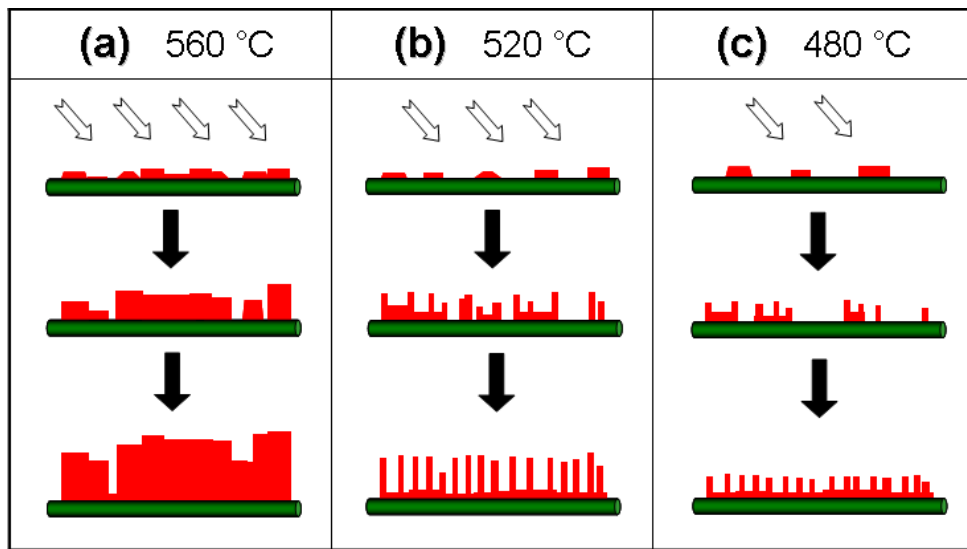


Figure 5. 16 Schematic illustration of structure evolution of the branches (red color) under different growth temperatures. The temperature dependent nucleation rates and lateral growth rates lead to the formation of distinct nanobelt and NW branches.

The temperature dependent branch morphologies can be mainly attributed to several reasons. First, the ZnO nucleation density increases with temperature. The Zn vapor was generated at the central high temperature region (1000 °C). Thus, a highest Zn vapor concentration existed at 1000 °C and the concentration gradually decreased towards the lower temperature region (downstream). The vapor diffusion induced by this concentration gradient would result in a higher Zn vapor concentration at 560 °C, with the lowest concentration at 480 °C (indicated by the number of hollow arrows in Figure 5.16). A fast and dense ZnO nuclei deposition on the primary ZGO NW can be expected due to the higher vapor concentration at 560 °C. The dense nuclei which are in close vicinity to each other would coalesce more easily compared with the relatively sparse nuclei at the lower temperature region (Figure 5.16). While the thickness of the branches is restricted by the diameter of the backbone NW,³⁵ elongation of the coalesced nuclei with larger widths results in the formation of nanobelt branches (Figure 5.16a). Second, the higher lateral growth rate of the branches at higher temperature also contributes to the formation of belt-like morphology. Previous research work showed that the two dimensional (2D) nucleation probability increases with temperature.^{37,38} Many reports also revealed that high temperature promotes the formation of nanobelt structures instead of thin NWs.^{37,46} Here the higher lateral expansion rate of the branches grown at 560 °C would lead to the formation of severely coalesced nanobelts with larger widths. Third, the longitude growth rate of the NWs increases with both growth temperature and vapor concentration.⁴⁷ As mentioned above, the Zn concentration at 560 °C is higher than those at 520 °C and 480 °C due to the vapor diffusion. Both aspects (high growth temperature and vapor concentration) would promote the longitude growth rate of the branches.

5.5 ZGO NW Networks for Selective Deep-UV Photodetection

5.5.1 Device Fabrication Methods

For device fabrication, standard optical-lithography followed by Cr/Au (10/50 nm) deposition and liftoff was used to define the contact electrodes. The ZGO NWs were suspended in ethanol by sonication (~10 s) and then dispersed on top of the electrodes. UV photoresponse of the devices was characterized by Keithley semiconductor parameter analyzer using a portable UV lamp (254 nm and 365 nm). All the measurements were performed at room temperature in ambient conditions.

5.5.2 Network Devices with Fast Response Time and High Wavelength Selectivity

Wide-bandgap semiconductor NWs have been widely used as building blocks for nanoscale UV photodetectors.⁴⁸⁻⁵⁰ Compared with their bulk or thin film counterparts, the nanostructures are expected to exhibit high photosensitivity due to their high surface-to-volume ratios. To date, extensive research has been carried out into binary wide-bandgap materials for UV detection, such as ZnO,⁵⁰ SnO₂,⁴⁹ ZnS⁵¹ and GaN.⁵² However, much less attention has been paid to more complex materials (such as ternary oxides), probably due to the difficulty in obtaining high quality ternary NWs.^{53,54} Ternary oxide NWs are chemically and thermally stable, and are superior for deep UV detection due to their larger bandgap and hence higher wavelength selectivity. For example, ZnO ($E_g=5.4$ eV) responds to the whole UV band (~200-400 nm), but ZGO ($E_g=5.68$ eV) is expected to be UV-A/B (~290-400 nm) blind and only responsive to UV-C band (~200-290 nm).⁵¹ Here, we demonstrate the optoelectronic property studies of ZGO NW network UV photodetectors. Instead of individual NW, the networks are of interest for photodetector fabrication since they yield

sufficiently good or even better device performances but only require facile and low-cost lithography techniques.^{55,56}

Although impurity phases were usually detected in the vapor phase deposition of ternary oxide NWs,^{54,57} no impurity phases such as Ge, ZnO or GeO₂ were detected in our samples (via a controlled ZnO/GeO₂ molar ratio in the source materials). The high purity ZGO NWs eliminate the concern that the UV photoresponse may originate from the impurities, such as Ge or ZnO NWs. In contrast to the previously reported short and agglomerated ZGO nanorods obtained by hydrothermal method,⁵ much longer ZGO NWs can be readily obtained by VLS growth method. The lengths are time-dependent and typically exceed 10 μm for a growth period of 60 min. The high aspect ratio facilitates the photodetector fabrication by connecting the electrodes or forming inter-connected NW networks.

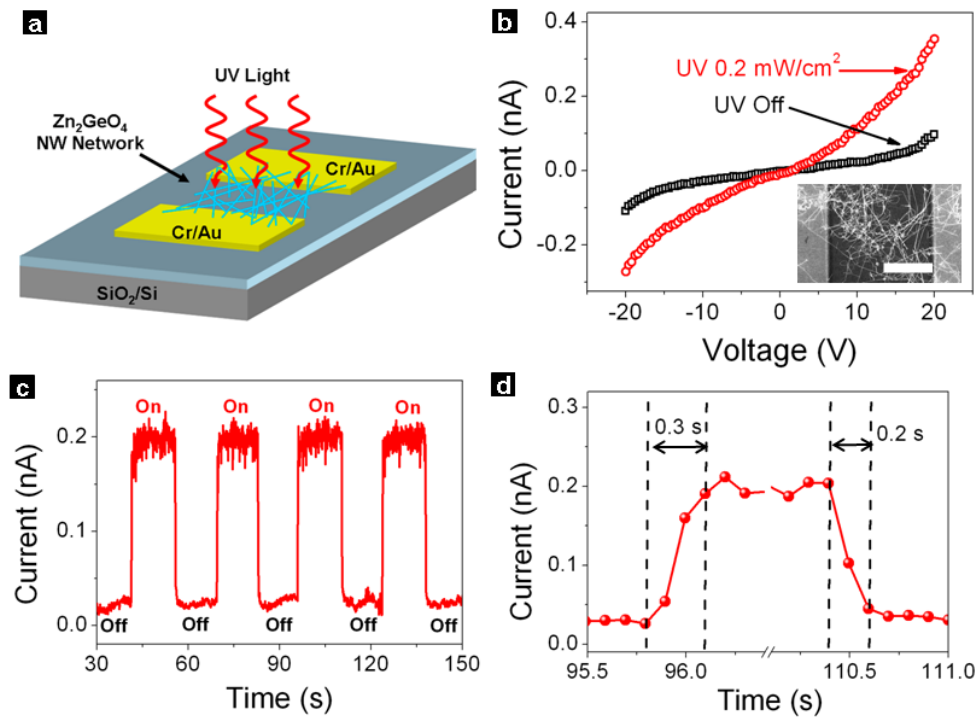


Figure 5. (a) Schematic diagram of the UV photodetector using ZGO NW networks. (b) I-V characteristics of the device in dark (black squares) and upon 0.2 mW/cm² (red circles) 254 nm UV illumination. Inset is a typical SEM image of the NW network between electrodes. Scale bar is 5 μm . (c) Photoresponse characteristics showing the reversible switching behavior when the 0.2 mW/cm² 254 nm UV light is turned on and off repeatedly. (d) Enlarged view of a single on/off cycle showing the fast response and reset time within 1 s.

The metal-semiconductor-metal (MSM) photodetector structure is depicted in Figure 5.17a. The ZGO NW networks are dispersed between the pre-patterned Cr/Au electrodes. *I-V* characteristics of the photodetectors measured in dark and under 0.2 mW/cm² 254 nm UV illumination are depicted in Figure 5.17b. The *I-V* curves were measured with bias from -20 V to 20 V at room temperature in ambient condition. For a fixed bias of 20 V, the current of the NW network increases from 0.09 nA (black square) to 0.35 nA (red circle) when the UV light is turned on. The quasi-linear curves indicate that the contact resistance does not contribute significantly when compared with the resistance of the NW network, which is expected to be highly resistant due to the large bandgap (thus extremely low carrier density) and NW-NW junction barriers (details will be discussed below).^{54,58} The photoresponse behavior of the device was characterized by measuring the current as a function of time when the 254 nm UV light was periodically turned on and off, as shown in Figure 5.17c. The measurement bias was fixed at 20 V with UV light intensity at ~0.2 mW/cm². A fully reversible switching behavior was observed. The current increased from ~0.02 nA to ~0.2 nA upon UV illumination, which is an enhancement of about 10-fold. It is worth noting that the ZGO NW photodetector exhibited fast response and recovery times within 1 s. An enlarged view of a typical on/off cycle is shown in Figure 5.17d. The measured response and recovery time are 0.3 s and 0.2 s, respectively. Similar fast response and reset times (<1 s) were observed for all the devices (15 devices measured).

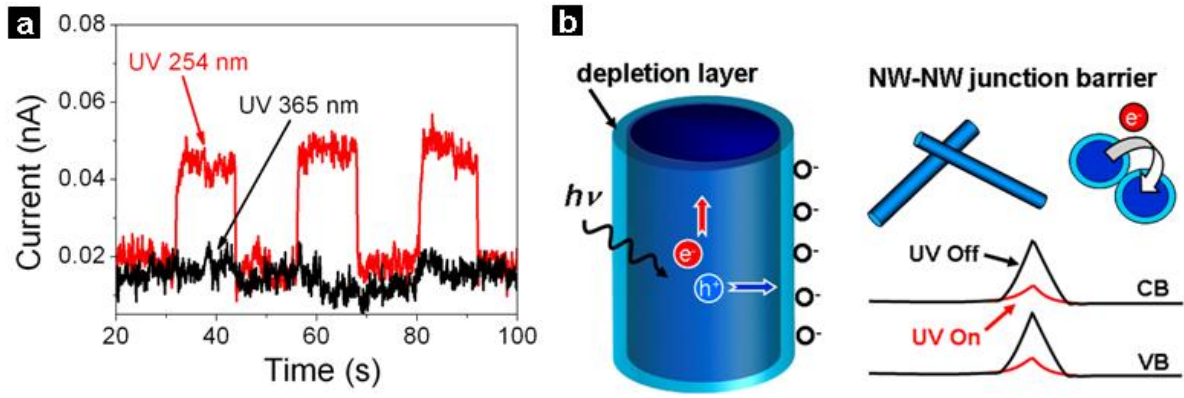


Figure 5. 18 (a) Photoresponse behavior of the device under UV illumination of 254 nm (red line) and 365 nm (black line). (b) Schematic of the carrier generation and NW-NW junction barrier for electron transfer in the network device.

The wavelength selectivity of the ZGO network devices in UV spectrum was demonstrated using the available 254 nm and 365 nm UV light. The photoresponse characteristics are shown in Figure 5.18a. The current shows no observable change upon 365 nm UV illumination (black curve), in contrast to the abrupt increase when exposed to 254 nm UV light (red curve). The photon energies of 254 nm UV light (5.88 eV) are high enough to generate electron-hole pairs [$h\nu \rightarrow e^- + h^+$] in the ZGO NWs ($E_g = 5.68$ eV). However, the increase in carrier density is negligible when exposed to 365 nm UV light with sub-bandgap photon energies of 5.4 eV and no current increase can be observed. This observation reveals that the ZGO NWs exhibit high wavelength selectivity in the UV-C region, when compared with those extensively investigated binary oxides, such as ZnO and SnO₂.^{49,50}

Schematic diagram depicting the carrier generation and transportation processes in the network devices are shown in Figure 5.18b. The UV response and recovery are known to be associated with the oxygen adsorption and desorption processes.^{48-50,59} In ambient conditions, oxygen molecules would adsorb on the NW surface by capturing free electrons through $O_2(g) + e^- \rightarrow O_2^-(ad)$, creating a surface depletion layer with low conductivity [Fig. 4(b)]. Adsorbed oxygen ions would be discharged by the photon-generated holes through O_2^-

$(ad)+h^+\rightarrow O_2(g)$, resulting in a reduction of the depletion barrier thickness. Both the increase of carrier density and oxygen desorption contributes to the conductance increase of the NW networks.

Previously, it has been shown that the resistance of two crossed NWs was dominated by the NW-NW junction barrier, instead of the resistances of the NW themselves.^{14,15} As have been demonstrated in Ge NW photodetectors, the electrons have to overcome the NW-NW junction barrier when tunneling from one NW to another (Figure 5.18b). The electron-transfer barrier originates from the surface depletion layers. The depletion layer can be narrowed by UV illumination due to the increased carrier density, which is equivalent to a lowering of the effective barrier height. It is thus easier for electrons to go through the networks upon UV illumination and therefore resulting in the increase of current (Figure 5.17).

In contrast to the previously reported slow response and recovery time,^{3,8,16,17} the fast recovery time (<1 s) for our ZGO NW photodetectors can be attributed to the NW-NW junction barrier dominated conductance. Typically, the NW conductance is still higher than its initial value within a short period upon turning off the UV light, since the oxygen diffusion and re-adsorption to deplete the NW channel is a slow process.^{8,16,17} The dominate role of the junction barrier would lead to a current decay almost approaching its initial value within a short period (<1 s for our devices). The light induced barrier height modulation is typically much faster than the oxygen diffusion process (on the order of several minutes or hours). For example, it was shown previously that the photocurrent response time for bulk Au-CdS Schottky barrier was typically below 1 s.¹⁸ Very recently, it was also reported that the recovery time of ZnO NW UV-sensors could be improved by FIB deposited contacts with

Schottky barriers.⁸ In this work, we suggest that the response and recovery time can be enhanced by using NW networks with NW-NW barrier dominated conductance. No intense and expensive lithography processes are required and the single optical-lithography step also allows potential large-scale device fabrication.

We would like to compare our work with other reports on ternary oxide photodetectors. Feng *et al.* reported the usage of individual ZnGa_2O_4 NW for UV sensing.⁶⁰ Single ZnGa_2O_4 NW was dispersed on top of Au electrodes and tested without further treatment. Large Schottky barriers were observed for the NW devices.⁶⁰ Fast response time (~ 2 s) and reset time (< 1 s) were observed.⁶⁰ The conduction mechanism is similar to the previous report on ZnO NW photodetector⁶¹ with FIB deposited Schottky contacts, where fast response time was also observed. Xue *et al.* reported the UV sensing properties of individual ZnSnO_3 NW devices.⁶² Barrier dominated conductance (including both Schottky barrier and conduction barrier between NW layers)⁶² were observed in electrical property measurements, however, a slow current decay process (> 2000 s) were observed in UV sensing measurements. Our network devices is advantageous than those single-NW devices in several aspects. The probability of obtaining single-NW devices by randomly dispersing NW solutions on prepatterned electrodes is much lower than that of network devices. Moreover, the randomly dispersed single-NW devices did not show stable and consistent performances. For example, with similar fabrication procedures and conduction mechanisms, ZnGa_2O_4 NW device showed fast reset time but the reset time for ZnSnO_3 NW devices was > 1000 times slower. Also, the NWs deposited on top of the electrodes without any further treatments are prone to peeling off from the substrates. Instead, network devices are stable and exhibited consistently fast photoresponse rate in our studies.

5.6 Conclusions

In conclusion, we have presented the synthesis and characterization of high quality ZGO NWs and their corresponding superstructures (kinked NWs and nanorings) and heterostructures (branched ZGO-ZnO NWs). ZGO NW networks were used as efficient detection channels for selective deep-UV detection with fast response and reset time.

ZGO NWs were grown via a facile Au-catalyzed VLS mechanism. Detailed characterizations of the NW morphology, crystal structure and compositions were presented. The high purity NWs with high aspect ratios allows easy fabrication of electronic devices. Branched ZGO NWs were simultaneously grown with the straight NWs and a sequential seeding mechanism was proposed to account for their formation. Kinked NWs were formed by *in situ* tuning the pressure inside the growth chamber. The variation of supersaturation in the catalyst particles together with the preferential nucleation behavior at the three phase boundaries changed the NW growth directions and finally resulted in kinked superstructures. However, the entire kinked NWs remain single-crystalline without structural defects. The pressure induced kinking formation can be readily extended to other groups of materials, as have also been demonstrated on In_2O_3 .

Branched ZGO-ZnO heterostructures were synthesized by a secondary deposition method, where aligned ZnO nanorods were grown on the ZGO NW stems. The single-crystalline ZGO NWs served as excellent lattice-matched substrates for the growth of aligned ZnO nanorods, which were also confirmed by theoretical analyses of the lattice mismatches. Morphology of the ZnO branches can be efficiently tuned by changing the growth temperature. Both the branch lengths and widths increases with growth temperature, which were attributed to the high nucleation density, faster lateral and longitude growth rates at high temperature region.

ZGO NW network photodetectors were fabricated. The network devices exhibited excellent photodetector performances with fast photoresponse time and high wavelength selectivity. Typically, the response and reset time of the network devices was <1 s, which were attributed to the unique junction-dominated conductance of network devices. The wide bandgap of ZGO NWs (4.68 eV, corresponds to a cutoff wavelength of 265 nm) make them superior candidates for the selective detection of deep-UV light. As has been demonstrated, the NW photodetectors responded to 254 nm UV light but not to 365 nm UV light. The novel ZGO NW network devices allow potential large scale fabrication and may act as cost-effective photodetectors with high performances.

References

- (1) Lewis, J. S.; Holloway, P. H. *Journal of the Electrochemical Society* **2000**, *147*, 3148-3150.
- (2) Liu, Z. S.; Jing, X. P.; Wang, L. X. *Journal of the Electrochemical Society* **2007**, *154*, H500-H506.
- (3) Bender, J. P.; Wager, J. F.; Kissick, J.; Clark, B. L.; Keszler, D. A. *Journal of Luminescence* **2002**, *99*, 311-324.
- (4) Sato, J.; Kobayashi, H.; Ikarashi, K.; Saito, N.; Nishiyama, H.; Inoue, Y. *Journal of Physical Chemistry B* **2004**, *108*, 4369-4375.
- (5) Huang, J. H.; Wang, X. C.; Hou, Y. D.; Chen, X. F.; Wu, L.; Fu, X. Z. *Environmental Science & Technology* **2008**, *42*, 7387-7391.
- (6) Tsai, M. Y.; Yu, C. Y.; Wang, C. C.; Perng, T. P. *Crystal Growth & Design* **2008**, *8*, 2264-2269.
- (7) Jung, Y.; Lee, S. H.; Ko, D. K.; Agarwal, R. *Journal of the American Chemical Society* **2006**, *128*, 14026-14027.
- (8) Peng, H. L.; Schoen, D. T.; Meister, S.; Zhang, X. F.; Cui, Y. *Journal of the American Chemical Society* **2007**, *129*, 34-35.
- (9) Wang, Z. L. *Materials Science & Engineering R-Reports* **2009**, *64*, 33-71.
- (10) Geng, C. Y.; Jiang, Y.; Yao, Y.; Meng, X. M.; Zapien, J. A.; Lee, C. S.; Lifshitz, Y.; Lee, S. T. *Advanced Functional Materials* **2004**, *14*, 589-594.
- (11) Brent A. Wacaser, K. A. D., Jonas Johansson, Magnus T. Borgström, Knut Deppert, Lars Samuelson *Advanced Materials* **2009**, *21*, 153-165.
- (12) Mensah, S. L.; Kayastha, V. K.; Yap, Y. K. *Journal of Physical Chemistry C* **2007**, *111*, 16092-16095.
- (13) Wanger, R. S.; Ellis, W. C. *Applied Physics Letters* **1964**, *4*, 89-90.
- (14) Kodambaka, S.; Tersoff, J.; Reuter, M. C.; Ross, F. M. *Science* **2007**, *316*, 729-732.
- (15) Schmidt, V.; Gosele, U. *Science* **2007**, *316*, 698-699.

- (16) Yang, P. D.; Yan, H. Q.; Mao, S.; Russo, R.; Johnson, J.; Saykally, R.; Morris, N.; Pham, J.; He, R. R.; Choi, H. J. *Advanced Functional Materials* **2002**, *12*, 323-331.
- (17) Yan, C. Y.; Lee, P. S. *Journal of Physical Chemistry C* **2009**, *113*, 14135-14139.
- (18) Wu, J.; Punchaipetch, P.; Wallace, R. M.; Coffey, J. L. *Advanced Materials* **2004**, *16*, 1444-+.
- (19) Dick, K. A.; Deppert, K.; Larsson, M. W.; Martensson, T.; Seifert, W.; Wallenberg, L. R.; Samuelson, L. *Nature Materials* **2004**, *3*, 380-384.
- (20) Wang, D.; Qian, F.; Yang, C.; Zhong, Z. H.; Lieber, C. M. *Nano Letters* **2004**, *4*, 871-874.
- (21) Hannon, J. B.; Kodambaka, S.; Ross, F. M.; Tromp, R. M. *Nature* **2006**, *440*, 69-71.
- (22) Kodambaka, S.; Hannon, J. B.; Tromp, R. M.; Ross, F. M. *Nano Letters* **2006**, *6*, 1292-1296.
- (23) Doerk, G. S.; Ferralis, N.; Carraro, C.; Maboudian, R. *Journal of Materials Chemistry* **2008**, *18*, 5376-5381.
- (24) den Hertog, M. I.; Rouviere, J. L.; Dhalluin, F.; Desre, P. J.; Gentile, P.; Ferret, P.; Oehler, F.; Baron, T. *Nano Letters* **2008**, *8*, 1544-1550.
- (25) Kawashima, T.; Mizutani, T.; Nakagawa, T.; Torii, H.; Saitoh, T.; Komori, K.; Fujii, M. *Nano Letters* **2008**, *8*, 362-368.
- (26) Gao, P. X.; Wang, Z. L. *Journal of Physical Chemistry B* **2002**, *106*, 12653-12658.
- (27) Tian, B. Z.; Xie, P.; Kempa, T. J.; Bell, D. C.; Lieber, C. M. *Nat. Nanotechnol.* **2009**, *4*, 824-829.
- (28) Hughes, W. L.; Wang, Z. L. *Journal of the American Chemical Society* **2004**, *126*, 6703-6709.
- (29) Vomiero, A.; Ferroni, M.; Comini, E.; Faglia, G.; Sberveglieri, G. *Crystal Growth & Design*, *10*, 140-145.
- (30) Madras, P.; Dailey, E.; Drucker, J. *Nano Letters* **2009**, *9*, 3826-3830.
- (31) Wan, Q.; Dattoli, E. N.; Fung, W. Y.; Guo, W.; Chen, Y. B.; Pan, X. Q.; Lu, W. *Nano Letters* **2006**, *6*, 2909-2915.
- (32) Wan, Q.; Wei, M.; Zhi, D.; MacManus-Driscoll, J. L.; Blamire, M. G. *Advanced Materials* **2006**, *18*, 234-+.
- (33) Wacaser, B. A.; Dick, K. A.; Johansson, J.; Borgstrom, M. T.; Deppert, K.; Samuelson, L. *Advanced Materials* **2009**, *21*, 153-165.
- (34) Mazeina, L.; Picard, Y. N.; Prokes, S. M. *Crystal Growth & Design* **2009**, *9*, 1164-1169.
- (35) Bae, S. Y.; Seo, H. W.; Choi, H. C.; Park, J. *Journal of Physical Chemistry B* **2004**, *108*, 12318-12326.
- (36) Huang, M. H.; Mao, S.; Feick, H.; Yan, H. Q.; Wu, Y. Y.; Kind, H.; Weber, E.; Russo, R.; Yang, P. D. *Science* **2001**, *292*, 1897-1899.
- (37) Yan, C. Y.; Singh, N.; Lee, P. S. *Crystal Growth & Design* **2009**, **,.
- (38) Dai, Z. R.; Pan, Z. W.; Wang, Z. L. *Advanced Functional Materials* **2003**, *13*, 9-24.
- (39) Yin, L. W.; Li, M. S.; Bando, Y.; Golberg, D.; Yuan, X. L.; Sekiguchi, T. *Advanced Functional Materials* **2007**, *17*, 270-276.
- (40) Lao, J. Y.; Wen, J. G.; Ren, Z. F. *Nano Letters* **2002**, *2*, 1287-1291.
- (41) Wang, X. D.; Song, J. H.; Wang, Z. L. *Journal of Materials Chemistry* **2007**, *17*, 711-720.
- (42) Nikoobakht, B.; Eustis, S.; Herzing, A. *Journal of Physical Chemistry C* **2009**, *113*, 7031-7037.
- (43) Vandermerwe, J. H.; Bauer, E. *Physical Review B* **1989**, *39*, 3632-3641.
- (44) Wang, Q.; Li, G. D.; Liu, Y. L.; Xu, S.; Wang, K. J.; Chen, J. S. *Journal of Physical Chemistry C* **2007**, *111*, 12926-12932.
- (45) Yan, C. Y.; Lee, P. S. *Journal of Physical Chemistry C* **2009**, DOI: 10.1021/jp9050879.
- (46) Gao, T.; Wang, T. H. *Journal of Physical Chemistry B* **2004**, *108*, 20045-20049.
- (47) Kodambaka, S.; Tersoff, J.; Reuter, M. C.; Ross, F. M. *Physical Review Letters* **2006**, *96*, 096105.

- (48) Kind, H.; Yan, H. Q.; Messer, B.; Law, M.; Yang, P. D. *Advanced Materials* **2002**, *14*, 158-+.
- (49) Liu, Z. Q.; Zhang, D. H.; Han, S.; Li, C.; Tang, T.; Jin, W.; Liu, X. L.; Lei, B.; Zhou, C. W. *Advanced Materials* **2003**, *15*, 1754-+.
- (50) Soci, C.; Zhang, A.; Xiang, B.; Dayeh, S. A.; Aplin, D. P. R.; Park, J.; Bao, X. Y.; Lo, Y. H.; Wang, D. *Nano Letters* **2007**, *7*, 1003-1009.
- (51) Fang, X. S.; Bando, Y.; Liao, M. Y.; Gautam, U. K.; Zhi, C. Y.; Dierre, B.; Liu, B. D.; Zhai, T. Y.; Sekiguchi, T.; Koide, Y.; Golberg, D. *Advanced Materials* **2009**, *21*, 2034-2039.
- (52) Han, S.; Jin, W.; Zhang, D. H.; Tang, T.; Li, C.; Liu, X. L.; Liu, Z. Q.; Lei, B.; Zhou, C. W. *Chemical Physics Letters* **2004**, *389*, 176-180.
- (53) Fan, H. J.; Yang, Y.; Zacharias, M. *Journal of Materials Chemistry* **2009**, *19*, 885-900.
- (54) Feng, P.; Zhang, J. Y.; Wan, Q.; Wang, T. H. *Journal of Applied Physics* **2007**, *102*.
- (55) Unalan, H. E.; Zhang, Y.; Hiralal, P.; Dalal, S.; Chu, D. P.; Eda, G.; Teo, K. B. K.; Chhowalla, M.; Milne, W. I.; Amaratunga, G. A. J. *Applied Physics Letters* **2009**, *94*.
- (56) Cao, Q.; Kim, H. S.; Pimparkar, N.; Kulkarni, J. P.; Wang, C. J.; Shim, M.; Roy, K.; Alam, M. A.; Rogers, J. A. *Nature* **2008**, *454*, 495-U4.
- (57) Jie, J. S.; Wang, G. Z.; Han, X. H.; Fang, J. P.; Yu, Q. X.; Liao, Y.; Xu, B.; Wang, Q. T.; Hou, J. G. *Journal of Physical Chemistry B* **2004**, *108*, 8249-8253.
- (58) Duan, X. F.; Huang, Y.; Cui, Y.; Wang, J. F.; Lieber, C. M. *Nature* **2001**, *409*, 66-69.
- (59) Zhou, J.; Gu, Y. D.; Hu, Y. F.; Mai, W. J.; Yeh, P. H.; Bao, G.; Sood, A. K.; Polla, D. L.; Wang, Z. L. *Applied Physics Letters* **2009**, *94*.
- (60) Feng, P.; Zhang, J. Y.; Wan, Q.; Wang, T. H. *Journal of Applied Physics* **2007**, *102*, 074309.
- (61) Zhou, J.; Gu, Y. D.; Hu, Y. F.; Mai, W. J.; Yeh, P. H.; Bao, G.; Sood, A. K.; Polla, D. L.; Wang, Z. L. *Applied Physics Letters* **2009**, *94*, 191103.
- (62) Xue, X. Y.; Chen, Y. J.; Li, Q. H.; Wang, C.; Wang, Y. G.; Wang, T. H. *Applied Physics Letters* **2006**, *88*, 182102.

CHAPTER 6 Morphology Controlled Synthesis of $\text{In}_2\text{Ge}_2\text{O}_7$ (IGO) Nanostructures for Solar-Blind Photodetection

6.1 Objective

Investigation on ternary complex oxide nanomaterials is one of the emerging areas. Compared with elemental or binary materials, studies on ternary materials are much less and only limited reports can be found on the synthesis and property investigations of ternary oxide nanostructures, probably due to the difficulty of synthetic control. To properly control the morphology and stoichiometric compositions of ternary oxides is more difficult due to the existence of elemental or binary impurities. Further efforts are needed to achieve proper control over the nanostructures growth process and obtain desired morphologies for specific nanodevice applications.

Indium germanate ($\text{In}_2\text{Ge}_2\text{O}_7$, IGO) is a typical Ge-based complex ternary material and have received little attention previously. IGO is a wide bandgap semiconductor with a large bandgap of 4.43 eV. This novel ternary oxide exhibited interesting optical and electronic properties which may potentially be used in many areas, such as solid state light sourcing, chemical and light sensors. However, knowledge on the synthesis and properties of IGO nanostructures are far from sufficient. In this chapter, we will present our studies on the morphology control and device applications of IGO nanostructures.

Previously, several types of IGO nanostructures have been reported, including microtubes¹ and nanobelts.² Herein we focused on the morphology controlled synthesis of IGO

nanostructures, including semi-nanotubes, nanowires, nanobelts and hierarchical nanostructures. The morphology can be efficiently tuned by proper selection and combination of the growth conditions, such as carrier gas, source materials, catalysts and growth temperature. Typical growth conditions for the IGO nanostructures with distinct morphologies are summarized in Table 6.1. In the following sections, we will present the detailed growth conditions, structural characterization results and growth mechanism discussions for each type of structure.

Table 6. 1 Summary of the growth conditions for the 4 types of typical IGO nanostructures.

	Growth T/°C	Catalyst	Source Material	Carrier Gas
Nanotube	300-400	In	Ge+In ₂ O ₃	Ar
Nanowire	520-600	Au	GeO ₂ +In ₂ O ₃	Ar
Nanobelt	620-700	None	GeO ₂ +In ₂ O ₃	Ar+O ₂
3D structure	500-600	Au	Ge+In	Ar

The novel wide bandgap ternary oxide nanomaterials can be used in high performance UV photodetectors. Photodetectors using IGO nanobelts showed that the devices have outstanding wavelength selectivity for solar-blind deep-UV detection, with the responsivity in solar-blind region 2-3 orders higher than that in UV region and 3-6 orders higher than that in visible region. The stable oxide nanodevices, together with superior performances such as high wavelength selectivity and fast photoresponse time, make them suitable candidates for future light sensing applications.

6.2 Self-Catalytic Growth of IGO Semi-Nanotubes

6.2.1 Experimental Methods

Ge powder, In_2O_3 powder and activated carbon powder with an atomic ratio of about 2:1:3 placed in a quartz crucible was used as solid source and mounted in the middle of the high-temperature zone. Cleaned Si (100) wafer was placed 15-20 cm from the powder source at a growth temperature of 300-400 °C. The temperature of the furnace was increased to 1000 °C at a rate of 10 °C min⁻¹ and kept at that temperature for 30 min under a constant argon flow of 90 sccm. Ambient pressure inside the tube was around 1 Torr during the entire process. Subsequently, the furnace was cooled down to room temperature.

6.2.2 Structural Characterizations

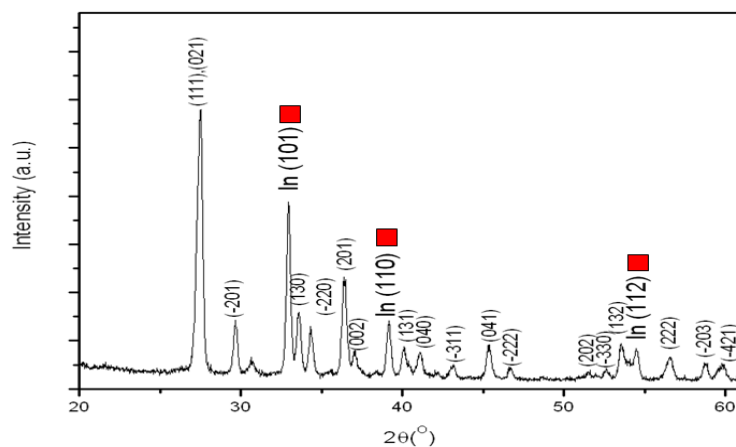


Figure 6. 1 XRD pattern of the indium germanate nanostructures. Both the IGO and In phases were detected. Red rectangles indicate the three peaks belong to In.

The products collected on the Si substrate were first characterized using XRD, as shown in Figure 6.1. The pattern suggests two crystalline phases, i.e., monoclinic IGO (JCPDS card 26-0768: $a=6.658$ Å, $b=8.784$ Å, $c=6.9266$ Å, $\beta=102.48^\circ$) and tetragonal In (JCPDS card 5-0642: $a=3.2517$ Å, $c=6.9459$ Å). The peaks belonging to In were indicated using red rectangles for clarity purpose.

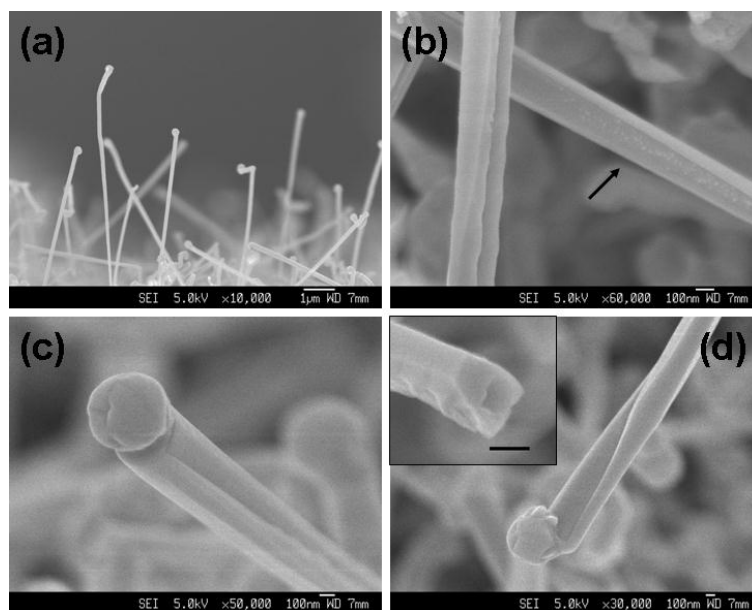


Figure 6. 2 SEM images of IGO semi-nanotubes. (a) low magnification of cross-section view; (b-d) high-magnification of the nanotubes revealing the semi-tubular structure and catalyst particles at the front. Inset in (d) shows an open end of a single nanotube. Scale bar is 100 nm.

A typical low magnification SEM image (cross-sectional view) of the products is shown in Figure 6.2a. The products are composed of a large quantity of 1D nanostructures with diameters and lengths in the range of 80-500 nm (corresponds to the catalyst particle sizes) and 5-20 μm , respectively. High magnification SEM images reveal that those structures are semi-nanotubes with hemispherical catalyst particles at the front. Representative magnified images of the body and tip of semi-nanotubes are shown in Figure 6.2b-d. Cross-sections of the semi-nanotubes are polygonous (Figure 6.2c) and a typical one with a roughly rectangular cross-section is shown in the inset of Figure 6.2d.

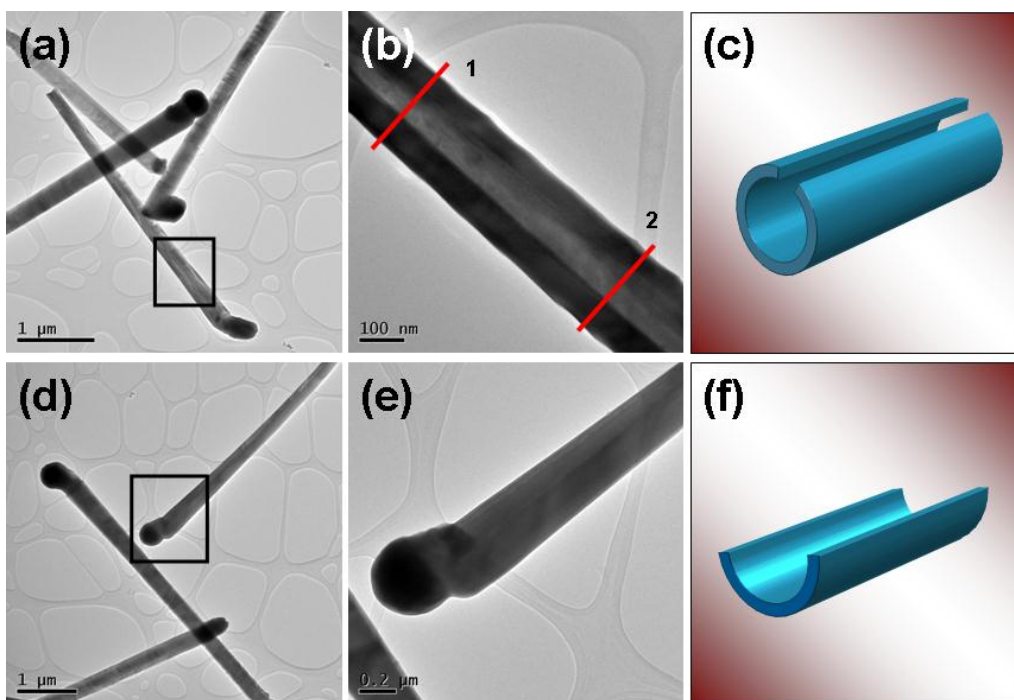


Figure 6. 3 (a,b) TEM images of semi-nanotubes with more than half tube-walls; (d,e) TEM images of semi-nanotubes with less than half tube-walls; (c,f) corresponding schematic illustrations of the semi-nanotubes.

More detailed structure and composition analyses of the products were carried out by TEM and EDS. Figure 6.3a and d are typical low magnification TEM images of the IGO nanotubes. Enlarged TEM image of the nanotube stem and catalyst tip (indicated by square in Figure 6.3a) is shown in Figure 6.3b and e, respectively. The hollow structure of the semi-nanotubes can be observed in Figure 6.3b. A hemispherical tip is shown at the nanotube front and instead of a complete cylinder tubular structure, the tube wall in Figure 6.3e consists of almost half of a circle, revealing the peculiar semi-nanotube structure. Schematic illustrations of the two kinds of nanotubes (with more than or less than half tube-walls) are shown in Figure 6.3c and f. The catalyst tips are omitted for clarity.

The nanotubes are frequently observed to be tapered as shown in Figure 6.2b (indicated by black arrow). In contrary to conventional tapering of NWs, *i.e.*, diameter of the NWs decreases from bottom to top due to non-catalytic decomposition of growth precursors or

catalyst migration, diameters of the nanotubes here increase as they grow. The diameters for position 1 and 2 in Figure 6.3b are 180 nm and 219 nm, respectively. One reason is that the tube walls are rolling up as the growth proceeds (Figure 6.2b and d), and subsequently the freshly grown parts of the nanotubes possess larger diameters than those segments away from the tips. In Figure 6.3b the opening widths (light region) of position 1 and 2 are 67 nm and 104 nm, respectively. But it is worth noticing that instead of the real width of inner cavity, the width of the light region is the opening between adjacent tube-walls, due to the incomplete tubular structure. Another possible reason is that the volumes of the liquid droplets grow larger as a result of continuous and simultaneous adsorption of In and Ge species from vapor phase.

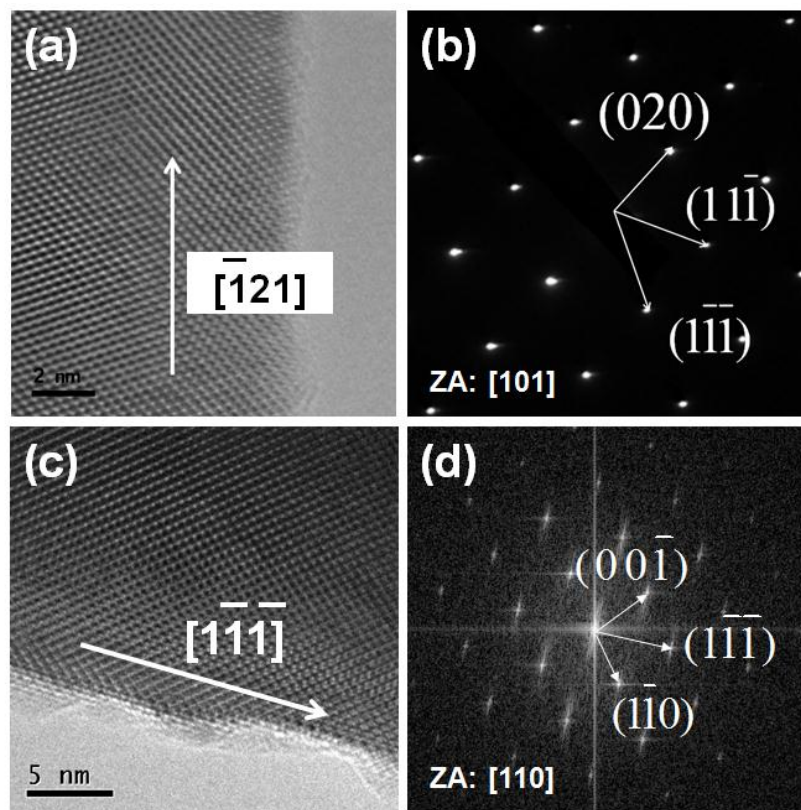


Figure 6. 4 (a,b) HRTEM and SAED of semi-nanotube grow along $\langle -121 \rangle$ direction; (c,d) HRTEM and FFT of semi-nanotube grow along $\langle 1-1-1 \rangle$ direction.

All the semi-nanotubes are single crystalline as confirmed using HRTEM and SAED. HRTEM images of the semi-nanotubes are shown in Figure 6.4. Figure 6.4a shows a

nanotube growing along $\langle -121 \rangle$ direction. The HRTEM image was taken along $[101]$ zone axis of a monoclinic IGO crystal. Corresponding SAED pattern is shown in Figure 6.4b. Figure 6.4c is the HRTEM image of a semi-nanotube growing along $\langle 1-1-1 \rangle$ direction; and the image was taken along the $[110]$ zone axis. Corresponding FFT pattern of the HRTEM is shown in Figure 6.4d.

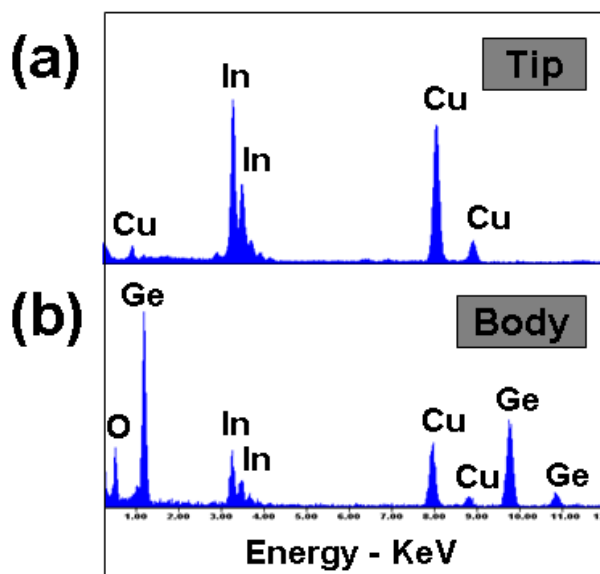


Figure 6. 5 EDS spectra of the (a) catalyst tip and (b) NW body of the semi-nanotubes.

EDS spectra taken from the tip and body of the semi-nanotubes are shown in Figure 6.5. They confirm that the tip is composed of indium while the body is composed of indium, germanium and oxygen with a roughly indium to germanium atomic ratio of 1:1. This is consistent with the XRD results, which show both IGO and In phases. Cu peaks come from the Cu grid used for TEM characterization.

6.2.3 Anisotropic Adsorption Induced Semi-Nanotube Formation

The growth of those single crystalline IGO semi-nanotubes can be explained by self-catalytic VLS mechanism.³ Indium serves as catalyst for IGO nanotube growth. In, In_2O and Ge vapor from the high temperature region would condense and form liquid droplets on the substrates

when they were brought to low temperature region by Ar flow. Continuous adsorption of those vapor species led to the precipitation of IGO at the solid-liquid interface when combined with residual oxygen in the furnace. Instead of the precipitation of pure Ge which leads to the growth of Ge NWs, formation of IGO compound results from the simultaneous adsorption of both In and Ge species from the vapor phase.

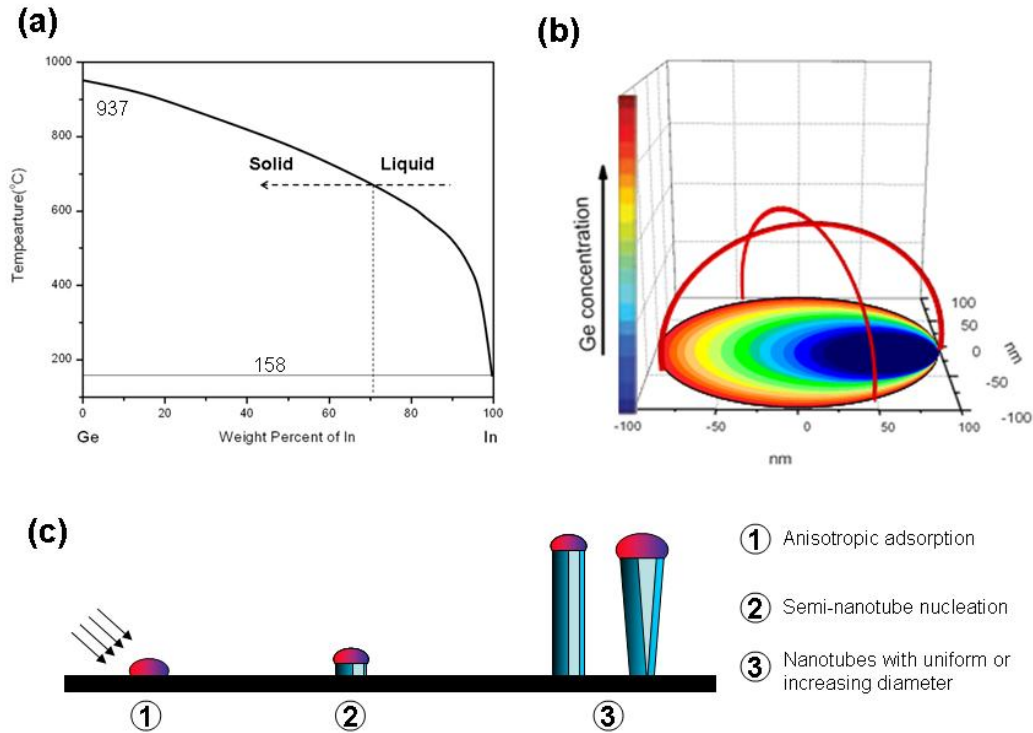


Figure 6. 6 (a) Binary phase diagram of Ge-In, showing that a higher In concentration is required if the liquid alloy were to solidify at a lower temperature; (b) germanium concentration gradient at the liquid-substrate interface (a circle with a diameter of 200 nm). The cap of the liquid droplet is omitted for clarity; (c) schematic illustration of the semi-nanotube nucleation and growth processes.

The semi-nanotubes were grown via a typical self-catalyzed VLS process, as shown in Figure 6.6. The Ge-In binary alloy phase diagram is shown in Figure 6.6a (small amount of oxygen is not expected to change the diagram significantly).⁴ A higher In concentration is required if the binary alloy wants to solidify at a lower temperature. And this indium ratio reaches almost 100% when the products are cooled down to a temperature below 158 °C. Although it is possible that the liquid droplet may contain oxygen during growth process due to the generation of In_2O from carbon-thermal reduction of In_2O_3 , it is not a stable compound and

would decompose during cooling process, forming IGO - a much more stable ternary oxide of indium and germanium at ambient pressure. This is verified by the fact that tetragonal In peaks were detected in XRD measurement and EDS spectrum reveals the catalyst tips contain only indium while germanium and oxygen contents are below detection level after growth.

One important issue to be addressed is that why semi-nanotubes are nucleated rather than complete nanotubes or NWs. We suggest that germanium concentration gradient near the liquid-substrate interface may play the key role during nucleation stage. Simulation results of three-dimensional growth model for Au-catalyzed GaAs NW with a diameter of 60 nm reveal that gallium concentration at the edges of the liquid-solid interface is higher than that at the center due to much shorter gallium diffusion distance.⁵ And the authors predicted the possibility for formation of tubular-shaped NWs based on this concentration gradient.⁵ Although the simulation result is based on solid-phase diffusion, this is also the case for catalyst particles in liquid state during growth. Average diameter of the IGO nanotubes here is around 300 nm. Those relatively large diameters would make it more difficult for germanium to distribute uniformly through the whole liquid-substrate interface and exacerbate the concentration variation, with the edges having higher concentration than central regions. Concentration variation along the edge may be attributed to the shadowing effect originating from anisotropic vapor adsorption as well as the exacerbated concentration variation. As a result, part of the edge possesses the highest germanium concentration as shown in Figure 6.6b. Places with high concentration would reach supersaturation first and turn to be nucleation sites for continuous nanotube growth. A schematic illustration of the semi-nanotube nucleation and growth process is shown in Figure 6.6c. It is suggested that germanium concentration gradient either through the liquid-substrate interface or along the edges may account for the nucleation of semi-tubular structure. The proposed mechanism

may potentially be tested by catalytic growth of NWs/nanotubes with highly directional vapor supply, such as growth via molecular beam epitaxy (MBE). Of course, the conditions have to be carefully optimized to achieve hollow nanotube growth instead of solid NWs. There may be other factors which are still unknown at the current stage leading to the growth of unique semi-tubular structures and requires further studies.

6.3 Au-Catalyzed Growth of IGO NWs

6.3.1 Experimental Methods

In a typical experiment for IGO NW synthesis, a small quartz tube containing mixed GeO_2 , In_2O_3 and carbon powder (molar ratio 2:1:4) was loaded into the furnace. Si(100) substrates coated with 12 nm Au film were placed at the low-temperature end to collect the products. The other experimental conditions were kept the same as those for semi-nanotube growth.

6.3.2 VLS Growth of IGO NWs

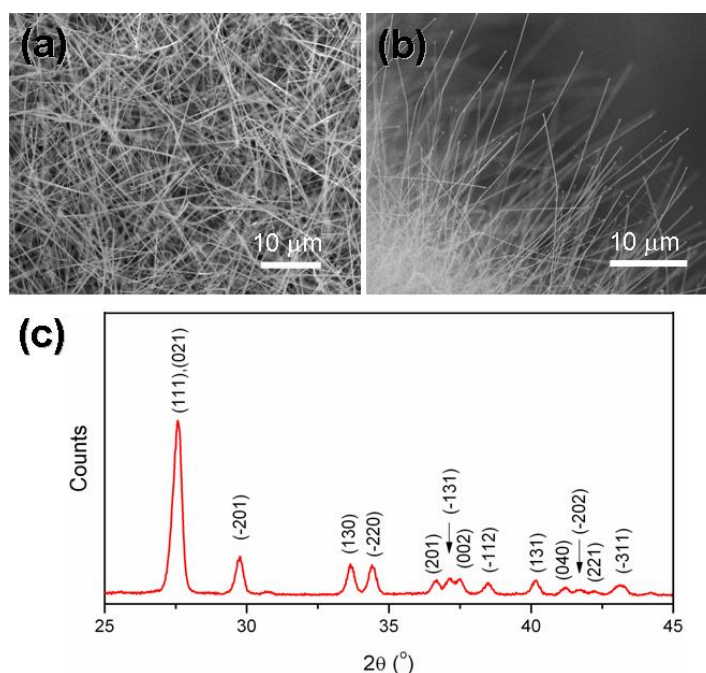


Figure 6. 7 (a,b) SEM images of the as-synthesized NWs on substrates; (c) XRD pattern of the indium germanate NWs.

After reaction, a layer of white product was found deposited on the substrate in the temperature range of 520-600 °C. The morphology of the as-synthesized products was first characterized using FESEM. Figure 6.7a is a typical top-view FESEM image of the NWs. Dense NWs of tens of micrometers long grew on the Si substrate surface and diameters of the NWs are in the range of 20-80 nm. Representative FESEM image of NWs growing at the edge of the substrates is shown in Figure 6.7b. XRD pattern of the NWs is shown in Figure 6.7c. All the peaks belong to monoclinic IGO crystal phase (JCPDS card 26-0768: $a = 6.658 \text{ \AA}$, $b = 8.784 \text{ \AA}$, $c = 6.9266 \text{ \AA}$, $\beta = 102.48^\circ$). It is worth mentioning that XRD results for the nanoribbons and hierarchical nanostructures which will be introduced later in this report all showed the same monoclinic IGO crystal phase.

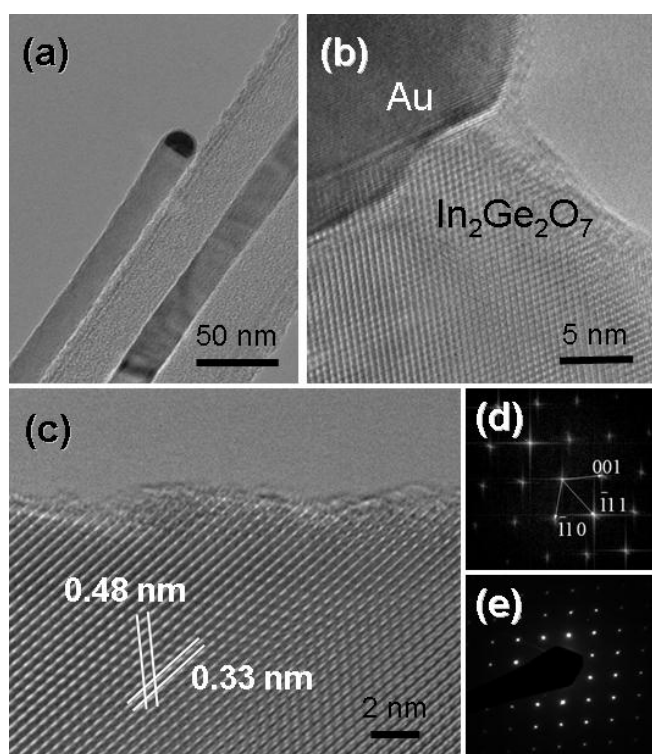


Figure 6. 8 (a) Low magnification TEM image of the IGO NW with metal catalyst particle at the front; (b) HRTEM image of NW segment below catalyst; (c) lattice-resolved HRTEM image of the NW; (d) two dimensional Fourier transform along [110] zone axis; (e) corresponding SAED pattern of the NW.

Detailed crystal structures of the NWs were further characterized by TEM. Figure 6.8a is a typical low magnification TEM image of the IGO NWs. Au catalyst particle can be clearly viewed at the growth front (dark region), indicating that the NWs are synthesized via VLS

mechanism.³ HRTEM image of the NW segment right below the catalyst particle is shown in Figure 6.8b. Lattice-resolved HRTEM image of the NW is shown in Figure 6.8c, with its corresponding two dimensional fast Fourier transform (FFT) and selected area electron diffraction (SAED) pattern shown in Figure 6.8d and e, respectively. HRTEM analyses confirm that all the NWs are single crystalline with no structure defects observed in the NW volume. The FFT as well as SAED pattern agrees well with the [110] zone axis of monoclinic IGO. Measured lattice spacing of 0.48 nm and 0.33 nm corresponds to the spacing between (001) and (-111) planes. Growth direction of the NW is close to [001] axis of the IGO crystal.

6.4 Spontaneous Growth of Ultralong IGO Nanoribbons

6.4.1 Experimental Methods

For IGO nanoribbon synthesis, keeping other experimental conditions the same as those for NW growth, Ar gas mixed with 5% O₂ at a total flow rate of 200 sccm was used; clean Si substrates without Au coating were used for product collection.

6.4.2 VS Growth of Nanoribbons with Rectangular Cross-Sections

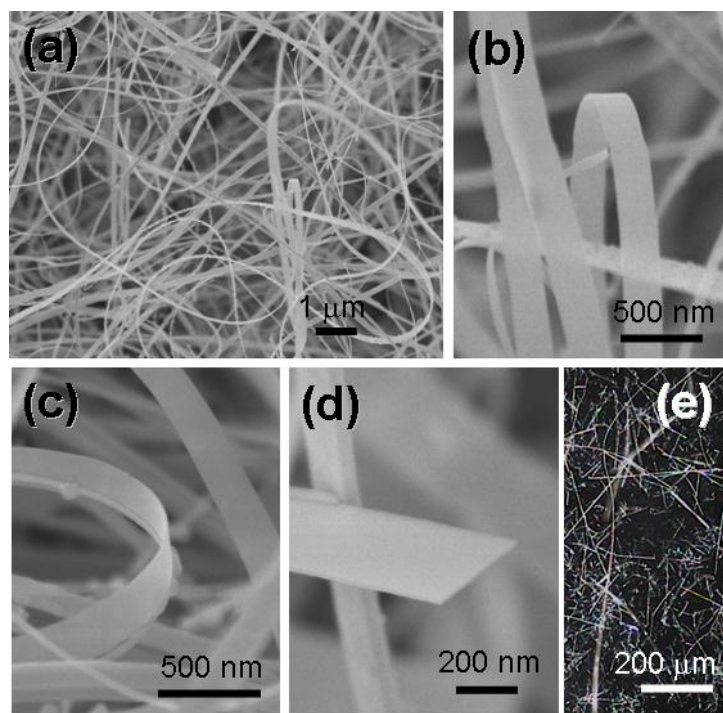


Figure 6. 9 (a) Low magnification SEM image of the IGO nanoribbons; (b,c) magnified SEM images showing the curved nanoribbon morphology; (d) SEM image of the nanoribbon cross-section; (e) low magnification optical microscopy image showing the ultra-long nanoribbons.

While pure Ar was used as carrier gas for IGO NW synthesis, nanoribbons were successfully synthesized through introduction of O₂ into the reaction chamber. In a typical nanoribbon synthesis reaction, Ar gas mixed with 5% O₂ at a total flow rate of 200 sccm was used as carrier gas. White fluffy layers of several millimeters extending from the substrate surface can be clearly observed when the furnace was cooled down. Figure 6.9a shows the representative morphology of IGO nanoribbons synthesized using mixed carrier gas (5% O₂). Magnified FESEM images revealing the unique curved nanoribbon shape are shown in Figure 6.9b and c. FESEM image of the nanoribbon cross-section is shown in Figure 6.9d. The width and thickness of the nanoribbon measured from the cross-section are 330 nm and 15 nm, with a corresponding width-to-thickness ratio of 22. The lengths of the as-synthesized nanoribbons are several hundreds of micrometers or even up to millimeters. Typical low magnification dark-field optical microscopy image showing the ultra-long nanoribbons is presented in Figure 6.9e.

Controlled experiments using mixed carrier gas of different O₂ concentrations showed that the nanoribbon growth temperature increased with O₂ content. For example, nanoribbon growth using carrier gas with 5% and 10% O₂ was observed in the temperature range of 620-700 °C and 750-800 °C, respectively.

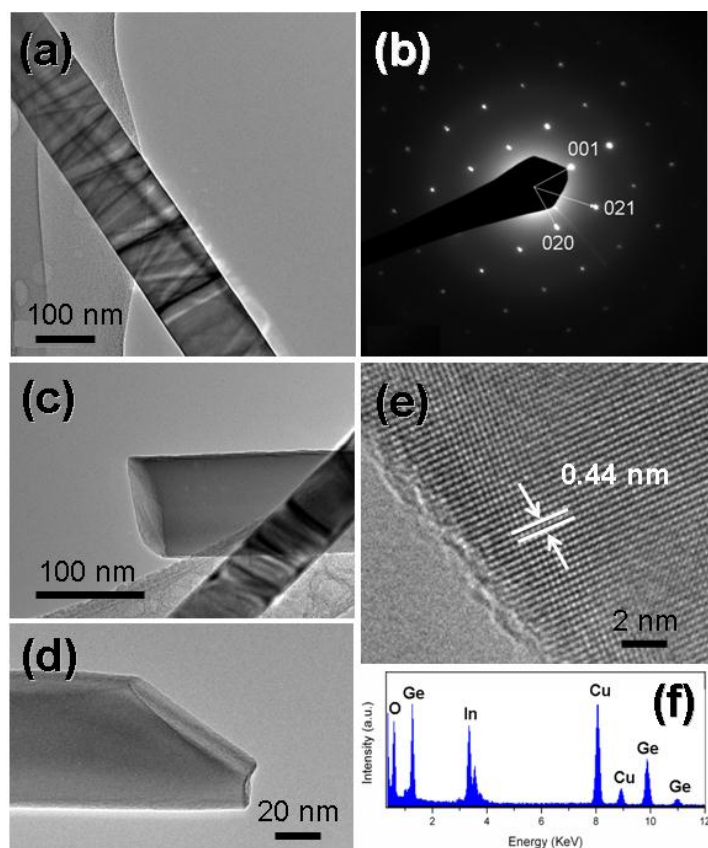


Figure 6.10 (a) TEM image of a single IGO nanoribbon; (b) SAED pattern of the nanoribbon along [100] zone axis; (c,d) TEM images showing the cross-sections of the nanoribbons; (e) HRTEM image and (f) EDS spectrum of the nanoribbons.

Morphology, crystal structure and composition of the nanoribbons were further characterized using TEM and EDS. Figure 6.10a is a representative low magnification TEM image of the IGO nanoribbon. The ripple-like contrast is due to the strain that resulted from the bending of the nanoribbon.⁶ SAED pattern of the nanoribbon taken along [100] zone axis is shown in Figure 6.10b. HRTEM image of the nanoribbon is shown in Figure 6.10e, and the measured lattice spacing of 0.44 nm corresponds to the spacing between (020) planes of monoclinic IGO. Upon taking the SAED pattern and HRTEM image into account, one can suggest that the preferred growth direction of the nanoribbon is close to [010] axis of the monoclinic

structure. TEM images of the rectangular cross sections of the nanoribbons are shown in Figure 6.10c and d. In comparison with the symmetric cross sections of NWs (such as circular, square or hexagonal), the rectangular cross sections with a large width-thickness ratio represent the distinct ribbon-like morphology. Careful examinations showed that no metal catalyst particles could be observed at the ends the nanoribbons, which is consistent with FESEM observation (see Figure 6.9d). Thus, VLS process may not be the dominant growth mechanism for nanoribbon formation. Finally, chemical composition of the nanoribbons was analyzed using EDS. EDS result (Figure 6.10f) reveals that the nanoribbons are composed of In, Ge and O, with an atomic ratio of In:Ge around 1:1. Peaks of Cu come from the Cu grid used for TEM characterization.

VS growth involving direct raw materials vaporization and condensation has been most widely employed to explain the formation of nanoribbons in vapor phase.⁷ However, unlike the well-developed VLS process, the detailed growth processes of the VS mechanism are still not fully understood.^{6,8,9} In general, surface energy and growth kinetics are the two key factors determining the final morphology of the products.⁶ There is a strong tendency to minimize the total surface energy during nanostructure nucleation and growth processes. Other factors that affect crystal growth kinetics may also play important roles in the formation of belt-like nanostructures, such as ambient gas, heating history, growth temperature or even the growth chamber geometry.^{7,10-12}

Here we propose a possible process that may account for the ultra-long and uniform IGO nanoribbon formation in our experiments. At the initial stage, nucleations of nanoclusters form on the substrate surface through direct vapor deposition at the low temperature region. The nanoclusters tend to be enclosed by low energy facets in order to minimize the total surface energy. Both theoretical and experimental studies have revealed a similar surface

energy minimization tendency for NW nucleation and growth.^{13,14} These low energy facets should be slow growing facets and require a high supersaturation for nucleation.¹⁰ On the other hand, the top surface of the clusters may not likely be low energy facets due to the crystal symmetry constraints.¹⁰ As a result, newly arriving growth species will not remain on the flat low energy side facets and tend to diffuse towards the atomically rough growth fronts with steps, ledges and kinks.⁶ The nanoribbon length increases rapidly due to the continuous preferential nucleation and incorporation of growth species at the top surface.

One critical issue to be addressed is what determines the cross section shape of the nanoribbons to be rectangular. Previous research work on whisker growth showed that the two-dimensional (2D) nucleation probability on whisker surface can be described as:^{9,15}

$$P_N = B \exp\left(-\frac{\pi\sigma^2}{k^2T^2 \ln \alpha}\right) \quad (1)$$

where P_N is the nucleation probability, B is a constant, σ is the surface energy, k is the Boltzmann constant, T is the absolute temperature and α is the supersaturation ratio defined by $\alpha=p/p_0$ (usually $\alpha > 1$), where p is the actual vapor pressure and p_0 is the equilibrium vapor pressure corresponding to temperature T . As revealed in the equation, lower surface energy corresponds to a higher 2D nucleation probability. In other words, the surface areas of the low energy surfaces tend to increase in order to minimize the total surface energy. Also, higher temperature and larger supersaturation ratio facilitate the 2D nucleation, resulting in the formation of sheet-like structure.⁹ In contrast, lower temperature and smaller supersaturation ratio promote the elongation along the axial direction and lead to the growth of wire-like structures.⁹ In our experiments, introduction of O_2 mainly has two effects. First, growth temperature increases with O_2 concentration. For example, the nanoribbon growth temperature using carrier gas with 5% and 10% O_2 are in the range of 620-700 °C and 750-800 °C, respectively. Second, the vapor supersaturation ratio increases with O_2 concentration

due to the faster oxidation rate. The higher growth temperature (T) and higher supersaturation ratio (α) along with the introduction of O_2 would increase the 2D nucleation probability of the low energy side facets, resulting in lateral growth (increase of surface area) of the side facets. Moreover, as viewed from the cross sections of the nanoribbons (Figure 6.9d and Figure 6.10c), formation of the slightly anisotropic rectangular shape is due to the different surface energies (σ) and thus different growth rates (according to equation 1) of the two groups of side facets. The effect of side facets growth rate has been reported previously for the WO_3 nanoribbon growth.¹⁶

We suggest that the 2D growth of the side facets is only significant at the nucleation and initial growth stage. The low energy side facets may not be atomically flat at the nucleation stage and have steps and ledges. The slightly different growth rates lead to the formation of rectangular cross sections. 2D growth of the side facets is negligible after a short growth period when the side facets are atomically flat. This is consistent with the experimental fact that the diameters of the IGO nanoribbons are very uniform with lengths up to millimeters and no tapering was observed. Previous research work on nanoribbon growth also showed negligible tapering of the nanoribbons although they are ultra-long in length.^{6,7}

6.5 Hierarchical IGO Nanostructures

6.5.1 Experimental Methods

For 3D hierarchical IGO nanostructure synthesis, mixed Ge, In and carbon powder (molar ratio 1:1:1) was used as source materials and other experimental conditions were kept the same as those for NW synthesis.

6.5.2 Combinational Homoepitaxial Growth

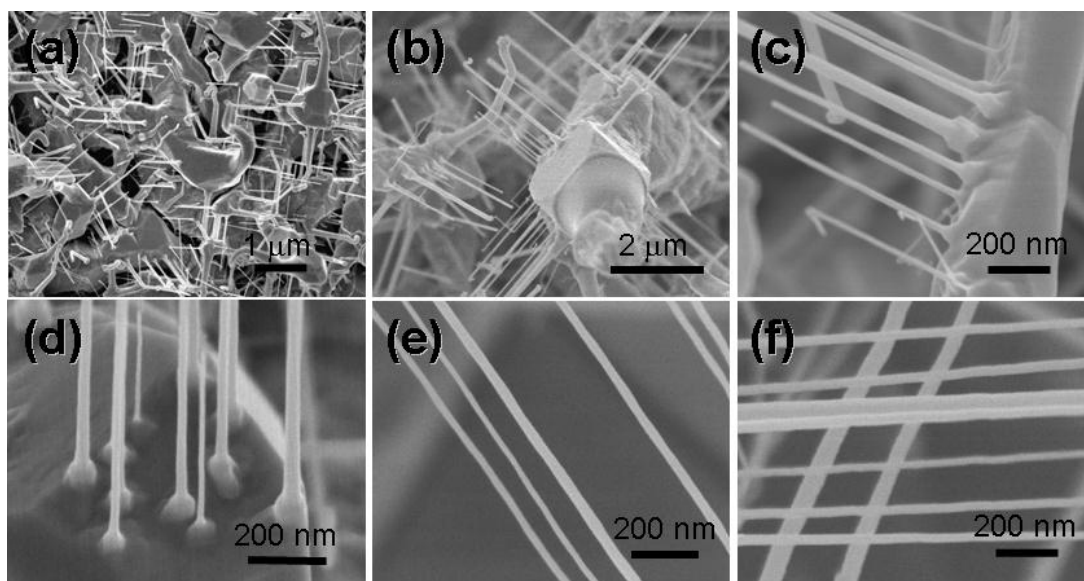


Figure 6. 11 (a) Low magnification SEM image of the hierarchical IGO nanostructures; (b-d) magnified SEM images showing IGO NWs growing on micro-crystals; SEM image of the (e) parallel and (f) crossed NW configurations.

3D hierarchical IGO nanostructures were synthesized using Ge and In as raw material through a similar thermal evaporation process. The deposited material in the as-synthesized sample has a dominant morphology consisting of aligned IGO NW arrays standing on top of large micro-crystals (Figure 6.11a). Enlarged FESEM images clearly reveal the NW arrays growing on polygonous micro-crystals (Figure 6.11b) or micro-rods (Figure 6.11c). Magnified view of the joint section of the aligned NW array is shown in Figure 6.11d. The thin NWs have dimensions of 10-50 nm in diameter and 0.5-2 μm in length. Typically the diameter of the joint section is slightly larger than that of the NW (Figure 6.11c and d). In the as synthesized sample, the microcrystals are in close vicinity to each other (Figure 6.11a and b) and it is possible for the orientation-aligned NW arrays to form crossed NW networks. Representative parallel and crossed NW networks are shown in Figure 6.11e and f, respectively.

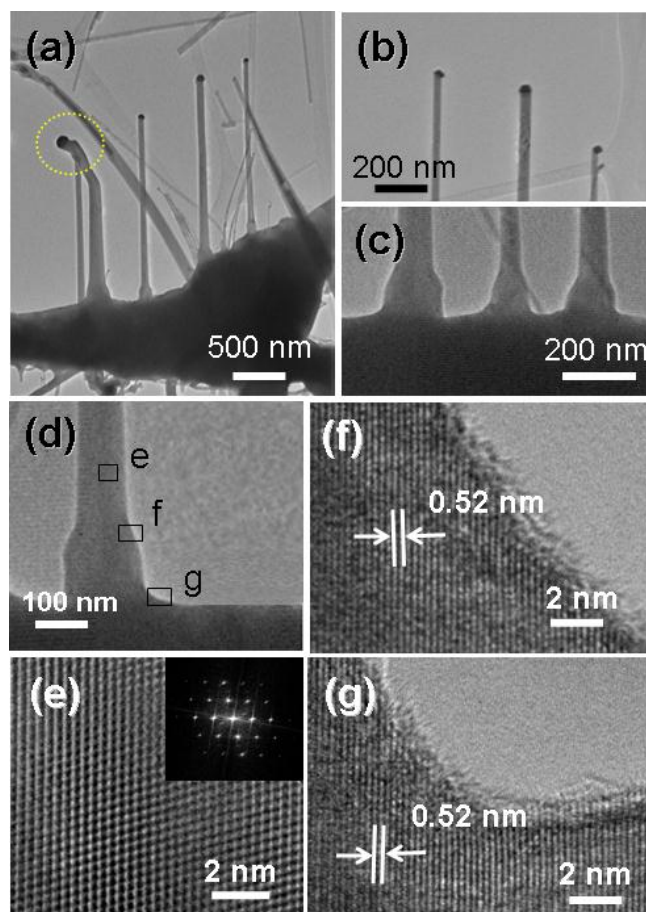


Figure 6.12 (a) TEM image of the hierarchical IGO nanostructures; (b,c) magnified TEM images of the tip and bottom of the NW array; (d) representative TEM image of the bottom of a single NW growing on micro-crystal; (e-g) HRTEM images of the NW with locations indicated in (d). Inset in (e) is the corresponding two dimensional Fourier transform recorded along $[110]$ zone axis.

Figure 6.12a is a typical low magnification TEM image showing the oriented growth of thin IGO NWs on top of the micro-crystals. Dashed circle indicates a curved NW tip while most of the NWs are straight. Enlarged views of the tip and bottom of the NW array are shown in Figure 6.12b and c. Metal catalyst particle can be clearly observed at the NW growth fronts (Figure 6.12b). Figure 6.12d is a representative TEM image of the bottom of a single NW growing on micro-crystal and corresponding HRTEM images with locations indicated by squares in Figure 6.12d are shown in Figure 6.12e-g. Measured lattice spacing of 0.52 nm in Figure 6.12f and g corresponds to the spacing between (1-10) planes of monoclinic IGO. Growth direction of the thin NWs is close to $[001]$ direction as determined from the FFT pattern (Figure 6.12e inset). HRTEM image of the NW-microcrystal junction (Figure 6.12g)

clearly shows the crystal continuity, suggesting that the micro-crystals serve as epitaxial templates for VLS NW growth. Similar oriented growth of NW arrays on large micro-crystals has previously been reported for several other materials.¹⁷⁻¹⁹

A combination of the VS and VLS mechanism can be used to explain the growth process of the IGO hierarchical nanostructures. First, the Ge and In vapor mixture, generated by evaporation of raw material at the center of the furnace (high temperature region), undergoes a fast condensation and reaction process at the low temperature region when combines with residual O₂ in the chamber. Large IGO microcrystals form on the substrate surface via VS mechanism. Second, parts of the Au nanoparticles remained on the IGO microcrystal surface when the crystals grow large. Consequently, the Au nanoparticles serve as catalysts for the growth of thin NWs. The formation of aligned NW arrays is due to the homoepitaxial growth considering the same composition of the microcrystal and NW. The crystallographic epitaxial relationship of the NWs and other initially formed structures has been demonstrated previously in the homoepitaxial growth of several other materials.^{17,18,20}

6.6 High Performance UV Photodetectors Using IGO Nanoribbons

6.6.1 Device Fabrication Methods

Single IGO nanobelt devices were fabricated by photolithography processes. Cr/Au (10/100 nm) electrodes were deposited on SiO₂/Si substrates (200 nm oxide) with dispersed IGO nanobelts by electron-beam evaporation. *I-V* characteristics of the devices were measured using an Advantest Picoammeter R8340A system. Spectral responses were measured using a Xenon lamp (500 W) as light sources. High frequency photo-switching behavior was measured using a 350 MHz Tektronix (TDS 5000B) oscilloscope with 230 nm incident light

chopped at 100 Hz. The device fabrication and performance measurements were collaborated with Dr. Li Liang in National Institute for Materials Science (NIMS), International Center for Materials Nanoarchitectonics (MANA), Japan.²¹

6.6.2 Performance Characterizations

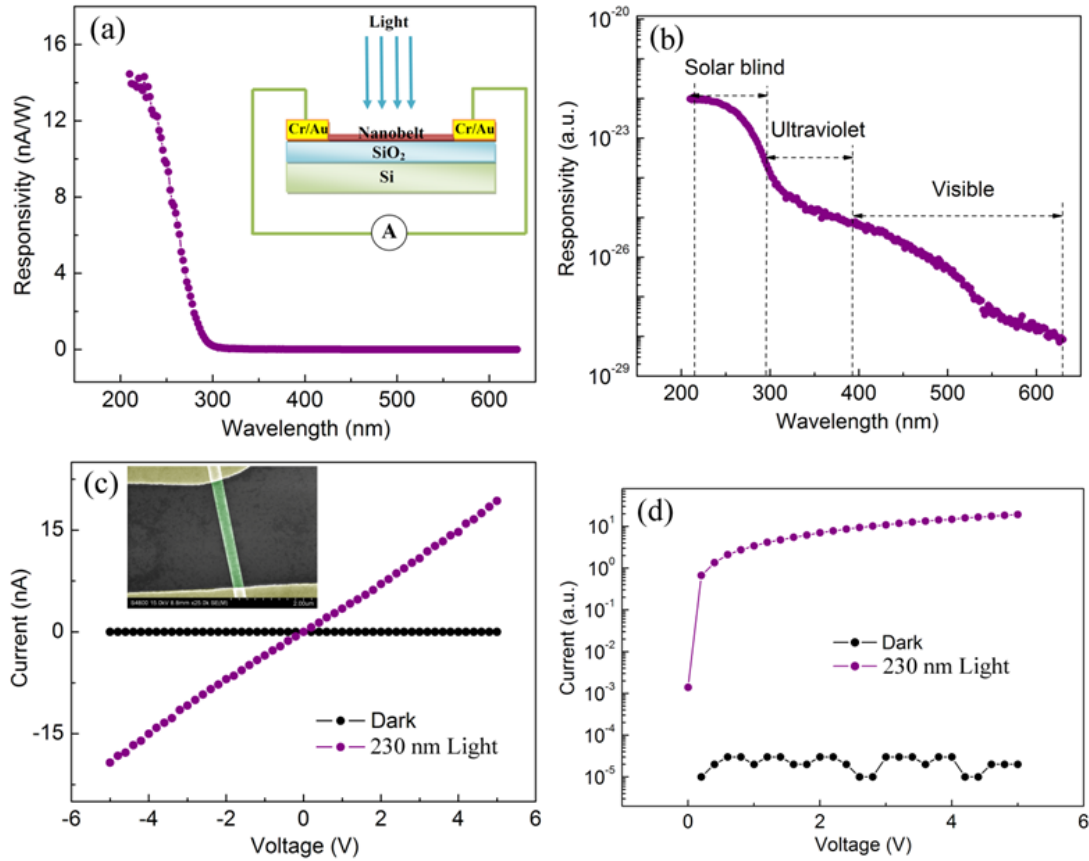


Figure 6. 13 (a) Linear and (b) logarithm plot of the spectral response in single IGO nanobelt device. (c) Linear and (d) logarithm I - V curves of the device in dark and under 230 nm light illumination. Insets in (a) and (c) are schematic and SEM image of the device. (This data was acquired by our collaborator Dr. Li Liang in NIMS-MANA, Japan)

IGO nanobelt photodetectors were fabricated for UV sensing applications. Schematic diagram of the device configurations and a typical SEM image of the device are shown in Figure 6.13a and c insets, respectively. Linear scale spectral response of the photodetector is shown in Figure 6.13a. As can be clearly viewed, the responsivity increases with shorter incident light wavelengths, with a highest value of 14 nA W^{-1} reached at 230 nm. The responsivity was calculated using $R_\lambda = I_p/PS$, where the photocurrent $I_p = I_{il} - I_d$ and I_d is the

dark current and I_{il} is the current of the device when illuminated with a light source, P is the light intensity irradiated on the nanobelt, and S is the effective illuminated area). A cutoff wavelength of ~ 290 nm was observed, which is consistent with the IGO bandgap of 4.43 eV (corresponds to ~ 280 nm). The responsivity for wavelengths >300 nm is negligible in the linear scale plot (Figure 6.13a).

To provide more detailed view of the photo-responsivity of IGO nanobelt photodetectors, logarithm scale spectral response is shown in Figure 6.13b. The wavelength range investigated was categorized into 3 sections: solar-blind region (~ 230 - 290 nm), UV region (~ 290 - 390 nm) and visible light region (~ 390 - 630 nm). We would like to highlight the fact that the responsivity in solar blind region is typically 2-3 and 3-6 orders of magnitude higher than that in UV and visible region, indicating outstanding wavelength selectivity of IGO nanobelt devices. This ultrahigh wavelength selectivity makes them superior candidates for selective deep-UV detection in the solar-blind region. Linear and logarithm scale I - V curves of the IGO nanobelts devices are shown in Figure 6.13c and d, respectively. The highly linear I - V curves in Figure 6.13c indicates good Ohmic conductance of the devices. The resistances of Schottky barriers at source/drain contacts are negligible compared with the resistance of the NW volume, which is expected to be highly resistant due to the large bandgap. The current increases significantly when illuminated with 230 nm light. For example, a photocurrent of 19 nA was recorded at a bias of 5.0 V under illumination but the dark current was negligible. Closer view in logarithm plot (Figure 6.13d) shows that the current increases by 6 orders of magnitude at 5 V bias, indicating a very high sensitivity.

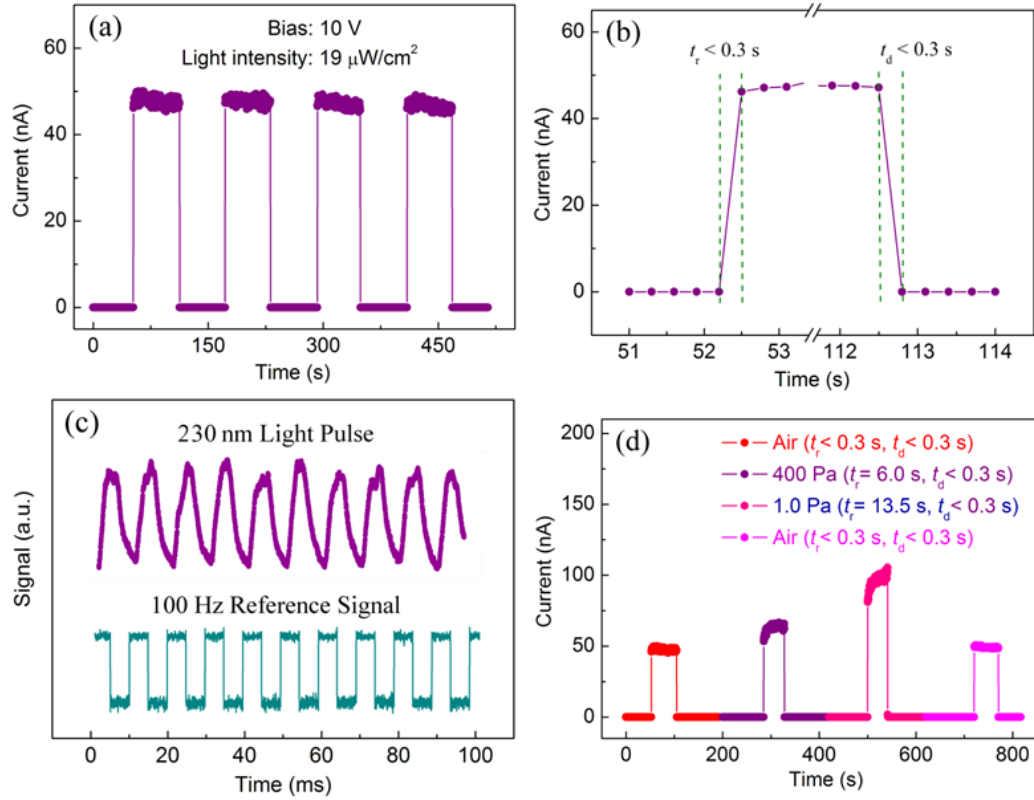


Figure 6. 14 (a) Photo-switching behavior of the IGO nanobelt devices under 230 nm light illumination ($19 \mu\text{W cm}^{-2}$) at a bias of 10 V. (b) Enlarged view of single cycle showing the fast response and reset time < 1 s. (c) High-frequency (100 Hz) switching characteristics. The reference signal is also shown for comparison. (d) Photoresponse in air and under different vacuum conditions. (This data was acquired by our collaborator Dr. Li Liang in NIMS-MANA, Japan)

Apart from the wavelength selectivity properties, photoresponse rate is another important characteristic of photodetectors. The photoswitching behavior of IGO nanobelt is shown in Figure 6.14a. The current changed rapidly between 0 and ~ 48 nA when the 230 nm light was turned on and off repeatedly. The device is rather stable without photocurrent degradation after several cycles. Enlarged view of an ON/OFF cycle is shown in Figure 6.14b, showing the fast response (t_r) and reset time (t_d) < 0.3 s (system limit). A more accurate measurement of the device photoresponse rate was measured using a 350 MHz Tektronix (TDS 5000B) oscilloscope, with incident 230 nm light chopped at a frequency of 100 Hz (Figure 6.14c). The current rose and decayed rapidly when the light was turned on and off (see comparison with reference signal). Fast response and reset time of ~ 2 ms were observed.

Photodetecting processes involve the electron/hole generation, carrier trapping and recombination. When the IGO nanobelts were exposed in air, oxygen molecules would be adsorbed on the nanobelt surface. The oxygen molecules would capture free electrons in the nanobelt volume, resulting in a surface depletion layer with poor conductivity. When the device was illuminated with UV light with photon energies above the bandgap, new electron/hole pairs would be generated leading to conductivity enhancement and hence current rise.²² Nanostructures with high surface-to-volume ratio than bulk or thin film materials are expected to show more significant depletion effects and consequently high sensitivities to the incident light. The proposed mechanism can be verified by the photocurrent measurements in vacuum conditions, where the surface depletion conditions changed with the oxygen concentrations. Figure 6.14d shows the photocurrent measurements in air and low vacuum conditions (400 and 1 Pa). The photocurrent level increases at higher vacuum conditions. In oxygen deficient conditions (such as 400 and 1 Pa), the oxygen re-adsorption rate is smaller and results in a higher nanobelt conductivity.

We would like to highlight that a higher vacuum conditions does not help to elongate the carrier lifetime (t_{life}), in contrary to our statement in previous publication.²¹ Instead we suggest that high oxygen concentration facilitates the hole trapping processes (electron/hole separation), which is beneficial for t_{life} . The increase of photocurrent at high vacuum conditions is due to the reduced depletion layer (increase the conductivity), which is more prominent than the decrease of t_{life} (reduce the conductivity). As shown in Figure 6.14d, the current would rapidly increase to the ON state value in air (<0.3 s) but the time is longer in vacuum conditions (6 s for 400 Pa, 13.5 s for 1 Pa). One possible reason is that the nanobelt in vacuum has a higher recombination rate (smaller t_{life}) and consequently, the carrier density (photocurrent) would increase to ON state more slowly.

6.7 Conclusions

In this chapter, we presented the syntheses of 4 types of novel IGO nanostructures: semi-nanotubes, NWs, nanoribbons and 3D hierarchical nanostructures. The unique semi-nanotubes were grown via a self-catalytic VLS method, with In as catalysts directing the growth of IGO tubes. The formation of unique semi-tubular structures was attributed to the anisotropic vapor adsorption process. The non-uniform supersaturation values at the liquid-solid interface led to the precipitation open tubular structures. IGO NWs were grown via an Au-catalyzed VLS method. IGO nanoribbons were grown by a direct deposition method without the usage of any metal catalysts. Ultralong nanoribbons with cross-sections were formed as a result of the anisotropic growth rates in the cross-sectional plane. 3D hierarchical nanostructures were formed as a combinational result of the VS and VLS growth. The microcrystals were formed by VS method while the thin IGO NWs were formed via VLS mechanism. Morphology control was achieved by proper tuning the related growth conditions, such as source materials, catalysts, gases and growth temperature. Our results are expected to provide useful guides for the synthesis of other complex oxide nanostructures.

The ultralong nanoribbons were used in UV photodetectors. Those novel wide bandgap nanostructures exhibited excellent wavelength selectivities and were especially suitable for deep-UV light sensing. The responsivity in the solar-blind deep-UV region (~ 200 nm) is almost 6 orders of magnitudes higher than that in visible region (~ 600 nm). Fast photoresponse time (down to ms order) was also achieved in our IGO nanobelt photodetectors. IGO nanostructures are shown to be ideal choices for solar-blind UV detection. The stable, low-cost and high performance devices may facilitate future industrial applications.

References:

- (1) Zhan, J. H.; Bando, Y.; Hu, J. Q.; Yin, L. W.; Yuan, X. L.; Sekigitchi, T.; Golberg, D. *Angewandte Chemie-International Edition* **2006**, *45*, 228-231.
- (2) Su, Y.; Li, S.; Xu, L.; Chen, Y. Q.; Zhou, Q. T.; Peng, B.; Yin, S.; Meng, X.; Liang, X. M.; Feng, Y. *Nanotechnology* **2006**, *17*, 6007-6010.
- (3) Wanger, R. S.; Ellis, W. C. *Applied Physics Letters* **1964**, *4*, 89-90.
- (4) Massalski, T. B. *Binary Alloy Phase Diagrams*; 1st ed.; ASM International Metals Park, Ohio, 1986.
- (5) Persson, A. I.; Larsson, M. W.; Stenstrom, S.; Ohlsson, B. J.; Samuelson, L.; Wallenberg, L. R. *Nature Materials* **2004**, *3*, 677-681.
- (6) Wang, Z. L. *Advanced Materials* **2003**, *15*, 432-436.
- (7) Pan, Z. W.; Dai, Z. R.; Wang, Z. L. *Science* **2001**, *291*, 1947-1949.
- (8) Moore, D.; Wang, Z. L. *Journal of Materials Chemistry* **2006**, *16*, 3898-3905.
- (9) Dai, Z. R.; Pan, Z. W.; Wang, Z. L. *Advanced Functional Materials* **2003**, *13*, 9-24.
- (10) Brent A. Wacaser, K. A. D., Jonas Johansson, Magnus T. Borgström, Knut Deppert, Lars Samuelson *Advanced Materials* **2009**, *21*, 153-165.
- (11) Gao, T.; Wang, T. H. *Journal of Physical Chemistry B* **2004**, *108*, 20045-20049.
- (12) Kirkham, M.; Wang, Z. L.; Snyder, R. L. *Nanotechnology* **2008**, *19*, 445708.
- (13) Wang, C. X.; Hirano, M.; Hosono, H. *Nano Letters* **2006**, *6*, 1552-1555.
- (14) Schmidt, V.; Senz, S.; Gosele, U. *Nano Letters* **2005**, *5*, 931-935.
- (15) Blakely, J. M.; Jackson, K. A. *J. Chem. Phys.* **1962**, *37*, 428-430.
- (16) Li, Y. B.; Bando, Y.; Golberg, D.; Kurashima, K. *Chemical Physics Letters* **2003**, *367*, 214-218.
- (17) Chen, X.; Kim, M. H.; Zhang, X.; Larson, C.; Yu, D.; Wodtke, A. M.; Moskovits, M. *Journal of Physical Chemistry C* **2008**, *112*, 13797-13800.
- (18) Gao, P. X.; Ding, Y.; Wang, Z. L. *Nano Letters* **2003**, *3*, 1315-1320.
- (19) Moore, D. F.; Ding, Y.; Wang, Z. L. *Journal of the American Chemical Society* **2004**, *126*, 14372-14373.
- (20) Seo, K.; Varadwaj, K. S. K.; Cha, D.; In, J.; Kim, J.; Park, J.; Kim, B. *Journal of Physical Chemistry C* **2007**, *111*, 9072-9076.
- (21) Li, L.; Lee, P. S.; Yan, C. Y.; Zhai, T. Y.; Fang, X. S.; Liao, M. Y.; Koide, Y.; Bando, Y.; Golberg, D. *Advanced Materials* **2010**, *22*, 5145-5149.
- (22) Yan, C. Y.; Singh, N.; Lee, P. S. *Applied Physics Letters* **2010**, *96*.
- (23) J. S. Jie, W. J. Z., Y. Jiang, X. M. Meng, Y. Q. Li, S. T. Lee *Nano Letters* **2006**, *6*, 1887.

CHAPTER 7 Conclusions and Recommendations

7.1 Conclusions

This dissertation focuses on the synthesis of Ge-based 1D nanostructures and their applications in photodetectors. We have presented the successful synthesis of semiconducting Ge, ZGO and IGO nanostructures. We first aimed to understand the underlying growth mechanisms for those novel 1D nanostructures, which can be used to guide the synthesis and morphology control processes. For example, Bi was successfully employed as an alternative catalyst for GeNW growth, as predicted by the Bi-Ge binary phase diagram. With crystallographic analyses of the ZGO and ZnO phases, we found that ZGO NWs can be used as lattice-matched substrates for the growth of aligned ZnO nanorod arrays, which were then achieved experimentally. The second main purpose of current project is to use those semiconducting nanostructures in photodetectors, with the goal of alleviating or eradicating problems exist in the current literature of photodetector research. We have found that GeNW networks showed greatly improved photoresponse time than single NW devices, due to the barrier dominated conductance in the network devices. Similar phenomenon was also observed in those ZGO NW network devices. Moreover, we have used Ge, ZGO and IGO NWs with different bandgaps to achieve excellent wavelength selectivity. For example, GeNW photodetectors can be efficient for visible light detection, while ZGO and IGO NWs with wide bandgaps can be used for selective detection of deep-UV lights.

In Chapter 4, we presented the synthesis of GeNWs using both the conventional Au and novel Bi catalysts by vapor phase deposition. Au is known to be excellent catalysts to direct GeNW growth. We found that high density GeNWs could be readily grown when using Au

thin film predeposited on Si substrate as catalysts. The as-grown GeNWs are single crystalline with uniform diameters. Searching for alternative metal catalysts for Si and Ge NW growth is of crucial importance to remove the detrimental effect of Au on the electronic properties of GeNWs. We have successfully demonstrated that Bi can be used for direct the growth of GeNWs in vapor phase, through a facile coevaporation method. The Bi catalyst particles were first deposited on the substrate due to its low melting point. Ge vapor generated at high temperature will be adsorbed and result in 1D NW formation. The novel in situ catalyst evaporation and deposition process also minimizes the oxidation of Bi, which may otherwise prevent the NW growth. The effect of Bi/Ge weight ratio in the source material was also investigated. A suitable Bi/Ge ratio is of great importance to achieve high quality NW growth, while high Bi concentration will result in the formation of large microparticles instead of NWs. Visible light photodetector based on single GeNW and NW networks were also demonstrated. Comparative studies revealed that the unique conduction mechanism in NW networks is especially desired to achieve fast photoresponse and reset time. While the reset time for single NW device is as large as 70 s, the reset time can be significantly shortened to less than 1 s by using percolated NW networks as detection channels. The NW-NW barrier behaviors like Schottky barriers, which responses very fast to the incident light. Thus the photoresponse time of the networks is very fast since the resistance of the network device is determined by the NW-NW junctions.

In Chapter 5, we presented the synthesis of ZGO NWs for photodetector applications. ZGO nanowires were synthesized using vapor phase transport method. High purity NWs were successfully obtained when the Zn/Ge ratio in the source materials were properly controlled. No impurity peaks, such as ZnO and GeO₂, can be detected from the samples grown under optimized conditions. We found that ZGO NWs can serve as excellent lattice-matched

substrates for ZnO NW array growth. The lattice mismatch between certain planes of ZGO and ZnO are pretty small (<4%) and hence could be used as an innovative low-cost substrate for epitaxial ZnO NW growth. Also, unlike the previous insulating substrates, such as Al_2O_3 , ZGO substrates are semiconducting and could facilitate device integration of the ZnO NWs. We demonstrated the introduction of kinks in the originally straight ZGO NWs. The NW growth direction could be varied from one to another when the pressure were changed in situ during growth, due to the change of supersaturation value in the catalyst and hence preferential nucleation at the catalyst-NW interface. This presents a novel nanoengineering technique to modulate the NW structures and hence properties and applications. Kinking does not introduce any structural defects in the NWs, *i.e.*, the entire NWs are still perfectly single-crystalline. Moreover, nanorings were also observed when the NW growth backward and merge with itself. The nanorings exhibited circular shapes due to the random kinking behavior of ZGO NWs. Finally, photodetectors based on ZGO NWs networks were also demonstrated. We only demonstrated the network photodetectors since they were shown to possess superior performance than those single-NW devices. Fast photoresponse and reset time below 1s were observed for those photodetectors, and were attributed to the unique barrier-dominated conductance of the network channels.

In Chapter 6, we presented the synthesis and applications of ternary IGO nanostructures. Excellent morphology control in the IGO nanostructures was achieved. Typically 4 types of nanostructures were grown: seminanotubes, nanowires, nanobelts and hierarchical structures. The morphology control was achieved by properly selecting and combination of the growth conditions, such as carrier gas, source material, catalyst and growth temperature. IGO seminanotubes were grown via a self-catalytic VLS method, where In serve as catalyst to direct the growth of IGO nanotube stem. The nanotubes exhibited unique semi-circular cross

sections, which were attributed to the non-uniform vapor adsorption and hence precipitation. IGO NWs were grown via Au-catalyzed VLS method, as evident from the Au catalyst at the front of the NWs after growth. IGO nanobelts were obtained when we changed the conditions to increase the supersaturation value in the growth chamber and promote the formation of anisotropic cross sections. The nanobelts were formed via VS method without the usage of any catalysts. Finally, hierarchical nanostructures, thin IGO nanowires standing on microcrystals, were formed via a combinational VS and VLS process. The microcrystals grew first via VS mechanism, then the small Au clusters on the surface of the microcrystals serve as catalysts to direct the thin NW growth. Epitaxial growth can be readily expected due the identical chemical composition of the microcrystal and NWs. Indeed, we have observed the growth of highly order NW arrays on the microcrystals. Semiconducting IGO nanobelts were used to fabricate deep UV photodetectors. The 1D nanostructures can function efficiently as solar blind deep UV photodetectors, where the conductance can vary by 6 orders with the incident light.

7.2 Recommendations for Future Work

Ongoing future work in this project may mainly focus on several directions, including:

1. Exploration of other complex germanate materials (*e.g.*, Bi-Ge-O, Ga-Ge-O, *etc.*);
2. Deepen understandings on the growth and structural evolution mechanisms to achieve better control over nanostructure design;
3. Improve the network distribution methods to achieve large scale uniform distribution with desired NW densities;
4. Design novel device configurations or use novel NW heterostructures to enhance the photodetector performances;
5. Fabricate integrated photodetector devices, probably with multi-functionality.

Besides the ZGO and IGO as have been demonstrated in this study, there are several other ternary germanates which are of potential interest for nanoelectronic and optoelectronic applications, such as bismuth germanate ($\text{Bi}_4\text{Ge}_3\text{O}_{12}$, BGO). BGO is the most commonly used oxide scintillator. Its unique properties such as good radiation hardness, high scintillation efficiency and good mechanical strength make it superior candidates for applications in particle physics, aerospace physics or geology exploration.¹⁻⁴ Fabrication of 1D BGO nanostructures and constructions of nanoscale devices would be especially useful for gamma ray detection. Large scale integrated device arrays would also be useful for the mapping of incident light locations. Fabrication of other germanate nanostructures would also be of interest for unique applications associated with their novel properties which have received little attention in literature.

Better understandings on the growth and structural evolution mechanisms are also required to achieve better control over the design of complex nanostructures. For example, we have successfully introduced kinks in the 1D NWs via pressure modulation, however, the detailed kinking mechanisms and material-dependent kinking behaviors are not fully understood yet. Controllability over of the segment lengths of nanorings remain to be improved. The preferential kinking behaviors of different materials can possibly be unveiled by designing comparative studies to investigate the effort of several possible factors, such as crystal phase (cubic or hexagonal), growth mechanism (VLS or VS), temperature, pressure modulation magnitude, vapor supply methods (CVD, PVD or MOCVD), *etc.* Clear understandings on the growth mechanisms will facilitate the design of nanorings with desired sizes and shapes. Understandings of the underlying mechanisms are also of crucial importance in design

complex heterostructures, such as core-shell NWs, branched NWs or even nanorings with segments composed of different materials.

For the fabrication of NW network devices, future work may focus on the fabrication of large scale uniformly distributed NW networks. While we have used a simple dropcast method to fabricate network devices, further efforts are required to produce networks with uniform distribution and controllable NW density. Potential methods may include contact printing, NW filtration, NW assembly by electrostatic forces on pattern areas or other novel and efficient methods.

Further improvements of the photodetector configurations are essential to improve device performances. There are still significant gaps between lab research and commercial applications despite the remarkable progresses in the past years. High performance devices with low fabrication costs are the targets for future research works. Novel NW heterostructures is one of the promising solutions for photodetector devices. Modulation of the NW structures, compositions may allow efficient controllability to tune the sensitivity and selectivity of NW photodetectors. Fabrication of radial and axial heterostructures or quantum dots decorated NWs may be considered as promising methods.

Fabrication of medium or large scale integrated devices is certainly one of the future research directions. High performance individual nanoscale devices can be integrated to enable greater functionalities. For example, devices suitable for selective detection of UV, visible or infrared light can be integrated in a single chip to achieve simultaneous reading and output of detection results of different lights. Moreover, light sensors and other devices like gas sensors can also be integrated to achieve multi-functionality.

References:

- (1) Cho, Z. H.; Farukhi, M. R. *Journal of Nuclear Medicine* **1977**, 18, 840-844.
- (2) Nitsche, R. *Journal of Applied Physics* **1965**, 36, 2358-&.
- (3) Lieder, R. M.; Jager, H.; Neskakis, A.; Venkova, T.; Michel, C. *Nuclear Instruments & Methods in Physics Research Section a-Accelerators Spectrometers Detectors and Associated Equipment* **1984**, 220, 363-370.
- (4) Nolan, P. J.; Gifford, D. W.; Twin, P. J. *Nuclear Instruments & Methods in Physics Research Section a-Accelerators Spectrometers Detectors and Associated Equipment* **1985**, 236, 95-99.

Publication List

1. **Yan, C. Y.**, Lee, P. S., Recent Progresses in Nanowire Photodetector Design and Performances (Invited Review), *Sci. Adv. Mater.* **2011**, Under Review.
2. **Yan, C. Y.**, Higgins, J. M., Faber, M. S., Lee, P. S., Jin, S., Spontaneous Growth and Phase Transformation of Highly Conductive Nickel Germanide Nanowires. *ACS Nano* **2011**, DOI: 10.1021/nn201108u.
3. **Yan, C. Y.**, Jiang, H., Zhao, T., Li, C. Z., Ma, J., Lee, P. S., Binder-Free Co(OH)₂ Nanoflake-ITO Nanowire Heterostructured Electrodes for Electrochemical Energy Storage with Improved High-Rate Capabilities, *J. Mater. Chem.* **2011**, DOI: 10.1039/c0jm04442c.
4. **Yan, C. Y.**, Singh, N., Lee, P. S., Kinking Induced Structural Evolution of Metal Oxide Nanowires into Single-Crystalline Nanorings. *ACS Nano* **2010**, 4, 5350.
5. **Yan, C. Y.**, Singh, N., Cai, H., Gan, C. L., Lee, P. S., Network Enhanced Photoresponse Time of Ge Nanowire Photodetectors. *ACS Appl. Mater. Interfaces* **2010**, 2, 1794.
6. **Yan, C. Y.**; Singh, N.; Lee, P. S., Wide-Bandgap Zn₂GeO₄ Nanowire Networks as Efficient Ultraviolet Photodetectors with Fast Response and Recovery time. *Appl. Phys. Lett.* **2010**, 96, 053108.
7. **Yan, C. Y.**; Lee, P. S., Crystallographic Alignment of ZnO Nanorod Arrays on Zn₂GeO₄ Nanocrystals: Promising Lattice-Matched Substrates. *J. Phys. Chem. C* **2010**, 114, 265.
8. **Yan, C. Y.**; Chan, M. Y.; Zhang, T.; Lee, P. S., Catalytic Growth of Germanium Oxide Nanowires, Nanotubes, and Germanium Nanowires: Temperature-Dependent Effect. *J. Phys. Chem. C* **2009**, 113, 1705.
9. **Yan, C. Y.**; Lee, P. S., Synthesis and Structure Characterization of Ternary Zn₂GeO₄ Nanowires by Chemical Vapor Transport. *J. Phys. Chem. C* **2009**, 113, 14135.
10. **Yan, C. Y.**; Lee, P. S., Bismuth-Catalyzed Growth of Germanium Nanowires in Vapor Phase. *J. Phys. Chem. C* **2009**, 113, 2208.
11. **Yan, C. Y.**; Singh, N.; Lee, P. S., Morphology Control of Indium Germanate Nanowires, Nanoribbons, and Hierarchical Nanostructures. *Cryst. Growth Des.* **2009**, 9, 3697.
12. **Yan, C. Y.**; Zhang, T.; Lee, P. S., Flow Assisted Synthesis of Highly Ordered Silica Nanowire Arrays. *Appl. Phys. A* **2009**, 94, 763.
13. **Yan, C. Y.**; Zhang, T.; Lee, P. S., Single Crystalline Semi-Nanotubes of Indium Germanate. *Cryst. Growth Des.* **2008**, 8, 3144.
14. Nandan, S., **Yan, C. Y.**, Lee, P. S., Comini, E., Sensing Properties of Different Class of Gases Based on the Nanowire-Electrode Junction. *Nanoscale* **2011**, 3, 1760.
15. Jiang, H., Yang, L. P., Li, C. Z., **Yan, C. Y.**, Lee, P. S., Ma, J., High-rate electrochemical capacitors from highly graphitic carbon-tipped manganese oxide/mesoporous carbon/manganese oxide hybrid nanowires. *Energy & Environmental Science*, **2011**, 4, 1813.
16. Nandan, S., **Yan, C. Y.**, Lee, P. S., Room Temperature CO Gas Sensing Using Zn-Doped Single In₂O₃ Nanowire Field Effect Transistor. *Sensors and Actuators* **2010**, 150, 19.
17. Li, L., Lee, P. S., **Yan, C. Y.**, Zhai, T. Y., Fang, X. S., Liao, M. Y., Koide, Y., Bando, Y., Golberg, D., Ultrahigh Performance Solar Blind Photodetectors Based on Individual Single Crystalline In₂Ge₂O₇ Nanobelt. *Adv. Mater.* **2010**, 22, 5145.